ENGINYERIA ELECTRÒNICA ELÈCTRICA I AUTOMÀTICA

UNIVERSITAT ROVIRA I VIRGILI

Graduate Students Meeting on Electronics Engineering

Tarragona, Spain. June 19 - 20, 2014

BOOK OF ABSTRACTS

DIPUTACIÓ DE TARRAGONA

IEEE

FUNDACIÓ URV

ENGINYERIA ELECTRÒNICA ELÈCTRICA I AUTOMÀTICA

UNIVERSITAT ROVIRA I VIRGILI

Graduate Students Meeting on Electronics Engineering

Tarragona, Spain. June 19 - 20, 2014

Programme

Programme

Thursday, June 19th

9:30 Opening Session

09:45 Invited conference: Efficient gas sensing by resistance gas sensors at various temperatures and under ultraviolet irradiation.
Dr. Janusz Smulko. ***Gdansk University of Technology, Poland***

10:45 Coffee break

11:15 Invited conference: An introduction to spatial statistics for micro/nanoelectronics and materials science using the R language
Prof. Enrique Miranda, ***(IEEE Distinguished Lecturer)***
Escola d'Enginyeria, Universitat Autònoma de Barcelona, Spain

12:15 Students Oral Session 1

- **3-D Finite-Element Optical Modeling of Interdigitated Heterojunction Organic Solar Cells, Pedro Granero et al.**
- **Engineering nanoporous anodic alumina label-free optical biosensors, Gerard Macias et al.**
- **Comparison of Several Dithering Signals in Extremum Seeking Control for MPPT Operation of PV Panels, Héctor Zazo et al.**

13:15 Lunch

14:30 Poster Session

16:00 Invited conference: Charge Carrier Generation in Bulk Heterojunction Organic Solar Cells: from a 2D Model to extraction of parameters.
Dr. Yann Leroy, ***Université de Strasbourg***

17:00 Coffee break

17:30 Students Oral Session 2:

- **Hybrid electronic system based on multisensor data fusion for milk ageing analysis, Zouhair Haddi et al.**
- **Use of a CNT-coated piezoelectric cantilever with double transduction as gas sensor for benzene detection at room temperature, Pierric Clément et al.**
- **Automatic Compound Deconvolution and Alignment in Comprehensive Double Gas Chromatography - Mass Spectrometry by Blind Source Separation, Xavi Domingo et al.**

Friday, June 20th

09:30 Invited conference: An Introduction to Wireless Power Transfer: Basics, Applications and Design. Dr. Faical Turki, ***Vahle GmbH & Co. KG, Kamen - Germany***

10:30 Coffee break

11:30 Invited conference: GCxGC data analysis: challenges and possibilities using tensorial calibration
Dr. Gabriel Vivo-Truyols, ***University of Amsterdam***

12:30 Students Oral Session 3

- **Analysis and Design of AC-DC PFC with Low THD, Mirko Bodetto et al.**
- **Abstract Energy Management of a Fuel Cell Serial-Parallel Hybrid System, Harrynson Ramírez et al.**
- **Time-coded chipless RFID temperature sensor with self-calibration based on a Vivaldi antenna, Ángel Ramos et al.**

13:15 Closing Session

ENGINYERIA ELECTRÒNICA ELÈCTRICA I AUTOMÀTICA

UNIVERSITAT ROVIRA I VIRGILI

Graduate Students Meeting on Electronics Engineering

Tarragona, Spain. June 19 - 20, 2014

Invited Sessions

ENGINYERIA ELECTRÒNICA ELÈCTRICA I AUTOMÀTICA
UNIVERSITAT ROVIRA I VIRGILI
Graduate Students Meeting on Electronics Engineering
Tarragona, June 19th and 20th of 2014

Efficient gas sensing by resistance gas sensors at various temperatures and under ultraviolet irradiation

Dr. Janusz Smulko

Gdansk University of Technology, Poland

Abstract:

Taguchi gas sensors are very popular and can be used to detect various gases and their mixtures. Their main disadvantage is very limited selectivity. Practical use of gas sensors in environmental applications (e.g., in sewage systems to protect workers, in air conditioning systems to monitor atmosphere quality) requires determination of concentration of a few mixed gases at the same time. Independent sensors are usually used to determine concentration of the selected gases that means high maintenance costs and energy consumption. I would like to present recent results of improving gas detection by utilizing a single gas sensor and additional measurements to get more information about ambient atmosphere. Fluctuation enhanced sensing can be successively applied to improve gas selectivity. That method was proposed a few years ago and resulted in improvement of gas detection selectivity and sensitivity for various gas mixtures and using different gas sensors. The simple measurement setup can measure voltage fluctuations across the sensor to determine its power spectral density and to estimate sensor DC resistance. Both factors depend on gas sensor ambient atmosphere. Thus, observing voltage power spectral density and DC resistance we can detect some gases and determine their concentration.

Another possible technique of improving gas selectivity is modulating gas sensor temperature. That technique can be used by applying abrupt change of the sensor heating voltage. Such abrupt voltage drop results in dynamic DC resistance change which exhibits characteristic shape and requires about two minutes to stabilize its new value for commercial Taguchi gas sensors. When the sensor is placed in atmosphere of the mixed gases we can observe that the DC resistance changes at different pace. That fact can be utilized to improve gas detection selectivity.

The next considered method of changing sensors properties utilizes ultraviolet irradiations of the gas sensing layers (e.g., WO3 or TiO2) where a photocatalytic effect can be observed. Such method means usually lower energy consumption and faster response when compared with the presented method of temperature modulation. The preliminary results confirmed usefulness of that method. New results will be presented for WO3 gas sensing layers as well.

Additional information about gas sensor ambient atmosphere gathered by applying different modulation methods can be effectively used when productive detection algorithm is applied. Various algorithms for gas mixtures detection will be presented. Problems of applying Principal Component Analysis and Support Vector Machine method will be characterized by considering their computation complexity and necessity of additional parameters assessment.

Biography:

Janusz M. Smulko was born in Kolno, Poland. He received his M.Sc., Ph.D. and D.Sc. degrees in electronics from Gdansk University of Technology, Poland, in 1989, 1996 and 2007, respectively. Presently, he is Head of the Metrology and Optoelectronics Department of the Gdansk University of Technology. He had also conducted scientific research in short-term positions in Texas A&M University (2003), Uppsala University (2006/07), Massachusetts Institute of Technology (2011, 2013). As a researcher he focuses on the application of 1/f noise for gas sensing and reliability assessment of electronic components and structures, influence of noise on detection efficiency in Raman spectroscopy systems. He is a member of the Committee on Metrology and Scientific Instrumentation of the Polish Academy of Science and Editor-in-Chief of Metrology and Measurement Systems Journal.

ENGINYERIA ELECTRÒNICA ELÈCTRICA I AUTOMÀTICA
UNIVERSITAT ROVIRA I VIRGILI
Graduate Students Meeting on Electronics Engineering
Tarragona, June 19th and 20th of 2014

An introduction to spatial statistics for micro/nanoelectronics and materials science using the R language

Prof. Enrique Miranda

Escola d'Enginyeria, Universitat Autònoma de Barcelona, Spain

Abstract

Spatial statistics (SS) is a specific branch of statistics aimed at describing and characterizing the location of randomly distributed objects in the space (3D) or in the plane (2D). The objects can be trees in a forest, cells in biological tissues, galaxies in the universe, corrosion pits in metals, point-like defects in a silicon crystal wafer, etc., which from the mathematical viewpoint are regarded as a spatial point pattern. A central question in SS is to assess whether these objects interact or they follow a Complete Spatial Randomness (CSR) process. As in other branches of statistics, SS basically deals with exploratory data analysis, parameter estimation, model fitting and hypothesis test formulation. In this presentation, I will focus the attention exclusively on exploratory data issues, and to this end I will make use of a number of numerical and functional estimators able to summarize 2D data sets. Three examples will be discussed: breakdown spots in capacitors with high-K dielectrics, defective pixels in a CMOS radiation sensor and some stochastic patterns in different material systems. A brief introduction to the Spatstat package for R language will be provided.

Biography

Enrique Miranda was born in Buenos Aires, Argentina in 1963. He has a PhD in Electronics Engineering from the Universitat Autònoma de Barcelona (UAB), Spain (1999) and a PhD in Physics from the Universidad de Buenos Aires (UBA), Argentina (2001). From 1987 to 2003, he was Assistant Professor at the Faculty of Engineering - UBA and from 2001 to 2003, Associated Researcher of the National Council of Science and Technology-CONICET, Argentina. Currently, he is Professor at the Escola d'Enginyeria-UAB. Dr. Miranda has received research fellowships from the Spanish International Cooperation Agency: INTERCAMPUS (Universidad de Zaragoza), MUTIS (UAB), RAMON y CAJAL (UAB), German Exchange Academic Agency-DAAD (Technical University Hamburg-Harburg), italian government (Universita degli Studi di Padova), Matsumae International Foundation: MATSUMAE (Tokyo Institute of Technology, Japan), TAN CHIN TUAN (Nanyang Technological University, Singapore), Science Foundation Ireland: WALTON visitor awards (Tyndall National Institute), Slovak Academy of Sciences, and the distinguished visiting fellowship from the Royal Academy of Engineering (University College London, UK). He has authored and co-authored around 150 papers most of them devoted to the electron transport problem through the gate insulator in MIS and MIM devices: tunneling, degradation, and post-breakdown conduction. Dr. Miranda serves as member of the Distinguished Lecturer program of the Electron Devices Society (EDS-IEEE) and as Editorial Advisor of the journal Microelectronics Reliability. He forms or has formed part of INFOS, IRPS, ESREF, MIEL, EMRS and ESSDERC Technical or Steering Committees.

Charge Carrier Generation in Bulk Heterojunction Organic Solar Cells: from a 2D Model to extraction of parameters.

Dr. Yann Leroy
Télécom Physique Strasbourg

Abstract:
Modeling of Organic Solar Cell is only poorly treated as compared to the amount of experimental studies dedicated to this topic. The 1D models assuming an effective-medium in place of the active layer of the cells are the only models largely widespread. However, they can not reproduce correctly the morphology effects of a blend of donor and acceptor materials used for the active layer.

We will present a 2D model taking explicitly into account the donor and acceptor domains as well as a complex mechanism for free charge carrier generation. This mechanism involves Charge Transfer (CT) states which are bound electron-hole pairs pinned at the interface between the two domains. Consequently, a specific treatment has been developed in order to treat these CT states as a 1D species. The model implemented within the finite element software Comsol Multiphysics is validated through comparison with P3HT:PCBM standard cell measurements.

The model implies a large number of parameters which can be more or less known depending on the choice of the donor and acceptor materials. To identify these unknown parameters, fitting procedures are required. Unfortunately, classical fitting procedures, like Levenberg-Marquardt algorithm, are no longer reliable for the number of parameters considered here (up to 20 when some geometrical parameters are concerned). Specific statistical approaches can handle this kind of problem. We will present how a Markov Chain Monte Carlo fitting procedure helps to give reliable information about the possible sets of parameters compatible with experimental measurements.

Biography:
Yann Leroy graduated in 1998 from a french Engineer School, Télécom Physique Strasbourg, where he specialized in Physics and Modeling. In parallel, the same year, he obtained a M.Sc. in Condensed Matter and Nanophysics from the University of Strasbourg (France). He received his Ph.D. degree in Physics from the same University in 2001 and joined Télécom Physique Strasbourg as an Assistant Professor in 2002.
Doctor Leroy's expertise is the theory and simulation of disordered systems applied to the physics of devices, and more specifically on charge transport phenomena in nanostructures such as metallic nanoparticles and quantum dots. In the last decade, the research topics have dealt with the single-electron transistors and nanocrystal floating gate flash memories.
Approaches to these problems involve Monte-Carlo simulations and advanced self-consistent Schroedinger-Poisson models using a finite element methode.
More recently, he has focused on the electrical modeling of organic solar cells based on bulk heterojunctions as active layers.

An Introduction to Wireless Power Transfer: Basics, Applications and Design

Dr. Faical Turki

Vahle GmbH & Co. KG
Kamen – Germany

Abstract:
Wireless power transfer technologies were introduced in the industrial applications in the late nineties. The most spread layout is a distributed supply line along the driving track of a vehicle as a mobile load. These solutions feature significant advantages compared with conventional sliding contact technologies regarding wear and tear, maintenance and environmental influences.

Nowadays this technology is implemented in a new application field related to the emerging electrification trend of transportation vehicles especially in automotive products. The wireless power transfer is used for a convenient and automatic vehicle battery charging.

The basics of this technology and typical designs for known applications are presented and future visions of the deployment are introduced. Special emphasis will be put on the influence of the produced magnetic field on objects in its proximity and the solutions undertaken to solve this safety issue.

Biography:

Dr. Faical Turki is a power electronics specialist with an experience of more than fourteen years in in the research and development of industrial electronics. His four years in bleeding-edge research on IGBT based power electronics for wind turbines gave him an inside look at the design challenges of high efficiency power converters. This experience allowed him to take part of the earliest development of the first wireless inductive power supply systems. Starting with his work in the Institute for Electrical Machines, Traction and Drives in Braunschweig, he looks back on over ten years of research in the field of wireless power supply.
Since 2007 he is working at Paul Vahle GmbH & Co.KG in the development department for Contactless Power Systems CPS® and now he is head of the research and development of contactless power and data transfer systems for electric vehicles, trams and industrial applications.

His research includes polyphased inductive high power supply, bidirectional approaches, magnetic design, high frequency resonant converter topologies and data transfer on magnetically coupled power transfer circuits.

Dr. Turki received the Dipl.-Ing. degree in electrical engineering and the Ph.D. degree in electrical engineering at the Technical University of Braunschweig , Germany in 2002 and 2007, respectively. He is member in VDE an IEEE.

ENGINYERIA ELECTRÒNICA ELÈCTRICA I AUTOMÀTICA
UNIVERSITAT ROVIRA I VIRGILI
Graduate Students Meeting on Electronics Engineering
Tarragona, June 19th and 20th of 2014

GCxGC data analysis: challenges and possibilities using tensorial calibration

Gabriel Vivó-Truyols

University of Amsterdam,
Science Park, 904. 1098 XH Amsterdam (The Netherlands)
e-mail: g.vivotruyols@uva.nl

Abstract:
In analytical chemistry, we are witnessing a major increase in the amount of data generated by instrumentation. This is mainly due to the advent of comprehensive separation techniques (like two-dimensional gas chromatography, GCxGC) or mass spectrometry. Analytical chemistry is becoming one of the disciplines able to generate "Big Data", as economics or satellite imaging. Nowadays, a single experiment with a GCxGC-HRMS (two-dimensional chromatography coupled with high-resolution mass spectrometry) generates 15 Gb of data per hour.
Tensorial calibration constitutes, in principle, a promising framework to deal with the challenges posed to analyse this Big Data. Tensorial calibration is based in building up calibration models attending to the order of the tensor that a single experiment produces in each instrument. In this way, GCxGC-MS (like the one mentioned above) constitutes a third order instrument, as the data from a single experiment is logically arranged as a third-order tensor (a "cube of data"). Hence, third-order calibration techniques can be in theory used to deal with the data treatment of these instruments.
Surprisingly, the premises to apply third-order tensorial calibration are rarely met in practice. For example, the condition of trilinearity is normally not satisfied, due to retention time misalignments in the second-dimension separation mechanism. Additionally, when data from different experiment are treated together, misalignments between injections jeopardize the application of third-order tensorial calibration models. Another problem arises when the structure of the data is considered, as high-resolution mass spectrometry (used commonly nowadays) makes it very difficult to construct a third-order tensor, unless it is very sparse.
In this lecture, the challenges and opportunities of the application of tensorial calibration to GCxGC are going to be discussed. Also, some alternatives to the classical tensorial calibration methods are going to be proposed, like the use of Bayesian statistics to deal with the problem of automation in data treatment.

Biography:
Gabriel Vivó-Truyols (1975) studied analytical chemistry at the University of Balearic Islands (Spain) and obtained his MSc with honours in 1998. In 2004 he earned his PhD with honours from University of Valencia (Spain) on chemometrics methods for optimisation and data treatment of HPLC. His PhD was awarded with the "D.L. Massart award in chemometrics", a price given every two years to the best PhD thesis in chemometrics, world-wide. Parts of the PhD were conducted at the University of Brussels, under the supervision of prof. Massart. In 2004 he joined the team of Peter Schoenmakers (University of Amsterdam), where he developed a research program focused on chemometric techniques for optimisation, calibration and data-treatment of two-dimensional chromatographic methods. In 2007 he joined the joined BP in Sunbury (London area) as a chemometric specialist. During this work, he developed chemometric methods in different areas in the refining and marketing sector, including GCxGC analysis of petroleum subproducts, as well as methods for on-line infra-red analysis. Since 2008, Gabriel Vivó-Truyols is scientific consultant for BP in analytical chemistry and chemometrics, including GCxGC data analysis, on-line spectroscopic measurements, HPLC-DAD analysis, risk analysis and other projects. In 2009 he joined the analytical-chemistry group of Peter Schoenmakers at University of Amsterdam as assistant professor. Gabriel Vivó-Truyols has conducted 6 MSc thesis (one of them was recipient of the University of Amsterdam MSc award), and is currently conducting 4 PhD programs (one already concluded). The main part of his work has been performed in collaboration with industries, including Shell, BP, BASF, Merck, Unilever, DSM or the Dutch Forensic Institute (among others). He is (co)author of more than 40 articles, focused in the area of chemometrics and chromatography. Along with his task as assistant professor, he is the founder of the spin-off company "Tecnometrix" (www.tecnometrix.com) aimed to deliver consultancy and software in the area of chemometrics in a business-2-busines context.

ENGINYERIA ELECTRÒNICA ELÈCTRICA I AUTOMÀTICA

UNIVERSITAT ROVIRA I VIRGILI

Graduate Students Meeting on Electronics Engineering

Tarragona, Spain. June 19 - 20, 2014

Regular Sessions

3-D Finite-Element Optical Modeling of Interdigitated Heterojunction Organic Solar Cells

P. Granero[a], A. Raba[b], Y. Leroy[b], Anne-Sophie Cordan[b], V. S. Balderrama[a], J. Ferré-Borrull[a], J. Pallarès[a], and L. F. Marsal[a]*

[a]Nano-electronic and Photonic Systems (NePhoS), Department of Electronic, Electrical and Automatic Control Engineering, Universitat Rovira i Virgili, Av. Països Catalans 26 43007, Tarragona, Spain
[b]Laboratoire ICube, Univ. de Strasbourg/CNRS, 300 Bvd Sébastien Brant, Parc d'Innovation, BP 10413, F-67412 Illkirch, France
* Voice: +34 977559625, Fax: +34 977559605, E-mail address: lluis.marsal@urv.cat

1. Abstract

By means of 3-D finite-element numerical modeling, we analyze the influence of the incident light angle and polarization on the behavior of interdigitated heterojunction organic solar cells. We have performed simulations with different light source configurations. The nanopillar diameter and the radius of the circle that circumscribes the hexagon have also been varied to determine if the possible variations in the amount of absorbed light depend on the unit cell geometry. Results show that although there are some differences in the amount of the absorbed light, we can neglect them. So we can conclude that a single angle computation is enough to obtain accurate optical simulations for interdigitated OSC.

2. Introduction

Among other techniques, the interdigitated heterojunction approach has demonstrated to be a proper candidate to increase the efficiency of organic solar cells (OSC). This approach provides a proper exciton dissociation interface without sacrificing direct paths for carriers' collection [1], leading to a global improvement of the devices [2]. However, there is still a long way to optimize the cells and to realize their full potential. By means of 3-D finite-element numerical modelling [3], we investigate light absorption in interdigitated heterojunction full OSC for the case of poly(3-hexylthiophene) (P3HT) / 1-(3-methoxy carbonyl)-propyl-1-phenyl-(6,6)C_{61} (PCBM) devices. The aim of this work is to determinate if the angle and the polarization of the incident light must be take in account in the optical simulation models or it can be neglected. This work will help to understand the behaviour of the cells obtained in our facilities, which are achieved via nanoporous anodic alumina templates (NAAT) [4] (Fig.1).

3. Optical Modeling

From the NAAT templates we can obtain devices where the P3HT layer consists of a regular hexagonal distribution of nanopillars. Our computational domain is a 3-D model of one of this hexagonal unit cells (Fig.2). The model consists of a structure of indium tin oxide (ITO), Poly (3,4-ethylenedioxythiophene) poly(styrene sulfonate) (PEDOT:PSS), P3HT, PCBM and aluminium (Al). In order to determinate if the angle and the polarization of the incident light must be take in account in the optical simulation models or it can be neglected, we have perform simulations of different light source configurations. We also have varied the nanopillar diameter ($Ø_{NP}$) and the radius of the circle that circumscribes the hexagon ($Ø_{HEX}$) to determine if the possible variations in the amount of absorbed light depend on the unit cell geometry.

4. Results and Discussion

Fig. 3 shows the total power dissipation density as a function of the unit cell height (z-direction) along the centre of the nanopillar for several angles of polarization (ψ) and for several $Ø_{NP}$, $ØH_{EX}$ and wavelengths: a) $Ø_{NP}$ = 100 nm, $Ø_{HEX}$ = 500 nm, λ = 450 nm; b) $Ø_{NP}$ = 100 nm, $Ø_{HEX}$ = 300 nm, λ = 450 nm; c) $Ø_{NP}$ = 100 nm, $Ø_{HEX}$ = 150 nm, λ = 450 nm and d) $Ø_{NP}$ = 100 nm, $Ø_{HEX}$ = 500 nm, λ = 550 nm.

In all four cases the curves show a very similar behaviour for the different ψ, especially in the case of Fig. 3 B. For the other cases, we can find some differences in the amount of the absorbed light for each ψ. However, most of these small dissimilarities occur out of the active region, P3HT volume, that goes from z = 225 to 435 nm. Additionally, the differences that occur inside the active region, as we can see especially in Fig. 3 C, are very small. So, they will not affect the exciton generation rate and they can be neglected. Hence, we can conclude that a single angle computation is enough to obtain good optical simulations for interdigitated OSC. This fact allows reducing computation times without losing accuracy in the results.

Acknowledgements
This work was supported by the Spanish Ministry of Economy and Competitiveness (MINECO) under grant number TEC2012-34397 and by the Catalan Authority under project AGAUR 2014 SGR 1344.

References

[1] H. Hoppe, and N. S. Sariciftci, "Organic solar cells: An overview", J. Mater. Res., vol. 19, pp. 1924–1945, July 2004.
[2] D. Chen, W. Zhao, and T. P. Russell, "P3HT Nanopillars for Organic Photovoltaic Devices Nanoimprinted by AAO Templates", ACS NANO, vol. 6, pp. 1479–1485, February 2012.
[3] COMSOL (COMSOL Inc.), MA, USA. Available: http://www.comsol.com
[4] A. Santos, P. Formentín, J. Pallarés, J. Ferré-Borrull, and L. F. Marsal, "Fabrication and characterization of high-density arrays of P3HT nanopillars on ITO/glass substrates", Sol. Energy Mater. Sol. Cells, vol. 94, pp. 1247–1253, July 2010.

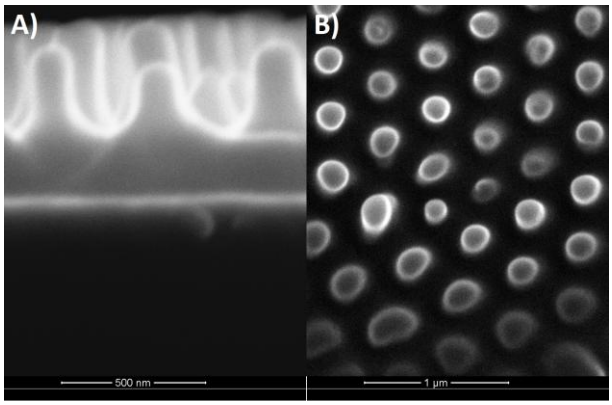

Fig.1. Environmental scanning electron microscopy images of P3HT nanopillars with the structure glass/ITO/PEDOT:PSS/ P3HT made with NAAT, a) cross section and b) top view.

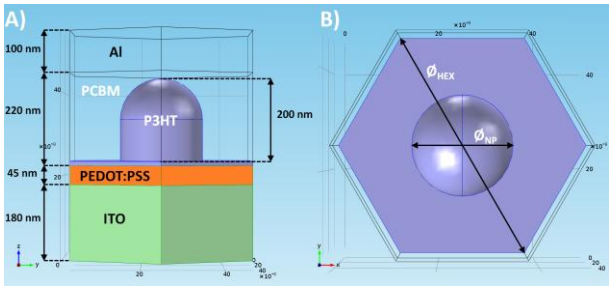

Fig.2. Schematic unit cell (periodic conditions) of the structure ITO/PEDOT:PSS/P3HT/PCBM/Al a) cross section and b) top view showing the geometrical characteristics. The residual layer of the nanopillar is 10 nm thick.

Fig.3. Total power dissipation density as a function of the unit cell height (z-direction) along the centre of the nanopillar for several angles of polarization (ψ) and for several $Ø_{NP}$, $Ø_{HEX}$ and wavelengths: A) $Ø_{NP}$ = 100 nm, $Ø_{HEX}$ = 500 nm, λ = 450 nm; B) $Ø_{NP}$ = 100 nm, $Ø_{HEX}$ = 300 nm, λ = 450 nm; C) $Ø_{NP}$ = 100 nm, $Ø_{HEX}$ = 150 nm, λ = 450 nm and D) $Ø_{NP}$ = 100 nm, $Ø_{HEX}$ = 500 nm, λ = 550 nm.

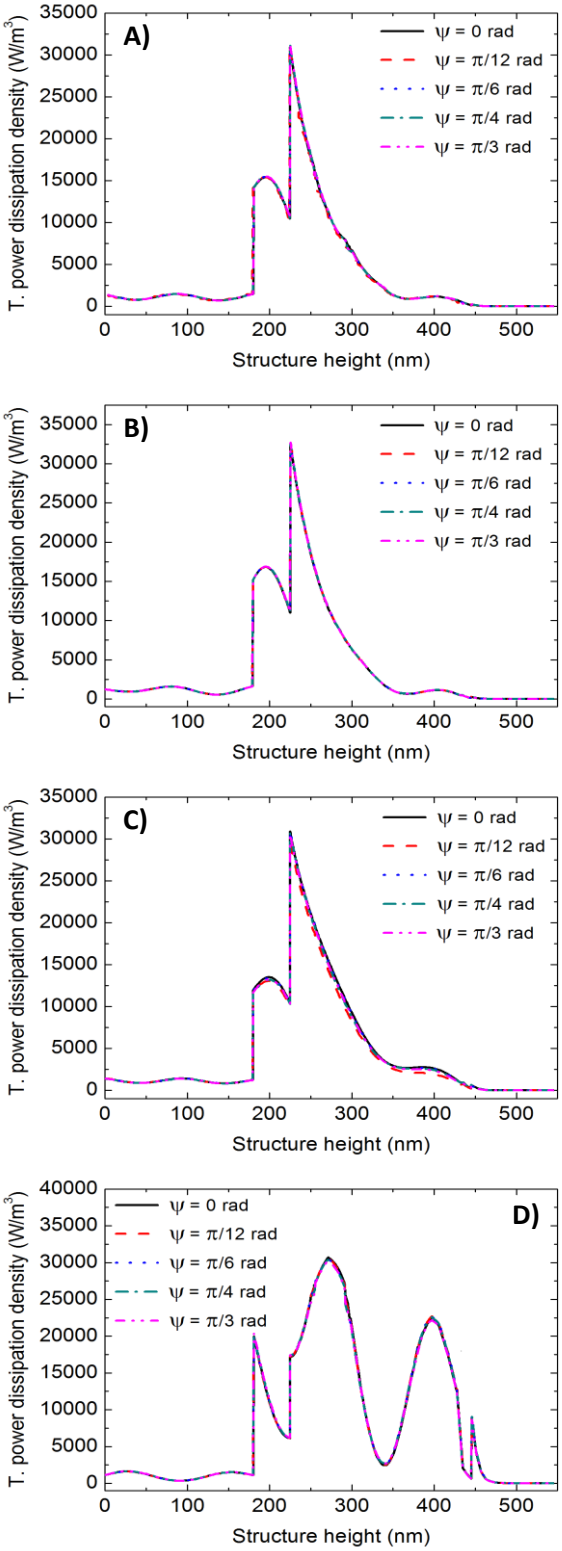

Engineering nanoporous anodic alumina label-free optical biosensors.

Gerard Macias, Josep Ferré-Borrull, Josep Pallarès, Lluís F. Marsal

Department of Electronic, Electric and Automatics Engineering,

Universitat Rovira i Virgili, Tarragona, Spain

Avda. Països Catalans 26, 43007; *E-mail: lluis.marsal@urv.cat; Tel: (34) 977 559625

Abstract

We report a study of the NAA biosensing capabilities. A NAA monolayer has been tested for serial detection of protein A and human IgG. Also, a NAA bilayer consisting in a high-porosity active layer and a low-porosity reference layer for self-compensation. Results show that NAA monolayers are able to detect proteins at 10 $\mu g \cdot mL^{-1}$ and NAA bilayers are able to inhibit protein entrance in the low-porosity layer.

1. Introduction

Label-free optical biosensors are devices capable of monitoring biomolecular binding in real time without the need of a fluorescent label. Among the optical techniques available, reflectance interference spectroscopy (RIfS) is one of the most sensitive.

RIfs monitors the interference oscillations arising from illuminating the film with white light. These oscillations depend on the effective optical thickness (EOT) of the film, which depends on both the refractive index (n) and the thickness (L) of the layer (EOT=2nL). Based on this concept, two different strategies have been used for the development of highly sensitive label-free biosensors. The first strategy consists in using a planar layer and monitoring the shift in the overall layer thickness [1]. The second strategy consists in using a porous thin film and monitoring the refractive index shift instead [2]. This latter technique allows higher ΔEOT due to the larger surface area available.

Among the available porous materials, nanoporous anodic alumina (NAA) is an ideal candidate. NAA is a cost-effective material obtained from the electrochemical etching of aluminium. It consists in an array of closed-packed uniform and parallel pores ordered in a honeycomb fashion. Furthermore, the structural morphology of NAA can be easily tuned by adjusting the electrochemical conditions [3]. One of the major advantages of NAA over other porous materials such as porous silicon (pSi) for the development of optical biosensors is its great stability at physiological pH [4].

Herein we report our recent advances in the development of NAA mono and double layer interferemetric optical biosensors.

2. Experimental section

Prior to anodization, Al substrates were electropolished in a mixture of EtOH and perchloric acid ($HClO_4$) 4:1 (v:v) at 20 V and 5 ºC for 4 min. Then, the electropolished Al substrates were cleaned in DI water, EtOH, DI water and dried under a stream of air. Subsequently, the first anodization step was performed in oxalic acid ($H_2C_2O_4$) 0.3 M at 40 V and 4-6 ºC for 20 h and cleaned with DI water, EtOH, DI water and dried under a stream of air. Then, the grown aluminium oxide was selectively dissolved in a mixture of phosphoric acid (H_3PO_4) 0.4 M and chromic acid (H_2CrO_4) 0.2 M at 70 ºC for 3 h. Afterwards, a second anodization was performed under the same anodization conditions and the time was adjusted in order to obtain the desired thickness. Finally, pores were widened by wet chemical etching in phosphoric acid (H_3PO_4) 5 % wt. at 35 ºC and the resulting samples cleaned in DI water, EtOH, DI water and dried under a stream of air.

3. Results

Fig.1 shows the cross section of a bilayer and a monolayer NAA interferometer.

In order to prove the capabilities of NAA membranes as optical biosensors, NAA monolayers were serially infiltrated with proteins in three steps. Step I corresponds to protein A (100 $\mu g \cdot mL^{-1}$), step II corresponds to human IgG (10 or 100 $\mu g \cdot mL^{-1}$). Fig. 2

shows the real-time measurement of ΔEOT during the experiment.

Further development of this technology requires self-compensation for environmental variations. For this reason, we developed the NAA bilayer. The NAA bilayer is composed of a high porosity top layer that allows the diffusion of proteins, and a low porosity bottom layer which hinders protein diffusion. This low porosity layer allows us to correct the signal from environmental conditions such as lamp or temperature fluctuations [5]. Fig. 3 shows the FFT of the reflectance spectrum before and after infiltration of bovine serum albumin (BSA). We observed how the signal from the bottom layer remained unaltered after BSA infiltration proving protein inhibition into the reference layer.

4. Conclusions

We have presented an optical interferometric biosensor consisting in a thin NAA film. NAA monolayers sensing possibilities have been proved by serially infiltrating protein A, human IgG and anti-human IgG. The NAA biosensor was able to detect the three proteins at 10 $\mu g \cdot mL^{-1}$.

We have also presented a NAA bilayer interferometer consisting of a high-porosity active layer and a low-porosity reference layer. Thanks to protein hindrance, this second layer is able to compensate environmental fluctuations.

We believe that these results are of great interest for the development of cheap optical biosensing devices.

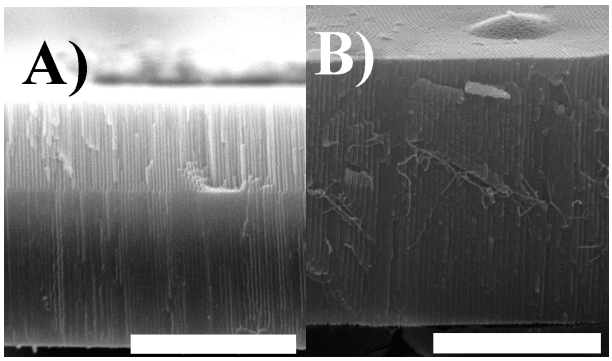

Fig. 1. SEM micrographs of the NAA films. A) bilayer NAA interferometer (scale bar = 4 µm) and B) monolayer NAA interferometer (scale bar = 3 µm).

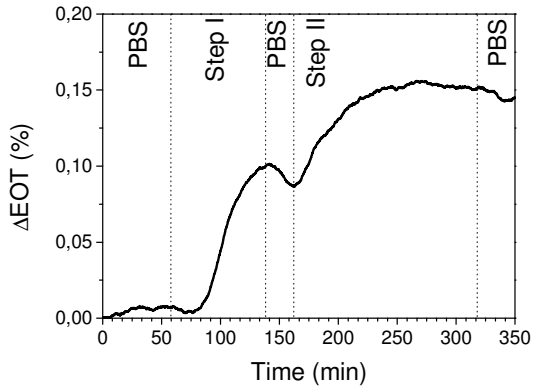

Fig.2. Real-time ΔEOT for NAA with a pore diameter of 51 ± 5 nm.

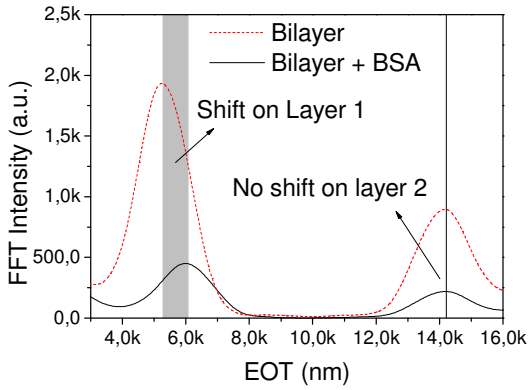

Fig.3. FFT of a NAA bilayer befote and after BSA infiltration.

Acknowledgements

This work was supported by theSpanish Ministry of Economy and competitiveness (MINECO) under grant number,TEC2012-34397 and by Catalan authority under project AGAUR 2014 SGR 1344.

References

[1] J. Piehler, A. Brecht, G. Gauglitz, "Affinity detection of low molecular analytes." Anal. Chem. 68, 139-143, 1995.

[2] V. S.-Y. Lin, K. Motesharei, K.-P. S. Dancil, M. J. Sailor, M. R. Ghadiri, "A porous silicon-based optical interferometric biosensor." Science, 278, 840-843, 1997.

[3] Rahman M. M., Garcia-Caurel E., Santos A., Marsal L. F., Pallarès J., Ferré-Borrull J. "Effect of the anodization voltaje on the pore-widening rate of nanoporous anodic alumina." Nanoscale Re. Lett., 7, 474-7, 2012.

[4]S.D. Alvarez, C.-P. Li, C. E. Chiang, I. K. Schuller, M. J. Sailor. "A label-free porous alumina interferometric immunosensor." ACSNano, 3, 3301-3307, 2009.

[5]Macias G. Hernández-Eguía L. P., Ferré-Borrull J., Pallarès J., Marsal L. F. "Gold-Coated Ordered Nanoporous Anodic Alumina Bilayers for Future Label-Free Interferometric Biosensors." ACS Appl. Mater. Interfaces, 5, 8093-8098, 2013.

Comparison of Several Dithering Signals in Extremum Seeking Control for MPPT Operation of PV Panels

Hector Zazo and Ramon Leyva

Department of Electronic, Electrical and Automatic Control Engineering
University Rovira i Virgili
Av. Paisos Catalans, 43007 Tarragona (Spain)
Phone/Fax number:+0034 977557049/9605, e-mail: hector.zazo@urv.cat

Abstract

The paper evaluates MPPT performances for PV panels. Specifically, it focus on MPPT methods based on Extremum Seeking Control and compares the performances for three different dithering signals; namely, a sinusoidal, a triangular and a squared signal.
The comparison is carried out by means of PSIM simulations as long as experimental measurements using a photovoltaic array BP858-F.

1. Introduction

MPPT (Maximum Power Point Tracking) methods are often used in a variety of renewable energy domains. Their purpose is to extract the optimal power from renewable sources. Among other Extremum Seeking Control (ESC) is a very used approach to design MPPT controllers. A good recent reference on ESC is [1]. The adaptation of ESC to converter domains can be found in references [2-3] among others. Common ESC uses a sinusoidal signal to perturb the system. And this dithering signal is used to update the searching sense and magnitude. This paper aims at the assessment of ESC technique when the dithering signal is not a sinusoidal signal but a triangular or square signal. Thus, along the paper, we compare advantages and disadvantages of using each dithering signal.

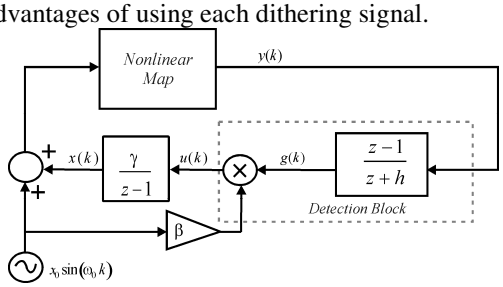

Fig. 1. ESC schema

ESC block diagram, that is shown in fig. 1, must ensure that the nonlinear map $y = f(x)$ operates at its optimal point; that is its input $x(k)$, and its output $y(k)$ tend to its optimal values. We assume that the nonlinear map $y = f(x)$ has a single maximum and is concave; or equivalently, $\frac{\partial^2 f}{\partial x^2} < 0$. ESC principle consist in adding a dithering signal $p(k) = x_0 \sin(\omega_0 k)$ at the input in order to estimate the gradient of the nonlinear map, which in fig.1 corresponds to *u(k)*. The gradient estimation is obtained by filtering the output $y(k)$ by a high-pass filter and multiply the filter output $g(k)$ by β times the dithering signal $p(k)$. Finally the gradient estimation is integrated to approaching $x(k)$ to its optimal value. It can be shown that the transient values of $x(k)$ depend on the gradient in the current time of the gradient $\frac{\partial f}{\partial x}(k)$, the average square value (and consequently, its value rms) of the dithering signal $\langle p^2(k) \rangle$ and the gain β.

When ESC is applied as MPPT technique in a photovoltaic array, the input $x(k)$ corresponds to the array voltage, and its output $y(k)$ corresponds to the supplied power.

2. Simulation Results

In order to evaluate performances for each dithering signal, our MPPT controller has been implemented in a DSP-PIC30F2020, which allows us a fast enough conversion A/D, and incorporates a digital PWM that drives the switches of the DC-DC converter, which force the desired voltage at the PV panel terminals. Besides, we simulate the proposed hybrid circuit by means of PSIM.

Next figures show transient behavior of MPPT signal for start-up and several abrupt irradiance changes. We use the same MPPT parameters for all the experiments with different dithering signals. MPPT parameters will be provided in the final version. Simulation results are summarized in fig. 2, that shows the array voltage when dithering signal are squared (in green), triangular (in red) and sinusoidal (in blue). It shows the transient waveforms for start-up, for a irradiance change from

500W/m^2 to 1500W/m^2 at 0.6 s, and for a irradiance change from 1500W/m^2 to 1250W/m^2 at 0.9s. We consider the temperature is 25ºC along all the simulation.

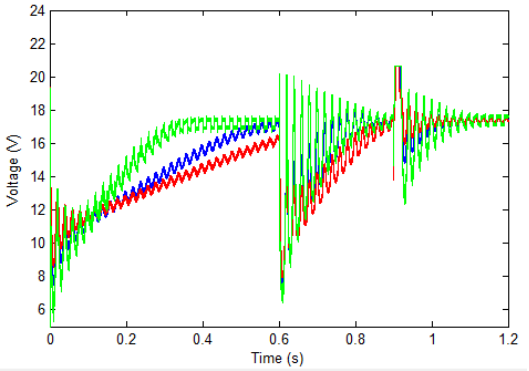

Fig. 2. PV panel voltage waveforms (red: triangular ESC, green: square ESC, blue: sinusoidal ESC)

It can be appreciated that start-up for the square case is the fastest and the triangular case the slowest. It is a consequence of the fact that the rms value for the same amplitude is the biggest in the square case and the smallest in the triangular case. Nevertheless, we can comment as a disadvantage that , for the same reason, the squared signal exhibits a less damped transient and therefore implies a greater stress in the DC-DC converter.

3. Experimental results

We have reproduced experimentally the start-up over a 100 W prototype; results are shown in figures 3, 4 and 5.

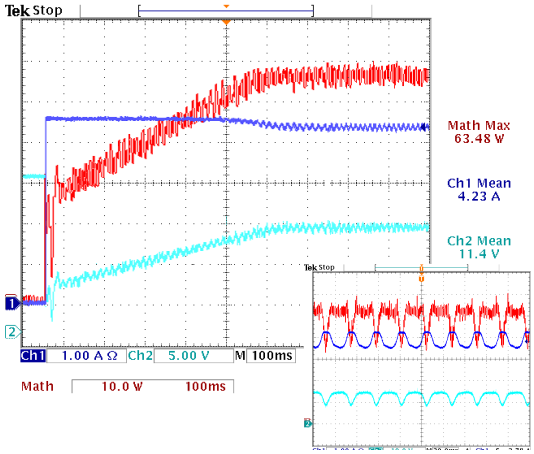

Fig. 3. Sinusoidal-Signal Extremum Seeking Control.

It can be appreciated by comparison of the three figures that, as expected, square case is the faster exhibiting a settlement time of 0.4 s approximately. The settlement time is 0.55 s and 0.65 s approximately for the sinusoidal case and triangular case, respectively. Figures 3, 4 and 5, also, show a detail of the permanent regime waveforms. In all the cases, we can assure that the optimal point is achieved since the voltage signals (cyan) and current signals (blue) are in counterphase. MPPT efficiencies are similar in all the cases.

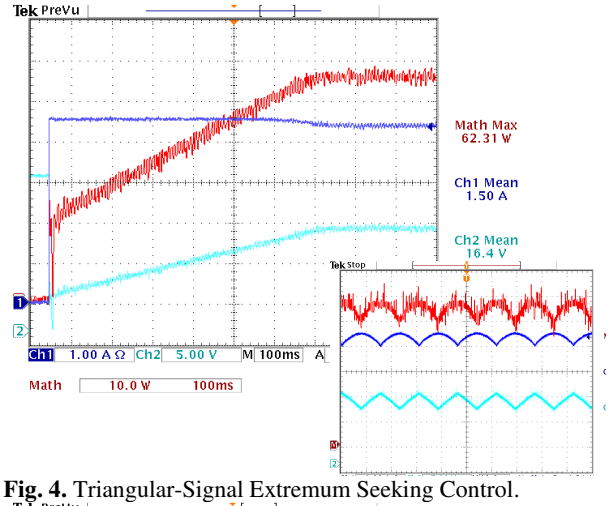

Fig. 4. Triangular-Signal Extremum Seeking Control.

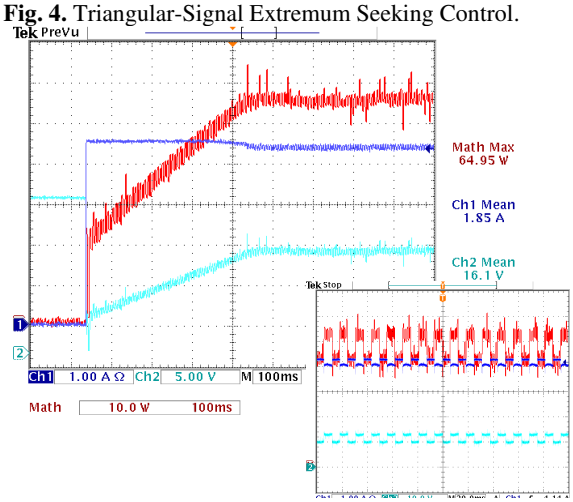

Fig. 5. Square-Signal Extremum Seeking Control.

4. Conclusions

The paper compares the performances of a MPPT controller based on ESC for sinusoidal, triangular and square dithering signals. The different perturbed MPPTs are applied for PV generation. Simulation and Experimental results conclude that square-dithering MPPT is the fastest, although has a less damped behavior.

References

[1] Ariyur, K.B.; Krstic, M.; “Real-Time Optimization by Extremum-Seeking Control”. New York: Wiley, 2003.

[2] Leyva, R.; Artillan, P.; Cabal, C.; Estibals, B.; Alonso, C.; "Dynamic performance of maximum power point tracking circuits using sinusoidal extremum seeking control for photovoltaic generation" International Journal of Electronics, vol.98,nº 4, pp. 529- 542, 2011

[3] Leyva, R.; Olalla Martinez, C.; Zazo, H.; Cabal, C.; Cid Pastor, A; Queinnec, I.; Alonso, C; “MPPT based on Sinusoidal Extremum Seeking Control in PV Generation”, International Journal of Photoenergy, vol. 2012, article ID 672765

Hybrid electronic system based on multisensor data fusion for milk ageing analysis

Z. Haddi[a,b], M. Bougrini[a,c], K. Tahri[a], T. Saidi[a], N. El Bari[d], E. Llobet[b], N. Jaffrezic-Renault[c], B. Bouchikhi[a]

[a]*Sensor Electronic & Instrumentation Group, Moulay Ismaïl University, Faculty of Sciences, Physics Department, B.P. 11201, Zitoune, Meknes, Morocco*
[b]*MINOS-EMaS, Electronic Engineering Department, Universitat Rovira i Virgili, Avda. Països Catalans, 26, 43007 Tarragona, Spain*
[c]*Université de Lyon, Université Claude Bernard Lyon 1, Institut des Sciences Analytiques, UMR CNRS 5280, 5, rue de la Doua, 69100, Villeurbanne cedex, France*
[d]*Biotechnology Agroalimentary and Biomedical Analysis Group, Moulay Ismaïl University, Faculty of Sciences, Biology Department, B.P. 11201, Zitoune, Meknes, Morocco*

Summary

The combined application of a hybrid e-nose and a voltammetric e-tongue to get additional chemical information from liquid samples through the analysis of the solution and its headspace is illustrated and discussed. The hybrid e-nose together with the voltammetric e-tongue was used for the evaluation of the evolution in the course of time of pasteurized milk samples. Artificial sense data have been elaborated by Principal Component Analysis (PCA) and Support Vectors Machines (SVMs). The results of the data fusion reveal a net classification of all the storage days.

Motivation

Data fusion approach can successfully merge individual data from multiple origins to draw the right conclusions that are more fruitful when compared to the original single data. Hence, this work has demonstrated that data fusion strategy used to combine e-nose and e-tongue signals led to a system of complementary and comprehensive information of the pasteurized milk which outperformed the performance of each instrument when applied separately.

Results

The hybrid e-nose used for this study consisted of two sensor arrays, the first one comprised four micro-machined gas sensors[1] and the second array consisted of four commercial tin-dioxide gas sensors: TGS 8xx (with xx = 15, 22, 24 and 42) obtained from Figaro Engineering. The voltammetric e-tongue was formed with four working electrodes (Platinum, Gold, Glassy Carbon and Silver). Samples of pasteurized milk were stored in a refrigerator at a constant temperature of 4 ° C until their analysis in days 1, 2, 3, 4 and 5. The PCA method was applied to the dataset of hybrid e-nose, which showed 74.34 % of the total variance (Fig. 1). As can be inferred by the results shown in this score plot, there is a certain area of overlapping in which no clear differentiation can be made between samples of the 2nd and the 3rd storage days. Fig. 2 reports the projections of the experimental results on 3D space formed by the first three PCs which explained 80.46% of data variance of the voltammetric e-tongue. The samples of the first three days are not sufficiently separated. Thus, when the electronic devices were applied separately to the study of the different spoilage states of the pasteurized milk, no clear storage day's discrimination can be drawn. To exploit the combination of the two instruments, the *Mid-level of abstraction* data fusion has been conducted and therefore yielded perfect classification of all the storage days (see Fig. 3). Furthermore, the SVMs reached a 100 % success rate in the identification of the five storage days (Table 1).

---

[1] Ionescu R, Espinosa EH, Sotter E, Llobet E, Vilanova X, Correig X et al., Oxygen functionalisation of MWNT and their use as gas sensitive thick-film layers. *Sensors and Actuators B* **113**: 36-46 (2006).

Figures

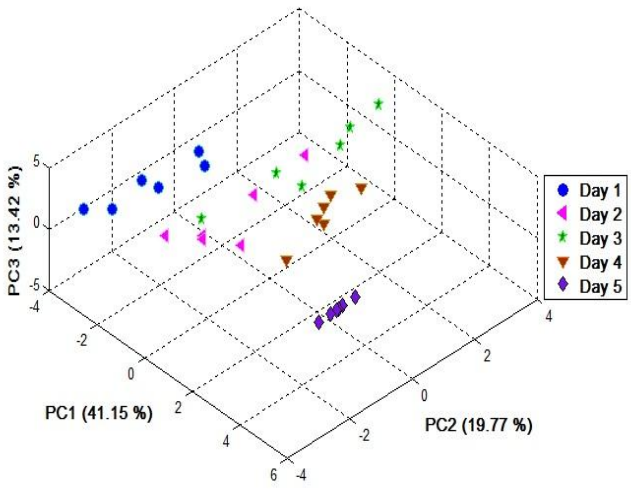

Fig. 1. Three-dimensional PCA plot performed on the samples gathered using the hybrid e-nose during five days of cold storage of pasteurized milk

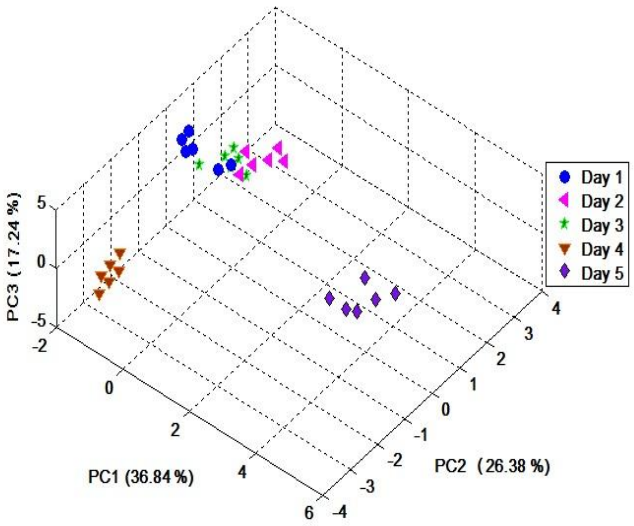

Fig. 2. Three-dimensional PCA plot performed on the samples gathered using the voltammetric e-tongue during five days of cold storage of pasteurized milk

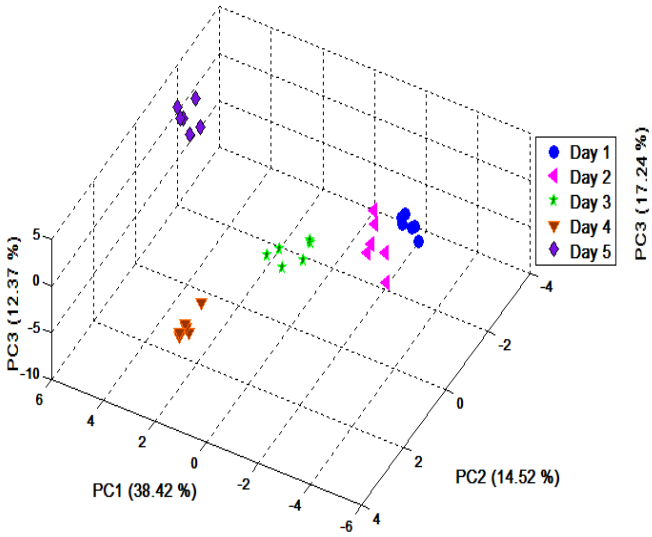

Fig. 3. Three-dimensional PCA plot performed on the five storage days of pasteurized milk measurements gathered using *Mid-level of abstraction* data fusion of the hybrid e-nose and the voltammetric e-tongue.

Table 1 SVM classification results

Actual	Predicted				
	Day 1	Day 2	Day 3	Day 4	Day 5
Day 1	6				
Day 2		6			
Day 3			6		
Day 4				6	
Day 5					6

Use of a CNT-coated piezoelectric cantilever with double transduction as a gas sensor for benzene detection at room temperature

P. Clément[1,2], E. Llobet[1], C. Lucat[2],H. Debéda[2]

[1]*Minos-EMas, Rovira i Virgili University, Tarragona, Spain*
[2]*IMS, Bordeaux University, Talence, France*

Pierrick Clément, Departament d'Enginyeria Electrònica, Elèctrica i Automàtica, Universitat Rovira i Virgili
Avinguda dels Països Catalans, 26 Campus Sescelades, 43007 TARRAGONA (Spain)
Tel. +34 977 256 572, e-mail: pierrick.clement@urv.cat

Abstract

In this work, we propose to use a screen-printed piezoelectric cantilever with double transduction. Indeed, the piezoelectric cantilever is used as a resonant type sensor coated with carbon nanotubes (CNTs) as sensitive layer. Then, the resistance of CNTs is measured in static mode in parallel thanks to a modification of the cantilever top electrode. The combination of the CNTs equilibrium conductivity measurement and the resonance frequency shift of the 31-longitudinal mode allow the use of this device as a chemical gas sensor for benzene detection. The responses towards benzene concentrations under different relative humidity backgrounds are discussed.

1. Introduction

It is known that thanks to their high sensitivity, resonant microcantilevers are used for many applications including gas sensor. Au/PZT/Au cantilevers (2x8x0.1mm3) with sandwich electrodes (Fig.1.) are fabricated on an alumina substrate by associating the screen-printing technique with the sacrificial layer process [1].

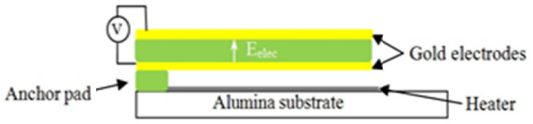

Fig.1. Self-actuated and self-readout PZT cantilever basic principle.

Thanks to the piezoelectric effect, they integrate both self-actuating and self-read-out functions. Their basic principle is explained by a competition between stress and mass effect due to the adsorption of the target gas on the sensitive coating leading to a resonance frequency shift. Also, unlike in typical silicon cantilevers, a high frequency 31-longitudinal mode is used in order to reach higher sensitivity [2] for gas sensing application [3]. CNTs are good candidates as sensitive layer since they have high specific area (up to 1800 m2/g in single wall CNTs) and the possibility to be chemically functionalized and metal decorated. In this device, they play also the role of transducer since the equilibrium conductivity of CNTs changes (translate into resistance shift) with the adsorption of the target gas on the nanotube sidewalls [4].

2. Experimental setup

For simultaneous resonance frequency shift and resistance variation measurements of the CNTs coating, the top rectangular electrode is replaced by two interdigitated electrodes (Fig.2.).

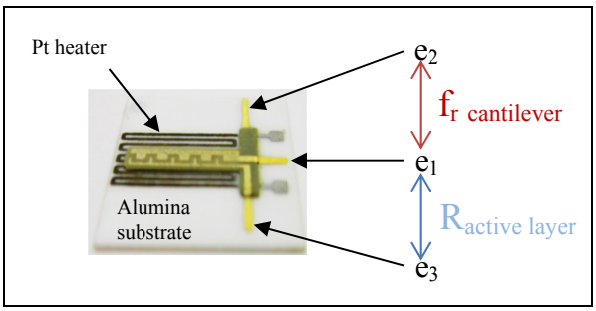

Fig.2. Picture showing the double transduction method where the bottom electrode is e_2 and the interdigitated electrodes are e_1 and e_3.

The piezoelectric properties of this new cantilever measured with an Agilent E5061B impedance meter show a resonant frequency fr≈70 kHz with a high quality factor Q≈1500 for the first 31-longitudinal mode. The CNTs are multiwall types obtained by

chemical vapor deposition and functionalized by oxygen-argon plasma to improve their surface reactivity (named O-MWCNTs). The monitoring of the resistance of CNTs layer during the deposition is made for achieving resistances of a few tens of ohms. After the CNTs drop coating, a negative resonance frequency shift of few hundreds Hertz is observed because of the predominant cantilever mass effect (Fig.3.).

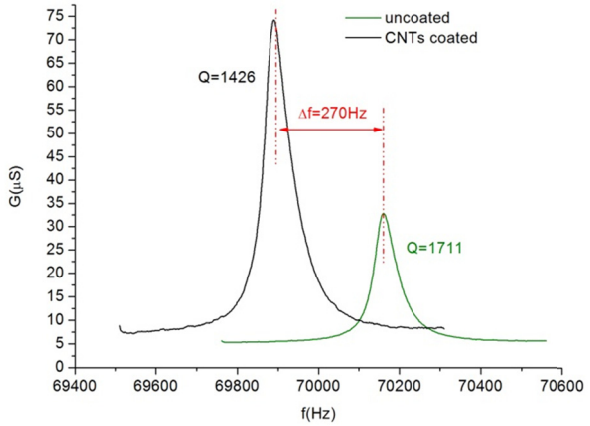

Fig.3. Conductance of the PZT cantilever at the resonance frequency before and after CNTs deposition

3. Results and conclusion

First results show a positive shift of the resonance frequency due to a stress effect under benzene with low noise thanks to a high quality factor and a LOD≈2.8 ppm. The resistance shifts of CNTs shows a LOD≈50ppm (Fig.4.).

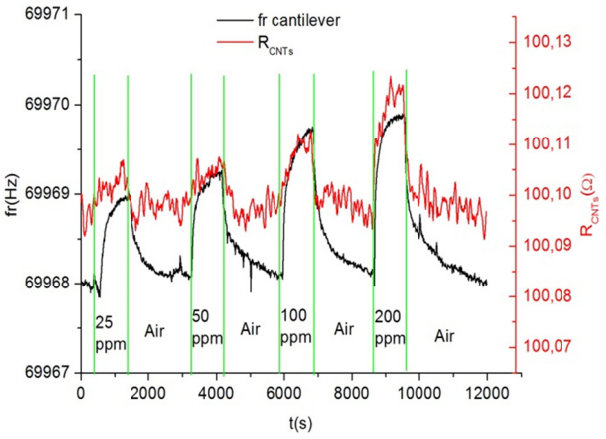

Fig.4. Response under benzene of CNTs coated PZT cantilever at room temperature.

The effect of relative humidity changes has been also investigated. Here negative shifts are observed due to the fact that a wide change in the relative humidity content has been studied (see Fig.5.).

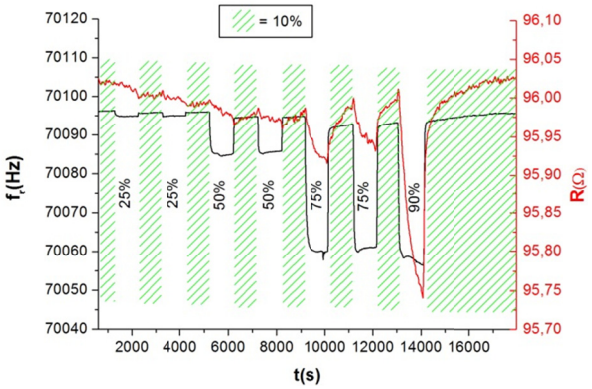

Fig.5. Response under humidity of CNTs coated PZT cantilever at room temperature.

Finally, a new device with double transduction has been made successfully. Current measurements are done for the detection of benzene with presence of different moisture content in order to study the device in real conditions.

References

[1] C. Lucat, P. Ginet, C. Castille, H. Debéda, and F. Ménil, "Microsystems elements based on free-standing thick-films made with a new sacrificial layer process," *Microelectronics Reliability,* vol. 48, pp. 872-875, 2008.

[2] I. Dufour, F. Josse, S. M. Heinrich, C. Lucat, C. Ayela, F. Ménil, and O. Brand, "Unconventional uses of microcantilevers as chemical sensors in gas and liquid media," *Sensors and Actuators B: Chemical,* vol. 170, pp. 115-121, 2012.

[3] J. Zhou, P. Li, S. Zhang, Y. Long, F. Zhou, Y. Huang, P. Yang, and M. Bao, "Zeolite-modified microcantilever gas sensor for indoor air quality control," *Sensors and Actuators B: Chemical,* vol. 94, pp. 337-342, 2003.

[4] I. Hafaiedh, P. Clément, H. Baccar, E. Llobet, and A. Abdelghani, "Functionalised multi–walled carbon nanotubes for chemical vapour detection," *International Journal of Nanotechnology,* vol. 10, pp. 485-495, 2013

This work is funded in part by CTP-DGR under grant no. 2011CTP00015.

Automatic Compound Deconvolution and Alignment in Comprehensive Double Gas Chromatography - Mass Spectrometry by Blind Source Separation

Xavi Domingo[†], Francesc Fernandez[‡], Nicolau Cañellas[†], Alexandre Perera[‡], Xavier Correig[†] and Jesus Brezmes[*]

[†] * Signal Processing in Omic Sciences (SIPOMICS). Metabolomics Platform,
Department of Electronic, Electrical and Automatic Control Engineering. Universitat Rovira i Virgili, Tarragona, Catalonia.
[‡] Bioinformatics and Biomedical Signals Laboratory (B2SLab), Centre de Recerca en Enginyeria Biomèdica (CREB),
Universitat Politècnica de Catalunya, Barcelona, Catalonia.
* Corresponding author. Email: jesus.brezmes@urv.cat

Nowadays, comprehensive double gas chromatography - mass spectrometry (GCxGC-MS) can be considered as a mature analytical technique at least on the hardware side. On the other hand, there is still much room for improvement on the software side, specially in automatic methods for high-throughput data processing of GCxGC-MS measurements. This is due to the fact that, despite the particular capability of GCxGC-MS to increase chromatographic resolution, co-elution of some compounds still occurs and makes it difficult to quantify and identify co-eluted components in each measurement.

In this study we introduce a novel approach to automatically process the samples of a complete GCxGC-MS measurement set based on blind source separation techniques. This processing involves compound deconvolution, compound alignment across samples and compound identification. The designed algorithm uses independent component regression (ICR) [1] applying non-negativity and unimodality constraints. After compound profiles and spectra are extracted, they are aligned across samples and identified against a spectra reference database.

The method deconvolves all the compounds of each sample in the experiment in a first step called factor extraction. An algorithm based on independent component analysis (ICA) is used to perform a true deconvolution of the mixture of compounds in data. Compound profile models are extracted by non-negative unimodal independent component analysis. Non-negative and unimodality constraints are applied to the ICA outcome to obtain chemically meaningful results in its application to chromatographic data. Concentration and spectra matrices are determined by non-negative least squares.

For each modulation cycle, three steps are applied to resolve the mixture: (1) Estimation of number of independent components with a principal component analysis (PCA). (2) Compound profile model extraction using non-negative unimodal independent component analysis. (3) Profile and spectra extraction by non-negative least squares regression

In a second stage, the factors (compounds) found in the different samples are aligned. The algorithm groups the extracted factors across the different samples according to their distance in the retention time and their correlation distance between their spectra with the restriction that compounds from the same sample cannot be clustered together.

Finally, the aligned factors are identified by comparing their spectra against a reference database such as the Golm metabolome database (GMD). Also, data can be statistically analyzed to retrieve significant variations of the deconvolved compounds between the existing classes or conditions in the experimental design.

A dataset composed of four replicates of a mixture of 30 pure metabolite standards, whose spectra is included in the Golm Metabolome Database GMD [3], was analyzed by the presented method. Comparing their spectra against the GMD spectra database correctly identified all the standards in the mixture. This shows the capability of the method to deconvolve and retrieve the different compounds spectra.

This study shows the applicability of ICR to the deconvolution of chromatographic signals, especially with GCxGC-MS samples. The automatic deconvolution of multiple samples is of special interest for high-throughput data analysis in untargeted metabolomics. An R package is currently under development. This package performs the complete GCxGC-MS data analysis workflow: compound deconvolution, alignment, identification and quantification. The package aim is to identify changes between experimental conditions in untargeted metabolomics oriented experiments.

REFERENCES

[1] Xueguang Shao, Wei Wang, Zhenyu Hou, and Wensheng Cai (2006). A new regression method based on independent component analysis. *Talanta*, **69 (3)**, 676-680.

[2] Xueguang Shao, Zhichao Liu, and Wensheng Cai (2009). Extraction of chemical information from complex analytical signals by a non-negative independent component analysis, *Analyst*, **134 (10)**, 2095-2099.

[3] Hummel, J., Strehmel, N., Selbig, J., Walther, D. and Kopka, J. (2010) Decision tree supported substructure prediction of metabolites from GC-MS profiles. *Metabolomics*

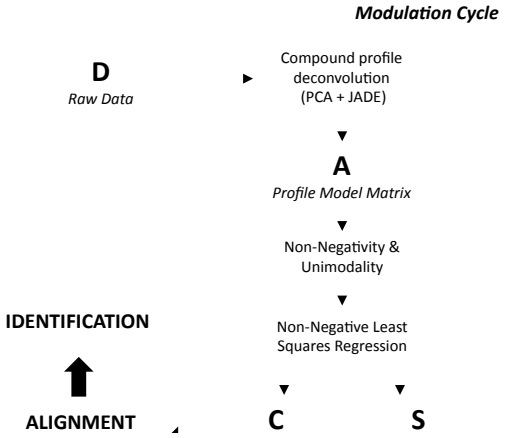

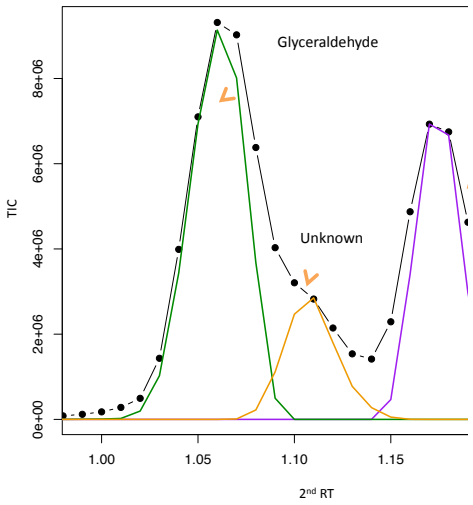

Fig. 2. Resolution of a mixture compound co-elut acid, glyceraldehyde and an unknown metabolite (not in database) appear co-eluted. The method is capable of re tration profile.

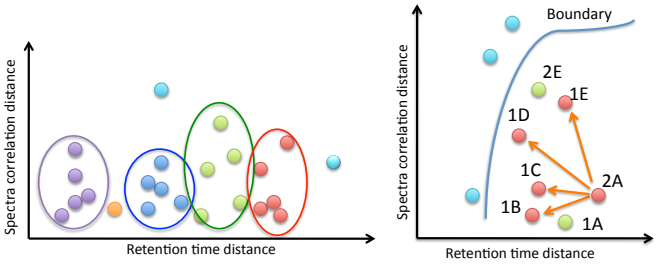

Fig. 3. Scheme of the alignment algorithm aim. The spheres represent the different compounds in different samples. Their proximity in terms of correlation and time is represented in the axis. In the right picture, the numbers represents the number of the same actual compound in a single sample. The letters represent the different samples.

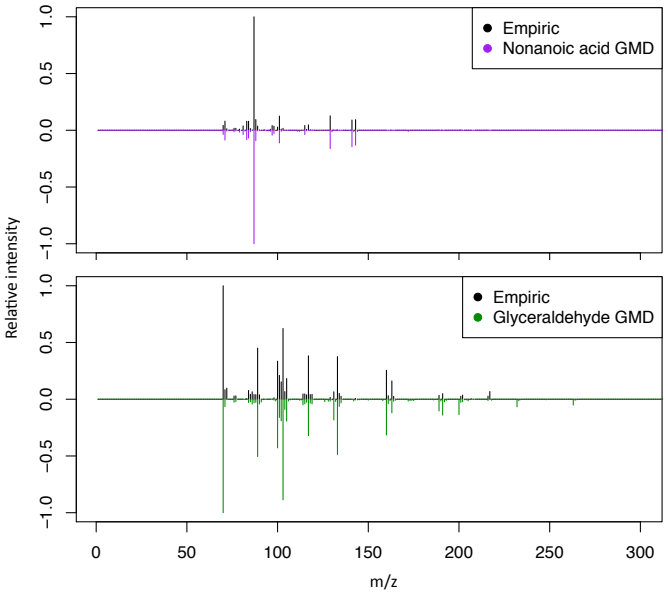

Fig. 4. Resolution of the spectra for the case presented in figure 2. The method proves to be capable of determining the different compound spectra

Analysis and Design of AC-DC PFC with Low THD

M. Bodetto, A. El Aroudi, A. Cid-Pastor, and Luis Martínez-Salamero.
Department of Electronics, Electrical Engineering and Automatic Control
Universidad Rovira i Virgili. Tarragona, Tarragona , SPAIN
E-mails: {mirko.bodetto, angel.cid, abdelali. elaroudi, luis.martinez}@urv.cat

***Abstract*- Most AC-DC converters exhibits harmful harmonic distortion in the input line current waveform near de zero voltage crossing. Even this distorted signal is observed imposing a behave as a Loss Free Resistor under SMC. This paper propose two techniques to reduce this distortion using an AC-DC converter under SMC. The first one consists of a PI controller applied to the switching function. The second option consists of a time varying hysteresis width which is made enough small as the input voltage approaches zero. An improvement has been obtained with the second technique, thus this technique has been validated by means of numerical simulations, and experimental verification.**

1. Introduction

Power factor correction (PFC) circuits are used in many industrial applications. For this purpose, switch-mode DC–DC converters, working as PFC circuits, are used to ensure a high power factor at the mains side [1]. The power quality is determined by the international standards such as EN 61000-3-2 [2].

Many DC-DC converters with non pulsating input current can be used in PFC applications. However, high-order schemes such as Ćuk and SEPIC converters are needed in single-stage PFC applications.

In many research studies the PFC is performed by a Sliding-Mode Control (SMC) [3, 4] in such a way that the input voltage is proportional to the input current in average ($i_1 = g \cdot v_g(t)$), where g is a suitable design parameter.

The SMC is implemented by a hysteretic comparator to limit the switching frequency to practical values. However as can be seen in [5] a harmful harmonic distortion takes place near the zero crossing of the input voltage, due to the system enters into the discontinuous conduction mode (DCM) operation in this critical area.

To mitigate this problem, has been proposed two techniques; the first one consists of a PI controller applied to the switching function. The second option consists of a time varying hysteresis width [6] which is made enough small as the input voltage approaches zero.

The rest of the study is organized as follows: a system description and stability analysis are presented in Section II. Numerical simulations are reported in Section III, experimental verification is presented on Section IV. Finally the conclusions and future research lines are summarized in Section V.

2. System Description And Stability Analysis.

Fig. 1 shows a circuit diagram of the system under study. It consists of a high order DC-DC converter under a SMC.

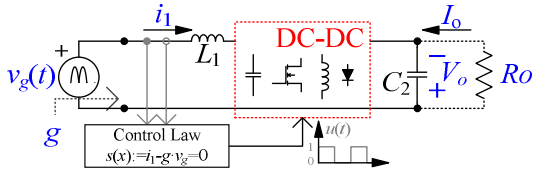

Fig. 1 Block diagram of an AC–DC switching converter for PFC.

The sliding surface is selected such that the input current i_1 is proportional to the input voltage v_g. Thus the switching surface is described (1) where $g=1/r$.

$$s(x) := i_1 - g \cdot v_g = 0 \tag{1}$$

The system works in Continuous Conduction Mode (CCM). In this operation mode, the system switches between two different topologies that can be described by a system of differential equations corresponding to the two states of the MOSFET S_1 ON ($u(t)=1$) or OFF ($u(t)=0$). The system state equations are expressed as follows

$$\begin{aligned} \dot{x} &= A_1 x + B_1 \quad \text{for} \quad u = 1 \\ \dot{x} &= A_2 x + B_2 \quad \text{for} \quad u = 0 \end{aligned} \tag{2}$$

where $x = (i_1, i_2, v_1, v_2)^T$ is the vector of state variables. The matrices A_i, and vectors B_i are state matrices and input vectors of the Ćuk and SEPIC converters. Mathematical analysis is performed in the same way as in [5, 7] respectively.

The equilibrium point results from the intersection of ideal dynamics sliding curve, and are detailed below:

$$\begin{aligned} Xss_{Cuk} &= [g \cdot v_g \quad g \cdot v_g^2 / V_2 \quad v_g + V_2 \quad V_2]^T \\ Xss_{SEPIC} &= [g \cdot v_g \quad g \cdot v_g^2 / V_2 \quad v_g \quad V_2]^T \end{aligned} \quad , \quad V_2 = v_g \sqrt{g \cdot Ro} \tag{3}$$

Applying the Routh-Hurwitz criterion, one can determine that the system is locally stable for all values of v_g>0. Therefore the harmonic distortion observed in the zero crossing voltage area is attributed to a loss of sliding mode regime due to DCM caused of a decrease in the switching frequency.

3. Numerical Simulations

Numerical simulations have been performed using PSIM.

To alleviate the problem of distortion near the zero crossing, it has been used two possible solutions which are shown in Fig. 2. The first one consists of a PI controller applied to the switching function $s(x)$ to compensate the error between the input current and its reference when the system fails to perform the switching due to the DCM (Fig. 2a). However another kind of distortion in the input current $i_1(t)$ waveform is caused by this controller [5]; so that the power factor (PF) and total harmonics distortion (THD) are negatively affected, therefore this option was not implemented.

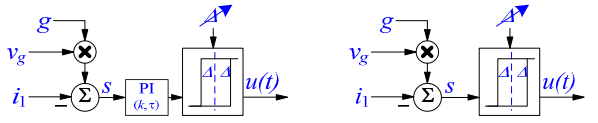

b) With a PI compensator. c) Variable hysteresis width Δ.

Fig. 2 Block diagram of the both controls.

The second option is made the hysteresis width approach to zero as v_g approaches zero (Fig. 2b), thereby narrowing the width Δ which implies an increase of the switching frequency.

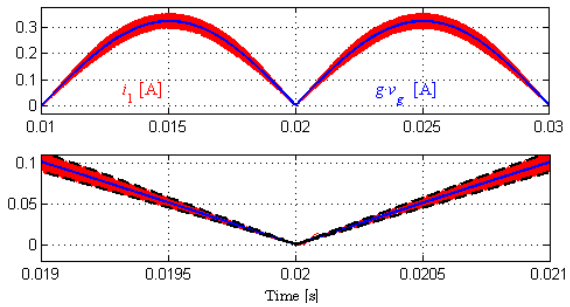

Fig. 3 Effects of the SMC with variable hysteresis width.

If the system is controlled with a variable hysteresis window, one can observe that the input current ripple is decreased near the zero crossings as can be seen in Fig. 3. This is due to the increased value of the switching frequency caused by a decrease of the hysteresis width in this region. In this way obtaining an improvement in the PF and thus the system behaves as near ideal LFR. The improved between conventional control to control variable windows width are shown in TABLE I

TABLE I SYSTEM UPGRADE

	Δ		Improvement	Relative Improvement %
	i_{in}	i_{in}		
THD %	8.825	6.289	2.5350	28.732
PF (vg-i1)%	99.612	99.802	0.1899	0.191

4. Experimental Verification

A prototype of the proposed control and power converter has been implemented to confirm the theoretical and simulation results. The prototype has been performed to verify the operation of both controls, proposed and conventional control. Values of the components used in the prototype are detailed in [5].

The experimental measurements is shown Fig. 4. It can be seen the waveforms of the input variables as: input voltage (v_g), input current (i_1), input power (p_i), their average or RMS values are shown in the same figure. It can be observed a perfect proportionality between input current and input voltage. This input variable is related by input conductance $g = ks \cdot G$, where ks is a voltage sensor gain. This gain was chosen in 1/5000.

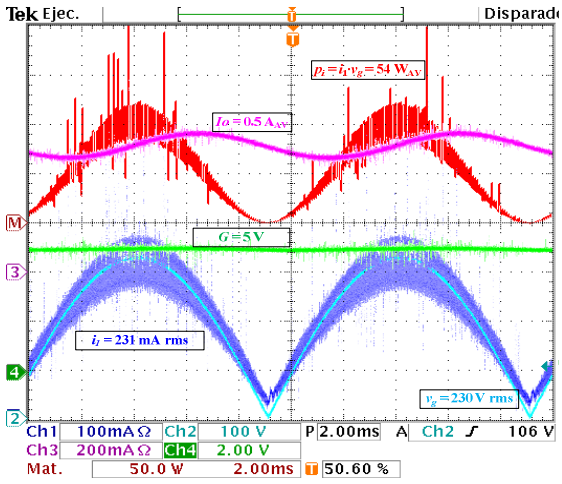

Fig. 4 Waveforms of the input i_1 and output currents I_o, input voltage v_g, line current i_{in}, input power p_i, conductance reference G, with a variable hysteresis width Δ.

Additionally, these features are also observed when a feedback is used to control the output current. The results with a closed output current loop are shown in Fig. 5; where it can be observed that the load current tracks the reference current (I_{ref}) while the input variables maintain the proportionality between the input variables imposed by the SMC.

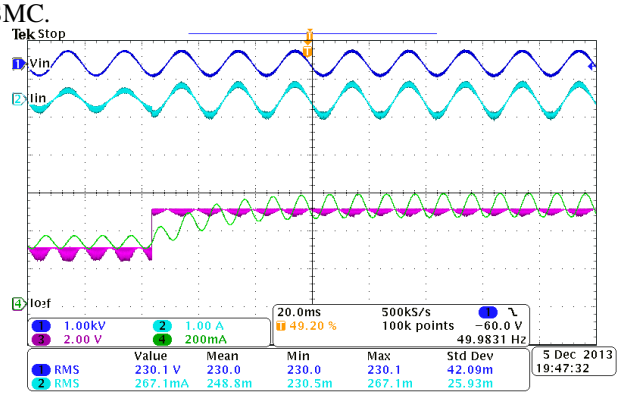

Fig. 5 Waveforms of the output currents with a closed output current loop: line voltage v_{in}, line current i_{in}, output current reference I_{ref}, output current Io.

5. Conclusions

The harmonic distortion near zero crossing can cause harmful effects in PFC converters. In this study, we have proposed a method to reduce this distortion for a SMC Ćuk converter operating in CCM. Two different options have been considered. The first one consists of a PI controller applied to the switching function. The second option consists of a time varying hysteresis width which is made enough small as the input voltage approaches zero. With both methods, the proportionality of the input variables is satisfied with a simple design resulting in a very low distortion control of the input current. Numerical simulations and experimental verification confirm the correct operation of the proposed techniques and verify the robustness of the system. In addition an output current loop is used to control the load current.

References

[1] J. M. Alonso, M. A. Dalla Costa, and C. Ordiz, "Integrated Buck-Flyback Converter as a High-Power-Factor Off-Line Power Supply," *IEEE Transactions on Industrial Electronics,* vol. 55, pp. 1090-1100, 2008.

[2] *Limits for Harmonic Current Emissions (Equipment Input Current ≤ 16 A Per Phase),* IEC 61000-3-2, Part 3-2, 3rd ed., 2005.

[3] A. Cid-Pastor, L. Martinez-Salamero, A. El Aroudi, R. Giral, J. Calvente, and R. Leyva, "Synthesis of loss-free resistors based on sliding-mode control and its applications in power processing," *Control Engineering Practice,* vol. 21, pp. 689-699, 2013.

[4] T. Siew-Chong, Y. M. Lai, and C. K. Tse, "General Design Issues of Sliding-Mode Controllers in DC-DC Converters," *IEEE Transactions on Industrial Electronics,* vol. 55, pp. 1160-1174, 2008.

[5] M. Bodetto, A. El Aroudi, A. Cid-Pastor, J. Calvente, and L. Martinez-Salamero, "Sliding Mode Control of a Cuk converter with variable hysteresis width for HBLEDs applications," in *IEEE International Multi-Conference on Systems, Signals and Devices, SSD*, 2014, pp. 1-6.

[6] M. Bodetto, A. El Aroudi, A. Cid-Pastor, and L. Martinez-Salamero, "High performance hysteresis modulation technique for high-order PFC circuits," *IET Electronics Letters,* vol. 50, pp. 113-114, 2014.

[7] M. Bodetto, A. Cid-Pastor, L. Martinez-Salamero, and A. El Aroudi, "Design of an LFR based on a SEPIC converter under sliding mode control for HBLEDs applications," in *IEEE International Symposium on Circuits and Systems, ISCAS*, 2011, pp. 2901-2904.

Energy Management of a Fuel Cell Serial-Parallel Hybrid System

Harrynson Ramírez-Murillo*, Carlos Restrepo, Javier Calvente, Alfonso Romero and Roberto Giral.

***Abstract*—A serial-parallel hybrid (SPH) fuel cell system which include control and protection loops are presented in this article. The hybrid system is formed by a Fuel Cell (FC), an Auxiliary Storage Device (ASD), and the current-controlled dc-dc converters responsible for the management of the energy between FC and ASD in a serial-parallel topology. The main advantages of the selected converter are its voltage step up and step down properties, high efficiency, and low input and output current ripples. This allows it to be positioned in the different FC hybrid system localizations with a suitable design of its control. Moreover, having the same module for all the system converters simplifies the design and construction tasks. The theoretical analyses have been simulated and validated experimentally on a 48 V, 1200 W dc bus.**

I. Introduction

Proton exchange membrane fuel cell (PEMFC) is a device that converts chemical fuels into electric power, with many advantages such as non-polluting emissions, high-current-output ability, high energy-density, low-operating temperatures which allows a fast start-up, high-efficiency and low weight and volume compared with other fuel cell types [1]. However, the relatively short lifespans of fuel cells represent a significant barrier for their commercialization in both stationary and mobile applications [2]. Therefore, a significant part of research about fuel cells focuses on prolonging their operational lives.

The PEMFC stack is a complex system that requires an auxiliary power-conditioning system to ensure safe, reliable, and efficient operation under different operating conditions. The output characteristics of a PEMFC are limited by the mechanical devices that are used to maintain the air-flow within the cathode, mainly the compressor. As a consequence of this limitation, a load transient will cause a high voltage drop after a short time, which is a symptom of the oxygen starvation phenomena. This operational condition is harmful for the FC because it accelerates the catalyst loss and the carbon-support corrosion [3] and for this reason a FC is considered to be slow dynamic response equipment with respect to the transient load requirements [4]. The prevention of this undesired phenomenon requires the limitation of the slew-rate of the FC current. In addition, to ensure a fast response to any load power transient, batteries, ultracapacitors or other auxiliary power sources in conjunction with current-controlled dc-dc converters are needed to support the operation of the fuel cell, which is know as a FC hybrid system. In this paper a serial-parallel hybrid topology is presented whose key element is an innovative non-inverting buck-boost dc-dc switching converter introduced in [5], with the current control proposed in [6] to be a modular converter in the implemented hybrid system. The modular advantages such as voltage step up and step down properties, high efficiency, wide bandwidth, low input as well as output current ripple. Due to all the above mentioned features, this converter can be positioned in different localizations in the fuel cell hybrid system with a suitable design of its control.

This work was supported by the Spanish Ministerio de Ciencia e Inovación under the projects CSD2009-00046, TEC2009-13172 and TEC2012-30952.

H. Ramírez-Murillo, J. Calvente, A. Romero and R. Giral are with the Departament d'Enginyeria Electrònica, Elèctrica i Automàtica, Escola Tècnica Superior d'Enginyeria, Universitat Rovira i Virgili, 43007 Tarragona, Spain.

C. Restrepo is with the Department of Electrical Sustainable Energy, Delft University of Technology, 2628 CD Delft, The Netherlands.

*Corresponding author. Email: harrynson.ramirez@urv.cat. Postal Address: Avda. Països Catalans 26, Campus Sescelades, 43007, Tarragona, Spain. Fax: (+34)977559605. Telephone number: (+34)977297051.

II. Fuel Cell System

The control loops and protection specifications of the FC serial-parallel hybrid topology shown in Fig. 1 are listed in Table I. As mentioned above, this configuration uses the same converter module with input and output current regulations in the different places of Fig. 1. The digital master control sends the current references to the analogue current loops to regulate the different voltage values of the system. The master control goals are: FC slew-rate current limitation, FC and capacitor range voltage protection, output voltage v_o regulation at 48 V, maximum current limitation in each converter, safe startup and shutdown of the system, among others.

Two different converter models were developed to study the FC series hybrid topology. The first one is a static model to make long-time simulations of the system while the second one is a dynamic model to study the short-time transitions.

A high frequency pole in the v_o control loop was implemented with an analog circuit to reduce the computational costs and the time-delays of the digital master control. This pole works as an anti-aliasing low-pass filter because the converter modules are not synchronized switching frequencies.

III. Experimental Results

This experiment conducted verified that the master control regulated in a satisfactory manner the capacitor voltage V_{ASD} and the output voltage v_o in 50 V and 48 V, respectively by applying the load resistance changes from $47.5\,\Omega$ to $4.7\,\Omega$ with a frequency of 100 Hz and a 50% duty cycle shown in Fig. 2. Different ripple values from i_{g1} and i_{g2} in Fig. 2(a) show the different operation points from converters 1 and 2, respectively. This was achieved since Fig. 2(c) shows that an output current change Δi_o of 9.2 A caused a maximum output

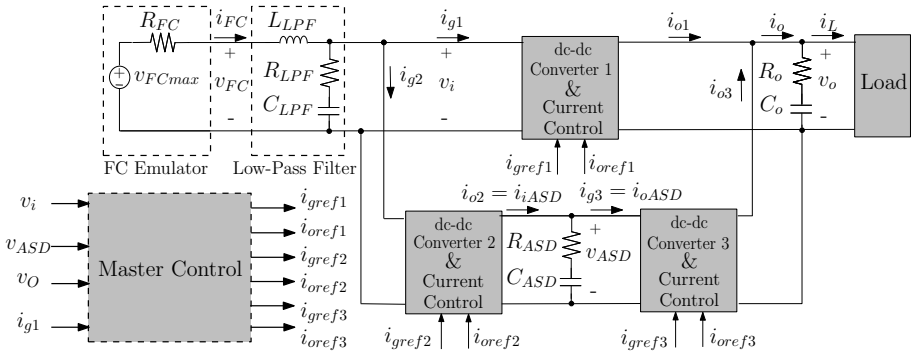

Fig. 1. FC serial-parallel hybrid topology block diagram. The master control regulates the input/output port voltages from each converter by means of the current reference values

TABLE I
FC SERIES HYBRID SYSTEM SPECIFICATIONS.

Parameter	Value	Units	Description
V_{FCmin}	26.0	V	FC minimum voltage
V_{FCmax}	42.0	V	FC maximum voltage
V_{oref}	48.0	V	Output voltage reference
V_{ASDref}	50.0	V	ASD voltage reference
V_{ASDmin}	25.0	V	ASD minimum voltage
V_{ASDmax}	57.0	V	ASD maximum voltage
$-SR_{FCd}$	-32.0	A/s	FC current minimum SR
SR_{FCu}	8.00	A/s	FC current maximum SR
$P_{o\,\max}$	1.20	kW	Output maximum peak power
$P_{FC\,\max}$	500	W	FC peak power
C_o	2.350	mF	Dc bus capacity
C_{ASD}	600	mF	ASD capacity
$I_{\max}$	16.0	A	Converters maximum current
ω_o	2.37	kHz	v_o loop bandwidth
ω_{ASD}	1.33	Hz	v_{ASD} loop bandwidth

voltage transient Δv_o of 1.6 V. In addition, the capacitor voltage exhibited a peak ripple of less than 0.4 V. Also, as Fig. 2(c) shows, the fuel cell maximum current transient of 2.8 A.

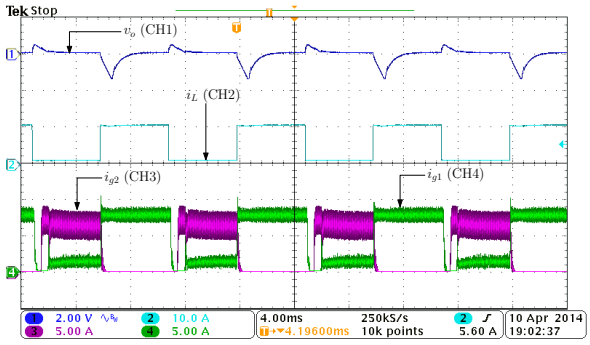

(a)

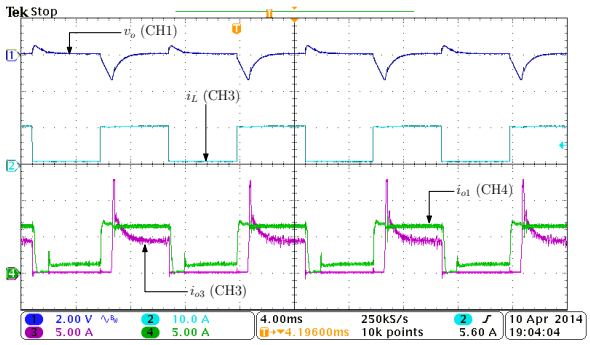

(b)

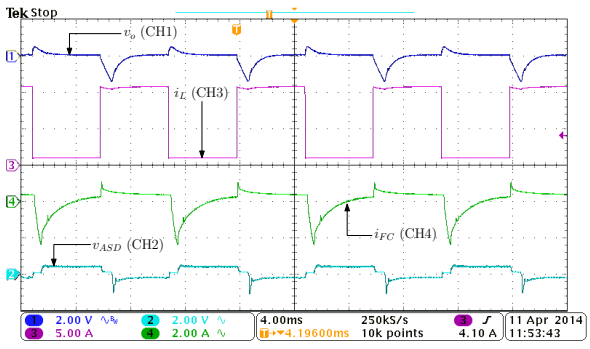

(c)

Fig. 2. SPH topology below a pulsating load power profile, with a frequency of 100 Hz and a 50% duty cycle, $I_{FC} = 7.4$ A, $V_{ASD} = 50$ V and $V_o = 48$ V as mean values. (a), (b) and (c) Experimental measurement. Output voltage v_o (2 V/div, AC coupling), load current i_L (5 or 10 A/div), input currents i_{g1} and i_{g2} (5 A/div), output currents i_{o1} and i_{o3} (5 A/div), fuel cell current i_{FC} (2 A/div, AC coupling), ASD voltage v_{ASD} (2 V/div, AC coupling) and the same time base of 4 ms.

REFERENCES

[1] J. Pukrushpan, A. Stefanopoulou, and H. Peng, "Control of fuel cell breathing," *IEEE Control Syst. Mag.*, vol. 24, no. 2, pp. 30 – 46, apr 2004.

[2] B. Wahdame, D. Candusso, X. Francois, F. Harel, M.-C. Pera, D. Hissel, and J. Kauffmann, "Analysis of a fuel cell durability test based on design of experiment approach," *IEEE Transactions on Energy Conversion*, vol. 23, no. 4, pp. 1093 –1104, dec. 2008.

[3] W. Schmittinger and A. Vahidi, "A review of the main parameters influencing long-term performance and durability of pem fuel cells," *J. of Power Sources*, vol. 180, no. 1, pp. 1 – 14, 2008.

[4] T. C. J. Restrepo, C. Konjedic and R. Giral, "A review of the main power electronics' advances in order to ensure efficient operation and durability of PEMFCs," *Journal for Control, Measurement, Electronics, Computing and Communications, Automatika*, vol. 53, no. 2, pp. 184–198, 2012.

[5] C. Restrepo, J. Calvente, A. Cid-Pastor, A. Aroudi, and R. Giral, "A noninverting buck-boost dc-dc switching converter with high efficiency and wide bandwidth," *IEEE Transactions on Power Electronics*, vol. 26, no. 9, pp. 2490–2503, Sept. 2011.

[6] C. Restrepo, T. Konjedic, J. Calvente, M. Milanovic, and R. Giral, "Fast transitions between current control loops of the coupled-inductor buck-boost dc-dc switching converter," *IEEE Transactions on Power Electronics*, vol. 28, no. 8, pp. 3648–3652, 2013.

Time-coded chipless RFID temperature sensor with self-calibration based on a Vivaldi antenna

Angel Ramos, David Girbau, Antonio Lazaro, and Ramon Villarino

Department of Electronic, Electric and Automatic Control Engineering, Universitat Rovira i Virgili
Av. Paisos Catalans, 26, 43007 Tarragona, Spain – angel.ramos@urv.cat – +34 977 29 70 48

Abstract

This paper proposes a radio frequency identification (RFID) sensor based on an ultra-wide band (UWB) Vivaldi antenna loaded with two transmission lines. The time-domain response is composed by a structural and two tag (or antenna) mode reflections. Each transmission line generates its own tag mode. One tag mode is used to sense temperature, and the other is used to calibrate the sensor. Experimental results obtained with two reader approaches are presented to validate the system.

1. Introduction

Completely-passive battery-free wireless sensors are desirable in remote sensing applications where long-term environment controlling and monitoring take place. Since they do not require neither wiring nor batteries, they can be used in hazardous environments, such as contaminated areas, under concrete, in chemical or vacuum process chambers and also in applications with moving or rotating parts. Chipless RFID tags provide an identification code realized by nonchip-based means, with physical permanent modifications in the tag that modulate the reader's backscattered signal [1]-[3]. Chipless RFID sensor tags are an interesting alternative for passive wireless sensing. They consist of integrating a passive sensor into a chipless tag and adding information of some physical parameter on the backscattered response to an incoming signal. Several approaches to wireless sensors based on chipless RFID tags have recently been published, as for instance [2]-[5].

However, there are also a number of issues that must also be addressed in order to make them competitive in front of other alternative solutions. Some of these aspects are the read range, the reliability, the accuracy or the sensor calibration process. In this direction, this work proposes a self-calibrated time-coded chipless temperature sensor tag.

The backscattered signals in chipless sensor tags only contain information of the physical parameter that is sensed. No other state is available to perform a calibration. This means that the user needs a calibration curve for all possible sensor-reader distances and angles. Two tags could be used for simultaneous measurement, one sensor tag and a calibration tag. This results in a large structure and the problem partly remains, since the tag-reader angle is not always identical for the two tags. This work proposes to integrate a second backscattering signal at the sensor tag in order to perform a self-calibration. In addition, this signal also increases the number of words that can be coded to identify the tag.

The paper is organized as follows. Section 2 describes the temperature sensor design and its basic operation. Section 3 presents some measurements using a Vector Network Analyzer and a UWB radar as readers. Finally, some conclusions are drawn in Section 4.

2. Sensor Design

A. Sensor tag design and measurement setup

The measurement setup is shown in Fig. 1 (top). It consists of a RFID reader that illuminates a sensor tag. The reader can be realized with a Vector Network Analyzer (VNA) sweeping the UWB frequency band (frequency-step technique). The time-domain response is obtained from the inverse Fourier transform of the S_{21} parameter [3]. Another way to realize the reader is using a UWB radar to send a short-time pulse and collecting the backscattered signal with a fast sampler (impulse technique) [3],[6]. The sensor tag proposed in this work is composed by a UWB Vivaldi antenna connected to two transmission lines with different lengths (L_1 and L_2), as shown in Fig. 1 (bottom). One line is terminated with an open circuit (*Line 1*) and the other is loaded with a resistive temperature sensor (*Line 2*) that modulates its reflection coefficient as a function of the temperature. The reader sends a pulse *p(t)*, and receives the signal backscattered at the tag. The received time-domain signal is mainly composed by three reflected pulses: a structural mode (which depends on the tag size, shape and material) and two tag modes (which depend on the load connected at the two transmission lines). The *Tag1* mode is used to normalize the *Tag2* mode, instead of normalizing *Tag2* with the structural

mode, as done in [3]. It is important to note that the angular behaviour of the structural mode and the tag or antenna mode are different. The structural mode depends on the radar cross section (RCS) associated to the shape and materials of the tag. The tag mode is associated to the reradiated fields on the antenna (it follows the radiation pattern of the antenna) [3]. In consequence, the structural-to-tag mode ratio depends on the illumination angle, whereas the *Tag1*-to-*Tag2* modes ratio is independent of the angle because the two amplitudes depend on the same radiation pattern.

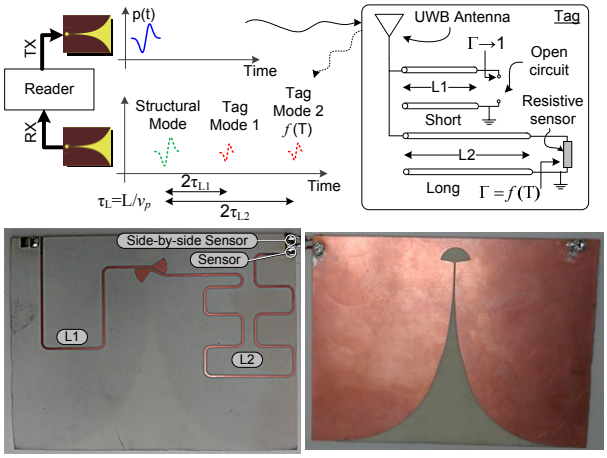

Fig. 1. System (reader + tag) setup with scheme of the signals transmitted and received at the reader (top), tag photograph of front face (bottom left) and back face (bottom right). The tag is manufactured on Rogers 4003 substrate. Tag size: 11.5 cm x 8.7 cm.

B. Tag characterization

Fig. 2 shows the measured tag response as a function of several loads connected at the ends of lines L_1 and L_2. The first peak corresponds to the structural mode. The second and third peaks correspond to the tag modes for the (short-delay) line L_1 (*Tag1*) and for the (long-delay) line L_2 (*Tag2*), respectively. The fourth and next peaks are multiple reflections of the tag modes. When the lines are terminated with an open circuit (OC), their associated tag modes have the largest amplitude. On the other hand, when the loads are matched to the characteristic impedance of the lines (80 Ω) their amplitudes are very small. A background subtraction technique has been applied in order to remove clutter and coupling between the reader's transmitting and receiving antennas. The Continuous Wavelet Transform has been applied to improve the signal to noise ratio [3].

Fig. 3 shows the measured tag response when the load connected to line L_2 is changed from 82 to 180 Ω. It can be observed that while the structural and Tag1 modes remain invariant, the *Tag2* mode changes its amplitude.

Fig. 4 shows the measured ratio between the structural mode and the *Tag2* mode and between *Tag1* and *Tag2* modes as a function of the load connected at the end of line L_2. It can be observed that both ratios depend on the load.

Fig. 5 shows the structural mode (top left) and *Tag1* and *Tag2* modes (top right) as a function of the tag-reader azimuth angle, being the *Tag2* mode loaded with 180 Ω. The structural mode can be seen as the RCS of the tag, and the tag modes as the tag radiation pattern over the entire frequency band. Taking into consideration the angles where the antenna radiates (-30º to 30º), the structural-to-*Tag2* and the *Tag1*-to-*Tag2* ratios are shown (Fig. 5, bottom). It can be deduced that using the ratio between tag modes is more constant than using the structural mode. Both ratios have been empirically demonstrated to be fairly constant with distance [6].

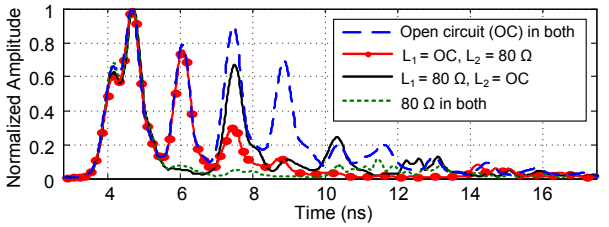

Fig. 2. Structural modes (first peak), tag modes of the short-delay line L_1 (second peak, *Tag1*) and tag modes of the long-delay line L_2 (third peak, *Tag2*) depending on the loads connected at their ends.

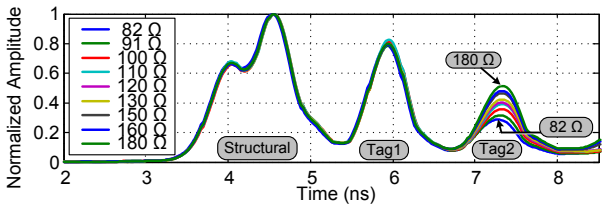

Fig. 3. Tag response as a function of the load at the end of line L_2.

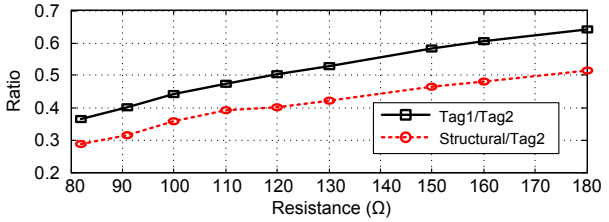

Fig. 4. Ratio between *Tag1* and *Tag2* modes and between the structural mode and *Tag2* mode as a function of the load, measured at a 40 cm tag-to-reader distance.

3. Sensor Measurement

A Vishay PTS 100 Ω temperature sensor is connected at the end of line L_2. A second identical sensor is placed side-by-side in order to measure the resistance with a multimeter for calibration (see Fig. 1). The reflection coefficient at the end of line L_2 changes with the temperature, and so does the amplitude of *Tag2* mode. In this section it is shown the advantage of obtaining the temperature from the ratio between *Tag1* and *Tag2* modes in front of the ratio between the structural and *Tag2* modes.

Fig. 6 shows the measured response when the sensor temperature is changed from 36 ºC to 130 ºC. This measurement has been done using the step-frequency technique (VNA). Fig. 7 shows the estimated temperature from the tag mode as a function of the real temperature for the structural-to-*Tag2* ratio and the *Tag1*-to-*Tag2* ratio. The temperature is obtained from the resistance measurement with the side-by-side sensor. The processing techniques described in [3] have been performed. It can be observed that using the *Tag1*-to-*Tag2* ratio clearly reduces the measurement error.

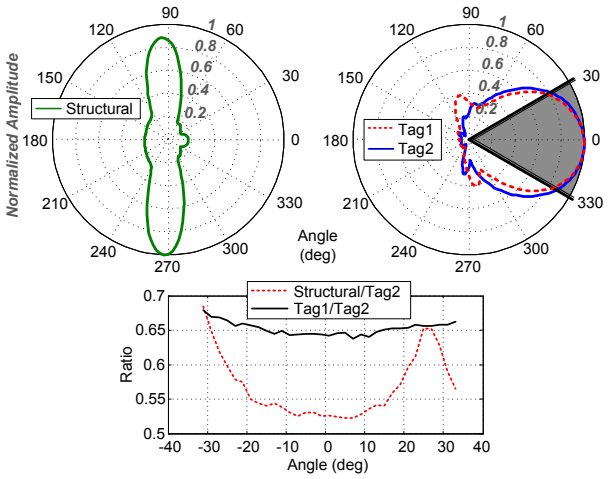

Fig. 5. Structural mode (top left) and tag modes (top right) as a function of the tag-reader azimuth angle. Ratio between the structural and *Tag2* mode and between *Tag1* and *Tag2* modes (bottom) for the gray-shaded area.

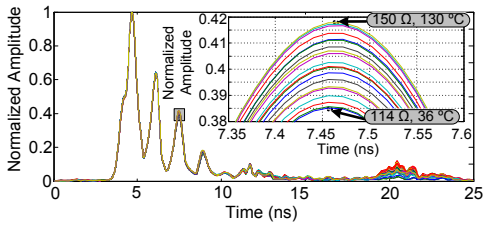

Fig. 6. Measured tag response as a function of the temperature with the step-frequency technique at 40 cm. In the inset, zoomed response of the *Tag2* mode.

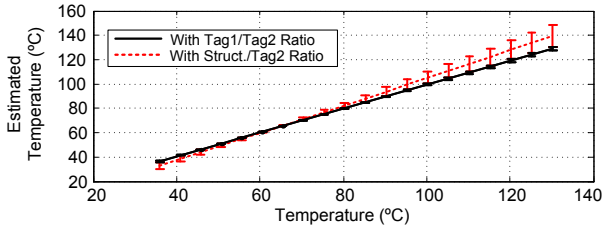

Fig. 7. Estimated temperature as a function of the temperature using the ratio between *Tag1* and *Tag2* modes (solid black line) and using the ratio between the structural and *Tag2* modes (dashed red line) measured with the step-frequency technique at 40 cm.

Finally, Fig. 8 shows the same measurement done with the impulse technique using a low-cost commercial CMOS radar [6]. An identical behaviour is observed, although the measurement error is larger due to the higher noise of its receiver in front of using a VNA.

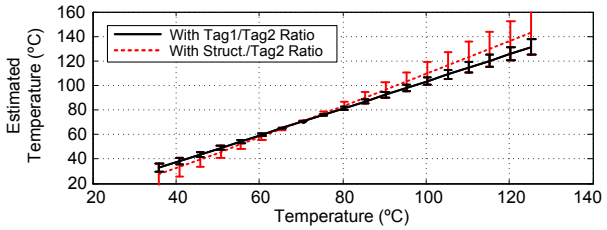

Fig. 8. Estimated temperature as a function of the temperature using the ratio between *Tag1* and *Tag2* modes (solid black line) and using the ratio between the structural and *Tag2* modes (dashed red line) measured with the impulse technique at 40 cm.

4. Conclusion

A radio frequency identification sensor system consisting of a passive chipless sensor tag and a UWB reader has been presented. The tag is based on a UWB Vivaldi antenna loaded with two delay lines. One line is terminated with an open circuit and the other loaded with a resistive sensor that changes the load reflection coefficient as a function of the temperature. The ratio between the two tag modes associated to the two delay lines is used for calibration. It permits to independize the sensor from the illumination angle within the beamwidth of the tag antenna. Experimental results with a VNA and a UWB radar have been presented.

References

[1] S. Preradovic, I. Balbin, N. C. Karmakar, and G. F. Swiegers, "Multiresonator-based chipless RFID system for low-cost item tracking," *IEEE Transactions on Microwave Theory and Techniques*, vol. 57, no. 5, pp. 1411-1419, May 2009.

[2] A. Vena, E. Perret, S. Tedjini, et al., "A compact chipless RFID tag with environment sensing capability," *IEEE MTT-S International Microwave Symposium Digest*, pp. 1-3, June 2012.

[3] D. Girbau, A. Ramos, A. Lázaro, S. Rima, and R. Villarino, "Passive wireless temperature sensor based on time-coded UWB chipless RFID tags", *IEEE Trans. on Microwave Theory and Techniques*, vol. 60, no. 11, pp. 3623-3632. November 2012.

[4] E. M. Amin and N. C. Karmakar, "Development of a low cost printable humidity sensor for chipless RFID technology," *IEEE International Conference on RFID Technology and Applications (RFID-TA)*, November 2012.

[5] B. Kubina, C. Mandel, M. Schüßler, M. Sazegar, and R. Jakoby, "A Wireless Chipless Temperature Sensor utilizing an Orthogonal Polarized Backscatter Scheme," *Proceedings of the 42nd European Microwave Conference*, October 2012.

[6] A. Ramos, D. Girbau, A. Lázaro, and S. Rima, "IR-UWB radar setup and tag design for time-coded chipless RFID," *6th Europ. Conf. on Antennas and Prop.*, pp. 2491-2494, March 2012.

3D CELL CULTURE MICROENVIROMENTS FOR TISSUE ENGINEERING

M. ALBA[1], P. FORMENTÍN[1], U. CATALÁN[2], S. FERNÁNDEZ-CASTILLEJO[2], R. SOLÀ[2], J. PALLARÈS[1], L. F. MARSAL[1]

[1] *Nano-electronic and Photonic Systems, Departament d'Enginyeria Electrònica, Elèctrica I Autómatica, Universitat Rovira i Virgili, Països Catalans 26, 43007, Tarragona, Spain; E-mail: lluis.marsal@urv.cat;*

[2]*Unit of Lipids and Atherosclerosis Research, Facultat de Medicina I Ciències de la Salut, Universitat Rovira i Virgili, Sant Llorenç 21, 43201 Reus, Tarragona, Spain.*

Abstract

Human Aortic Endothelial Cells (HAEC) plays a key role in the pathogenesis of atherosclerosis, which is a common, progressive and multifactorial disease that is the clinical endpoint of an inflammatory process and endothelial dysfunction. Study and development of new therapies against cardiovascular disease must be tested *in vitro* cell models, prior to be evaluated *in vivo*. To this aim, new cell culture platforms are developed that allow cells to grow and respond to their environment in a more realistic manner. In this work, the cell adhesion and morphology of HAEC are investigated on functionalized porous silicon (PSi) substrates with two different pore size configurations: macroporous and nanoporous silicon. Results show that different pore geometries induced different cellular response in the cell morphology and adhesion.

1. Introduction

The properties of porous silicon (PSi) make it an interesting material for biological application. PSi is biodegradable and it dissolves into non-toxic silicic acid. The dissolution rate depends on the pore geometry tuned and surface modification and it grows as the pore size increases. The pore diameter can be controlled and, a variety of pore sizes can be produced and the high surface are can be loaded with a range of bioactive species. For all this, PSi has been proposed and used for *in vitro* and *in vivo* biological applications.[1-2] Substrate topography affects cell functions, such as adhesion, proliferation, migration and differentiation.[3] Here, we reported the cell adhesion and cell morphology of Human Aortic Endothelial Cells (HAEC) on macro- and nanoporous silicon functionalized substrates. The interactions between cells and Si substrates have been characterized by environmental scanning electron microscopy (ESEM) and the results show the effect of the surface topography on the HAEC behaviour compared to the flat silicon. This study demonstrates potential applications of these forms of silicon for controlling cell development in tissues engineering as well as in basic cell biology research.

2. Experimental

Boron-doped p<100> silicon wafers with a resistivity of 0.001-0.002 ohm-cm were used for etching Nanoporous Silicon (NanPSi). Silicon wafers with a resistivity of 10-20 ohm-cm were used for Macroporous Silicon (MacPSi). All PSi were prepared using an anodization process in a custom-made teflon etching cell. An electrolyte formed by combining hydrofluoric acid (HF 48%) with ethanol and glycerol with the ratio of 3:7:1 (v:v) respectively, was used for the anodization of NanPSi and an electrolyte of hydrofluoric acid (40%) in N,N dimethylformamide (DMF) (1:10) was made for MacPSi etching. For NanPSi, the wafer was etched with a current density of 60mA/cm^2 for 1 min. MacPSi was etched with a current density of 4 mA/cm^2 for 30 min. Then the samples were rinsed with pentane and dried under a stream of nitrogen. Macro- and nanoporous silicon samples were morphologically characterized by scanning electron microscopy.

Porous silicon surfaces were functionalized with (3-aminopropyl)trietoxysilane (APTES) after an oxidation at 600 °C for 15 min. Then, samples were treated at 121 °C during 15 min for sterilization, and they were individually placed into single wells of a 12-well plate. The HAEC were seeded in complete cell culture medium and were growth at 37 °C in a humidified incubator with atmosphere containing 5% CO_2 for 48h. Silicon substrates were washed to remove adhering and death cells and then, the remaining cells were fixed. The morphology of cells adhering to the functionalized PSi substrates were observed with scanning electron microscopy at voltages ranking from 5-10kV.

3. Results and Discussion

The porous silicon (pSi) samples were produced by electrochemical etching of p-type silicon wafers in HF-based electrolytes. Two types of samples were generated by varying the etching conditions in order to study the cellular response on surfaces with different pore geometry. The topography of theses substrates was analyzed using scanning electron microscopy (Figure 1).

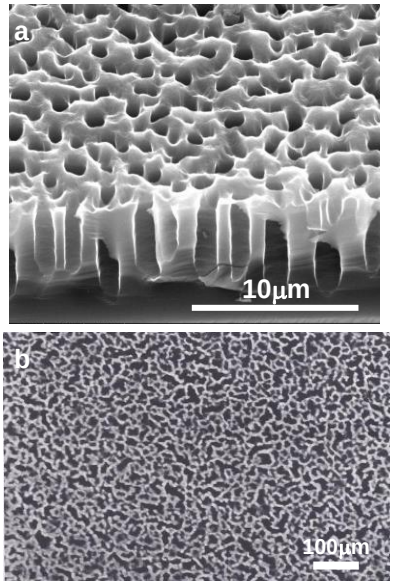

Fig.1. Top view ESEM images of: a) macroporous silicon substrate with a pore diameter of 1-1.5 μm and b) nanoporous silicon with pore sizes less than 50 nm.

Figure 2 shows representative images of HAEC growing on macro- and nanoporous Si substrate and, on flat Si as control, after 48 h of incubation. On nanoporous silicon, cells appeared elongated and spread with protrusions and, the development of the filopodia is visible at the cell borders (figure 2b), which it is due to the nanopores may not anchor firmly to the surface. The same shape is observed on flat silicon (figure 2a).

The cell migration after 48 h incubation on pSi 1-1.5 μm results in 2-D and 3-D shape of the HAEC, while the cells on nano- and flat silicon show only 2-D migration movements. In the macroporous substrate, the cell appears with a well spread cytoskeleton with formation of protusions out of the cell membrane and, is visible how part of it penetrates inside the macropore (figure 2c-d). Filopodia is not present in this type of substrate.

Cytotoxicity was determined by a colorimetric assay, which measures released LDH activity. LDH enzyme is released into the cell culture when the membrane is damaged. So, an increase of LDH has associated with a cellular injury. After a period 48 h, the production of LDH activity released increases in the porous silicon substrates and also in the blank control (cells incubated without silicon substrates). These results indicate that the presence of the silicon in the culture medium do not cause cytotoxicity *per se*.

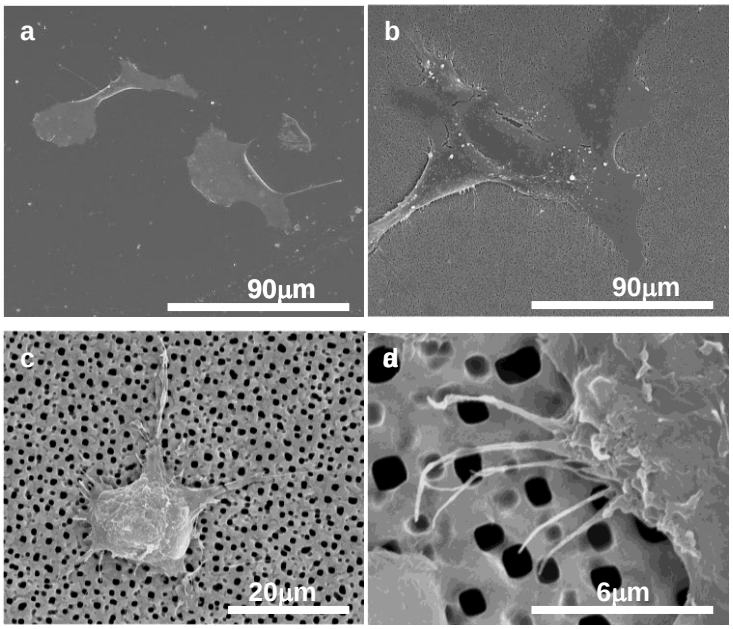

Fig.2. SEM images of HAEC culture after 48h incubation on modified silicon substrates: a) flat silicon, b) nanoporous silicon and c-d) macroporous silicon.

4. Conclusions

The cell adhesion and morphology of HAEC on two different silicon substrates with pore size in the macro and nanoporous range were investigated. Results show that different pore geometries induced different cellular response in terms of adhesion and morphology. MacPSi and NanPSi are promising substrates for developing new 3D cell culture platforms with applications in tissues engineering as well as in basic cell biology research.

5. Acknowledgments

This work was supported by Spanish Ministerio de Economía y Competividad (MINECO) under grant number TEC2012-34397 and Generalitat de Catalunya under grant number 2014-SGR-1344.

References

[1] S. P. Low, K. A. Williams, l. T. Canham, and N. H. Voelcker, *Biomaterials*, 4538 (2006). S. P. low, N. H. Voelcker, L. T. Canham, and K. A. Williams, *Biomaterials*, 2873 (2009).

[2] F. Gentile, R. La Rocca, G. Marinaro, A. Nicastri, A. Toma, F. Paonesa, G. Cojoc, C. Liberale, F. Benfenati, E. Di Fabricio and P. Decuzzi, *ACS Appl. Mater. Interfaces*, 2903 (2012). M. J. Sweetman, M. Ronci, S. R. Ghaemi, J. E. Craig, and N. H. Voelcker, *Adv. Funct. Mater.* 1152 (2012).

[3] A. Curtis and C. Wilkinson, *Biomaterials*, 1573 (1997). W. Sun, J. E. Puzas, T.-J. Sheu, X. Liu, and P. M. Fauchet, *Adv. Mater.* 921 (2007).

Aging of PTB7:$PC_{70}BM$ Blend Solution to Fabricate Standard Solar Cell and Its Influence on Electrical Performance

V.S. Balderrama, J.G. Sánchez, P. Granero, J. Pallarés, J. Ferré-Borrull, and L.F. Marsal*

Departament d'Enginyeria Electrònica, Elèctrica i Automàtica, Universitat Rovira i Virgili, Avda. Països Catalans 26, 43007 Tarragona, Spain
*Corresponding author: e-mail: lluis.marsal@urv.cat, Phone. +34 977 559 625, Fax: +34 977 559 605

Abstract

In this work, we study the effects on the power conversion efficiency (*PCE*) of the Poly({4,8-bis[(2-ethylhexyl)oxy] benzo[1,2-b:4,5-b′] dithiophene-2,6-diyl}{3-fluoro-2-[(2-ethylhexyl) carbonyl] thieno [3,4-] thiophenediyl}) (PTB7):[6, 6]-Phenyl C_{71} butyric acid methyl ester ($PC_{70}BM$) bulk-heterojunction organic solar cells (BHJ-OSC), where two blend solutions are prepared and allowed to stand during two different times: 48 h for the first solution and 6072 h for the second one, under N_2 environment. Devices fabricated with the blend solution of 48 h the *PCE* were higher than those for samples fabricated with the blend solution of 6072 h. The degradation on the efficiency of the solar cells after 120 h under nitrogen environment is mainly due to a reduction of short circuit current density (J_{SC}) and fill factor (*FF*) while open circuit voltage (V_{OC}) is the most stable parameter in both types of solar cells studied.

1. Introduction

Recently, the polymer of low-bandgap (i.e. PTB7) has been reported to enhance the *PCE* in BHJ solar cells of 7.1% [1, 2]. Actually, the stability of the polymeric solar cells is one of the critical issues to be resolved. However, studies about of the stability on solar cells manufactured with PTB7:$PC_{70}BM$ materials have not been reported yet. In this work, we manufacture standard OSC with two different blend solutions prepared at different times. Electrical measurements under dark and illumination condition are used to analyze the *PCE* of the devices just after fabrication and at 120 h of degradation under nitrogen environment.

2. Experimental Results

Photovoltaic devices were fabricated on pre-cleaned, patterned ITO glass substrates. 40 nm of PEDOT:PSS was deposited on the substrates by spin coating at 4500 rpm by 45 s and annealed at 120 ºC during 20 min. The PTB7:$PC_{70}BM$ active blend with a weight ratio of 1:1.5 was dissolved in chlorobenzene (CB) to get the solution of 25 mg/ml and was left stirring overnight. Two blend solutions were prepared under the same conditions. The first and second blend solutions (named as BS-1 and BS-2) were allowed to stand during 48 h and 6072 h under nitrogen environment in dark and at 24 ^{o}C, respectively. The blend solutions were deposited on top of the PEDOT:PSS layer by spin coating at 800 rpm during 30 s, obtaining 100 nm of thickness. Afterwards, the cathode layer, consisting 25 nm of Ca and 100 nm of Ag, being deposited by thermal evaporation in an ultra-high vacuum chamber (9 x 10^{-7} mbar), at a rate of 0.04 *k*Å/s and 0.05-0.08 *k*Å/s respectively, on top of the active layer. The active area of the devices was 0.09 cm^2 as defined by the geometric overlap between ITO and Ag. No further annealing was done on the solar cells after the evaporation of metallic contacts.

The architecture of device is shown in Fig. 1. The current density–voltage (*J–V*) characteristics of the devices were measured with a Keithley 2400 source measurement unit in combination with a solar simulator (Abet Technologies model 11000 class type A). The appropriate filters were utilized to faithfully simulate the AM 1.5G spectrum.

Fig. 2 is shown the *J–V* curves under light of the devices manufactured with the blend solutions BS-1 and BS-2. The performance parameters of the OSC were listed in Table 1. Devices made with the blend BS-1 just after fabrication the *PCE*, open circuit voltage (V_{OC}), short circuit current (J_{SC}) and fill factor (*FF*) were of 5.91%, 710 mV, 13.60 mA/cm^2 and 61%, respectively. While that samples manufactured with the blend solution BS-2 presented a little lower their parameter such as PCE, *Jsc* and *Voc* being of 11%, 4% and 7% less regarding blend solution BS-1 just after fabrication, respectively. Afterward, the two groups of solar cells got with the two different blend solutions were storage in dark and under nitrogen environment at 24 ^{o}C by 120 h following the procedure reported in [3]. The performance parameters for devices manufactured with BS-1 such as

PCE, V_{OC}, J_{SC}, and *FF* decreased moderately in 120 h being of 9.0%, 3.0%, 4.7% and 1.6%, respectively. While that for devices fabricated with BS-2 such as *PCE*, V_{OC}, J_{SC}, and *FF* were slightly faster the degradation being of 26.0%, 3.0%, 15.7% and 9.8%, respectively. Fig. 3 shows *J–V* curves under dark for the group of devices manufactured with blend solutions BS-1 and BS-2 just after fabrication and after of the exposure under nitrogen environment by 120 h. The series and shunt resistances per unit area (R_{S0} and R_{SH0}) were calculated as is reported in [3]. The fresh devices fabricated with BS-2 solution had higher R_{SH0} than that samples fabricated with BS-1 solution. The increase of R_{SH0} could be due to that there are less recombination of charge carriers near the dissociation site (e.g. Donor/Acceptor interface of both organic materials PTB7:PC_{70}BM in this case), that is, it also depends on the transport properties of the semiconductor [4]. However, more studies of analysis are required to understand the changes in performance parameters of the cells when the blend solution has long time for the preparation.

3. Conclusions

We have investigated the performance parameters and degradation of ITO / PEDOT:PSS / PTB7:PC_{70}BM / Ca /Ag solar cells under nitrogen environment. Two blend solutions were prepared and allowed to stand by 48 h and 6072 h. Samples made with the blend solution BS-1 with less downtime had higher the performance parameters. The *PCE* in devices manufactured with BS-1 was a 12% higher than that the devices fabricated with the blend solution BS-2.

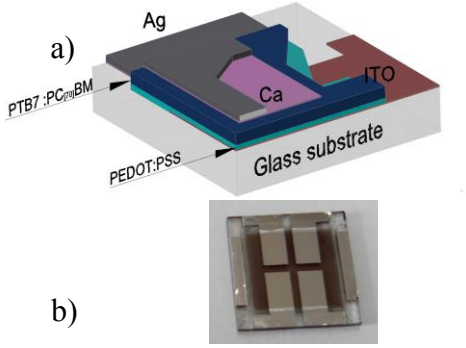

Fig.1. a) The image shows the standard structure PTB7:PC_{70}BM bulk heterojunction organic solar cell; b) physical representation of device.

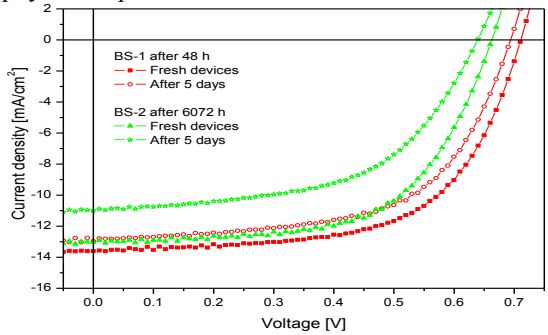

Fig.2. *J–V* curves under illumination of the organic solar cells fabricated with fresh and old PTB7:PC_{70}BM blend solutions.

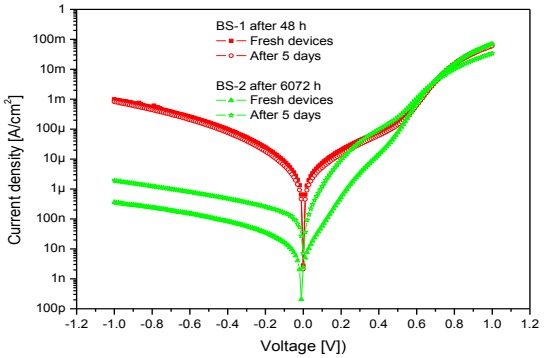

Fig.3. *J–V* curves under darkness of the organic solar cells fabricated with fresh and old PTB7:PC_{70}BM blend solutions.

Blend solution	Measurement of the PTB7:PC_{70}BM OSC	*Voc* [mV]	*Jsc* [mA/cm²]	*FF* [%]	*PCE* [%]	R_{S0} [Ω-cm²]	R_{SH0} [kΩ-cm²]
BS-1 [48 h]	Fresh	710	13.60	61	5.91	3.84	14.60
BS-1 [48 h]	After 5 days	690	12.96	60	5.38	4.40	20.83
BS-2 [6072 h]	Fresh	660	13.04	61	5.23	3.58	3082.10
BS-2 [6072 h]	After 5 days	640	11.00	55	3.85	8.50	244.54

Table1. Performance parameters of the OSC fabricated with blend solution under different conditions.

Acknowledgements

This work was supported by the Spanish Ministry of Economy and competitiveness (MINECO) under grant number, TEC2012-34397 and by Catalan authority under project AGAUR 2014 SGR 1344.

References

[1]H. Zhou Granero, "High-efficiency polymer solar cells enhanced by solvent treatment", *Adv. Funct. Mater. 25*, pp. 1646, 2013.

[2]L. Lu, "Understanding low bandgap polymer PTB7 and optimizing polymer solar cells based on it", *Adv. Mater.* doi: 10.1002/adma.20140038425, 2014.

[3]V.S. Balderrama, "Degradation of electrical properties of PTB1:PCBM solar cells under different environments", *Sol. Energy Mater. Sol. Cells* 125, pp. 155, 2014.

[4]V.S. Balderrama, "Influence of P3HT:PCBM blend preparation on the active layer morphology and cell degradation", Microelectron. Reliab. 51, pp. 597, 2011.

Gas sensing properties of nanostructured ZnO films obtained by atomic layer deposition on porous anodic alumina templates

R. Calavia[a], S. Roso[b], RM. Vázquez[a], S. Imre[b], E. Llobet[a]

[a]Minos-Emas. University Rovira i Virgili. Avd. Països Catalans, 26, 43007, Tarragona, Spain
[b]Department of Inorganic and Analytical Chesmistry, Budapest University of Technology and Economics. Hungary

Abstract

In this work we show the fabrication, morphological characterization and gas sensing properties of a nanostructured ZnO film grown on porous alumina (PAA) via ALD in order to conformally cover its pores, reaching in this way a highly nanostructured oxide film.

1. Introduction

The sensitivity of metal oxide layers as active materials for gas sensing applications increases when the surface to volume ratio rises. The gas sensing properties of nanostructured metal oxide films, sputter-deposited on porous anodic alumina (PAA) templates have been studied by our group [1,2]. For such films to continuously cover the pores of PAA, a step of pore widening is unavoidable, which significantly reduces the length to width aspect ratio of pores and, therefore, surface area. Here we have employed atomic layer deposition (ALD) to conformably coat PAA templates with thin films of zinc oxide (thickness up to 10 nm). ALD allows for avoiding the pore widening step needed with sputtering and these results in nanostructured metal oxides with increased surface area. As the films deposited by ALD have a very high surface to volume ratio, they are good candidates for gas sensor applications.

2. Sample preparation

A *p*-type silicon wafer was used as substrate (Fig.1.a). On the wafer a dry silicon oxide was grown (Fig.1.b). On the SiO2 layer a 600/20 nm thick Al/Ti bilayer was sputter-deposited (Fig.1.c) and anodised. For the anodising process a 0.4 M tartaric acid aqueous solution was used as electrolyte and a density current of 4.5 mA/cm^2 was set to obtain the PAA film on the silicon wafer (Fig.1.d). On the PAA were deposited 4 platinum electrodes with 50 µm and 80 µm gap (right) by lithography (Fig.1.e). Finally, a 10 nm thick ZnO film was grown by ALD (Fig.1.f) at 100 ºC using a shadow mask in order to protect the electrode contacts.

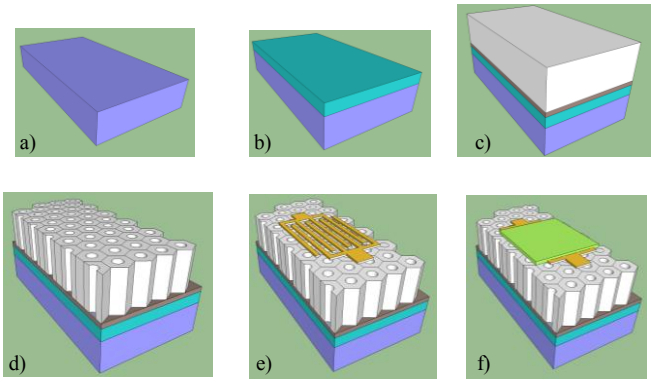

Fig.1. Sensor fabrication steps. a) p-type Si substrate. b) Dry SiO_2. c) Al/Ti sputter-deposited. d) Anodising aluminium layer to obtain porous alumina layer. e) Platinum electrodes deposition. f) 10 nm thick ZnO deposition by ALD.

3. Morphological analysis

The PAA layer obtained on the silicon substrate was analysed by SEM. Images on top show the upper surface (Fig.2.a) and a FIB cross sectional cut (Fig.2.b). The pore diameter and interpore distance were studied using these images, where the results were 50 nm and 180 nm, respectively. After the ZnO deposition a FIB cross sectional cut was made and imaged (Fig.2.c) Prior to cut the sample, a thick Pt stack was deposited by FIB. In this image there is a light and thin line that covers conformally the PAA layer, which is the ZnO film deposited by ALD. Its thickness is close to 10 nm. Under the PAA remains pure aluminium and the silicon oxide at the bottom of the image.

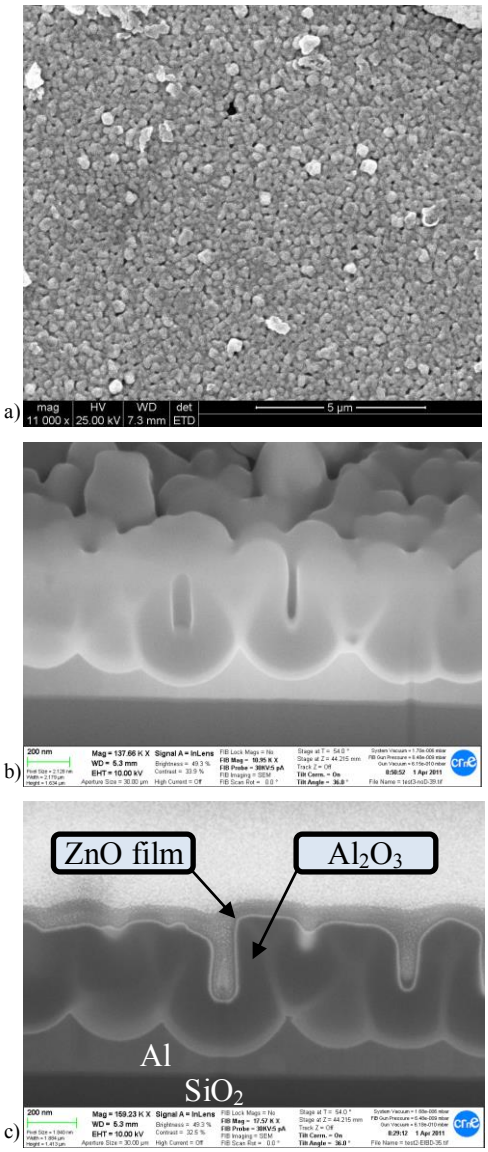

Fig.2. Morphological characterization. a) Porous alumina surface SEM image before ALD deposition. b) FIB cross sectional cut porous alumina layer. c) FIB cross sectional cut porous alumina layer after ALD deposition.

4. Gas sensing properties

A heater was glued on the bottom of the sensor and the working temperature was fixed at 250 ºC. The electrodes gap selected was 80 µm. The behaviour as gas sensor was evaluated for ethanol at different concentrations (100 ppm, 200 ppm (Fig.3.) and 500 ppm in dry air). The response obtained for these concentrations, calculated as Rair/Rgas, was 1.32, 1.63 and 1.66 respectively. Sensor response is reproducible. Response time to ethanol is about 120 s.

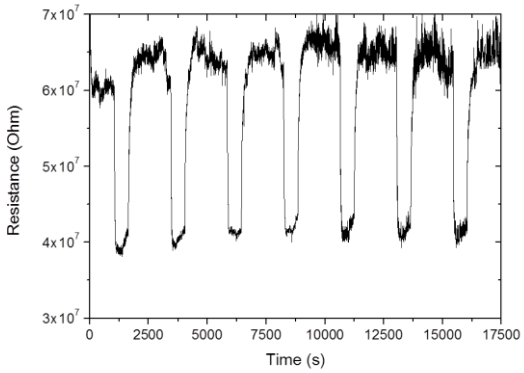

Fig.3. Response to 200 ppm Ethanol at 250 ºC

5. Conclusions

The ZnO film obtained by ALD conformally covers the PAA layer obtained by anodising on a silicon substrate. The ALD process is compatible with the standard lithography process employed for the patterning of Pt electrodes. This ZnO film has shown stable sensing properties for ethanol at different concentrations when operated at 250 ºC. In the future other materials and the response for other gases will be studied.

References (Times 10 bold)

[1] Int. Jour. Hydrogen energy, 38, 8011, 8021
[2] A. Chemistry, 84-17, 7502, 7510

Synthesis of colloidal Bi_2S_3 nanocrystals with tunable size from nanodot to nanorod

P.L. Han, P. Formentin, J. Pallarés and L.F. Marsal*

Departament d'Enginyeria Electrònica, Elèctrica i Automàtica, Universitat Rovira i Virgili, Av. Paisos Catalans 26, Tarragona, Spain
Phone: (+34) 977 55 96 25 *E-mail address: lluis.marsal@urv.cat

Abstract

Colloidal Bi_2S_3 nanocrystals with different shapes have been prepared *via* a simple hot injection method. The X-ray powder diffraction (XRD) patterns show that the resulting Bi_2S_3 nanocrystals belong to the orthorhombic phase. Transmission electron microscopic (TEM) studies reveal that the as-prepared Bi_2S_3 can be tuned to different morphologies by varying the experimental temperature.

1. Introduction

Bi_2S_3 is a novel semiconductor material with a direct bandgap of 1.3 eV [1]. It has attracted much attention because of its potential applications such as photocatalysis, photovoltaic conversion and biomolecule detection [2-4]. In recent years, one dimensional Bi_2S_3 structures with various morphologies including nanoflowers, nanorods, nanodots and nanowires have been synthesized by hydrothermal synthesis, microwave-assisted synthesis, solvothermal method, etc [5-6]. In addition, hot injection technique based on organic solvent route is also applied for fabrication of monodisperse nanoparticles with tunable size and shape [7]. Herein, Bi_2S_3 nanomaterial with a variety of morphologies has been prepared *via* the simple, effective hot injection method. We also discuss the effect of injection temperature during the fabrication process on the material shape.

2. Experimental section

Bi_2S_3 crystals were synthesized introducing a modification in the hot injection procedure [8]. Typically, the mixture solution containing 0.9 g of bismuth neodecanoate (bismuth precursor), 5 ml of oleic acid and 7.5 ml of octadecene was pumped for 2 h at 90 ℃. After this, the solution was heated to 155 ℃ and kept at this temperature for 20 min. Then 1.5 ml of oleylamine containing 0.094 g of thioacetamide (sulfur precursor) was quickly injected into the vessel under vigorous stirring at different conditions. In the first case, the sulfur precursor was injected at 155 ℃. In the second case, the sulfur precursor was injected when the solution lowed to 105 ℃. All reactions were allowed to proceed for 2 min in each case. After cooling to room temperature, oleate capped Bi_2S_3 nanocrystals were obtained after centrifugation and washed by successive dispersion/precipitation in toluene/ethonal. Finally the nanocrystals were dispersed in anhydrous toluene.

3. Results and discussion

Full XRD patterns from Bi_2S_3 samples obtained at two different injection temperatures are showed in Figure 1. All the different peaks can be indexed as the orthorhombic structure (JCPDS No 01-089-8964) and the major peaks can be ascribed to 010, 211, 221, 112 planes. The purity is confirmed by the trace of impurities. With increasing the injection temperature from 105 ℃ to 155 ℃, XRD patterns became sharper, which indicates increased crystallinity and grain growth as well. In order to investigate the morphology of the pure bismuth sulfide nanoparticles obtained at two different injection temperatures, TEM images are shown in Figure 2. The presence of ligands on the particle surface, leads to uniform size and excellent monodispersity for both nanodots and nanorods. For the sample fabricated at 105 ℃ injection temperature, TEM image displays uniform nanodots with 3-4 nm (Figure 2a). When the injection temperature was 155 ℃, the nanorods are also observed remarkably uniform in size and shape, with diameter of 5-6 nm and length of 25-30 nm (Figure 2b). In the synthesis of nanomaterials *via* wet chemical routes, reaction temperature is often a decisive factor for nucleation and growth processes. In our system, the injection temperature in the synthesis of Bi_2S_3 nanocrystals may effectively affect the speed of growth and nucleation. By comparative analysis of XRD, the Bi_2S_3 nanorods show a better crystallinity. Therefore, the increase in particle size is followed by a crystallinity enhancement.

4. Conclusion

Orthorhombic Bi_2S_3 nanocrystals have been prepared by a hot injection approach. The crystallinity and micromorphology of Bi_2S_3 can easily be tuned by changing the injection temperature. When the injection temperature increases from 105 ℃ to 155 ℃, the diameter and length increase in particle size is followed by a crystallinity enhancement.

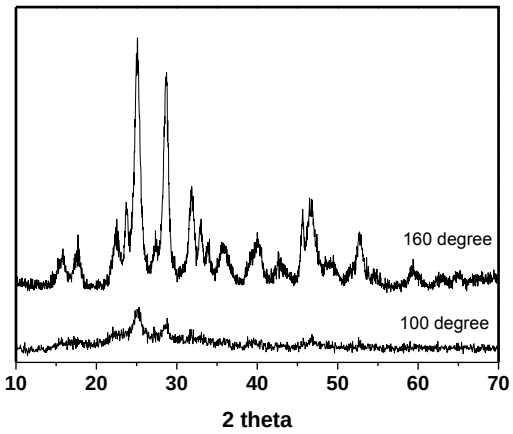

Fig.1. XRD patterns of Bi_2S_3 nanocrystals prepared at two different injection temperatures.

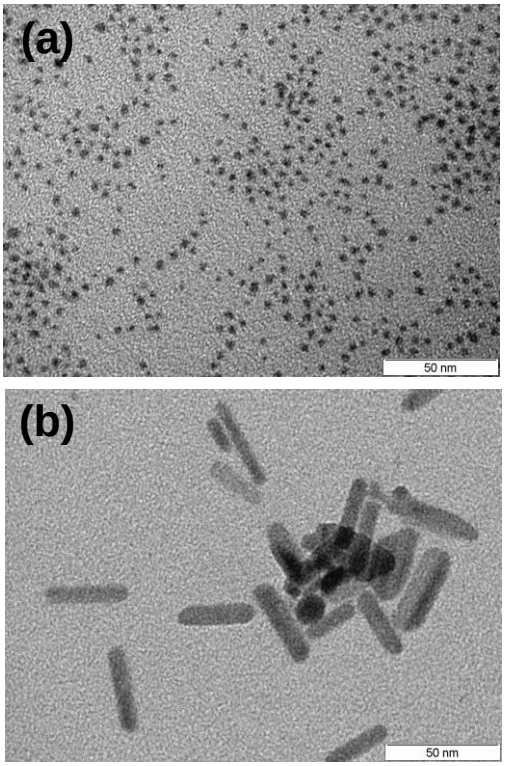

Fig.2. TEM images of Bi_2S_3 nanocrystals prepared at two injection temperatures.

Acknowledgement
This work was supported by the Spanish Ministry of Economy and Competitiveness (MINECO) under grant number TEC2012-34397 and Catalan authority under project 2014SGR1344.

Reference

[1] L. Cademartiri, R. Malakooti, P.G. O'Brien, A. Migliori, S. Petrov, N. Kherani, G.A. Ozin, "Large-scale synthesis of ultrathin Bi_2S_3 necklace nanowires ", *Angew. Chem., Int. Ed.*, 47, 3814 – 3817, 2008.
[2] T. Wu, X.G. Zhou, H. Zhang, X.H Zhong, "Bi_2S_3 nanostructures: A new photocatalyst", *Nano Res.*, 3, 379–386, 2010.
[3] L. Martinez, A. Stavrinadis, S. Higuchi, S.L. Diedenhofen, M. Bernechea, K. Tajima, G. Konstantatos, "Hybrid solution-processed bulk heterojunction solar cells based on bismuth sulfide nanocrystals", *Phys.Chem. Chem. Phys.*, 15, 5482-5487, 2013.
[4] L.S. Li, N.J. Sun, Y.Y. Huang, Y. Qin, N.N. Zhao, J.J. Gao, M.H. Li, H.H. Zhou, L.M. Qi, "Topotactic transformation of single-crystalline precursor discs into disc-like Bi_2S_3 nanorod networks", *Adv. Funct. Mater.*, 18, 1194–1201, 2008.
[5] Z.H. Ge, B.P. Zhang, J.F. Li, "Microstructure composite-like Bi_2S_3 polycrystals with enhanced thermoelectric properties", *J. Mater. Chem.*, 22, 17589-17594, 2012.
[6] X. Z. Liu, J. H. Cui, L. P. Zhang, W. C. Yu, F. Guo, Y. T. Qian, "Control to synthesize Bi_2S_3 nanowires by a simple inorganicsurfactant- assisted solvothermal process", *Nanotechnology*, 16, 1771-1775, 2005.
[7] Y.L. Zhang, J. Zhu, X. Song, X.H. Zhong, "Controlling the synthesis of CoO nanocrystals with various morphologies", *J. Phys. Chem. C*, 112, 5322–5327, 2008.
[8] K.L. Ai, Y.L. Liu, J.H. Liu, Q.H. Yuan, Y.Y. He, L.H. Lu, "Large-scale synthesis of Bi_2S_3 nanodots as a contrast agent for in Vivo X-ray computed tomography imaging", *Adv. Mater.*, 23, 4886–4891, 2011.

3-D Compact Model for Nanoscale Junctionless Triple-Gate Nanowire MOSFETs

Thomas Holtij [1,2], Michael Graef [1,2], Alexander Kloes [1], Benjamin Iniguez [2]

[1] Technische Hochschule Mittelhessen, Competence Centre for Nanotechnology and Photonics, Wiesenstrasse 14, Giessen 35390, Germany
[2] Universitat Rovira i Virgili, Department d'Enginyeria Electronica, Electrica i Automatica, Avda. Paıson Catalans 26, Campus Sescelades, Tarragona 43007, Spain

Abstract

A 3-D analytical and physics-based compact model for extremely scaled junctionless (JL) triple-gate nanowire (TGNW) MOSFETs is presented. Based on Poisson's equation and the conformal mapping technique, a compact solution for the electrostatics is derived in 3-D. A current expression is presented, which is continuous in all regions of device operation, and which takes into account the specific behavior of JL transistors. The model is compared versus measurement and simulated data of JL TG-NW MOSFETs, whereby the structural model parameters equal the values given by the fabricated devices. Important electrical parameters, such as threshold voltage V_T , drain-induced barrier lowering (DIBL) and subthreshold slope S are worked out.

1. Introduction

Junctionless transistors (JLTs) are touted as new candidates to handle upcoming manufacturing problems, related to abrupt pn-junctions, in future CMOS technology. The device is heavily doped, has no junctions and no doping concentration gradients while it provides full CMOS process compatibility. Improved electrostatic characteristics like near-ideal subthreshold slope, low leakage currents, high Ion=Ioff ratios, low DIBL and a lower gate capacitance are owed to the absence of the pn-junctions in JLTs. Additionally, their source/drain (S/D) engineering is simplified enormously [1-3]. The JLT's operational principle was detailed in [1].

In this work we target a JL TG-NW MOSFET (Fig. 1), because multiple-gate structures enable us to completely deplete the channel region easily. In general, the 3-D model is developed using Poisson's equation and the conformal mapping technique by Schwarz-Christoffel. The analytical solution for the electrostatics includes the dependence on the transistor's geometrical dimensions and N_d. The electrical parameters V_T, DIBL and S are calculated and investigated. A new current expression for JLTs rounds off the model. It is verified for different channel lengths L_g and N_d. A comparison versus measurement and 3-D TCAD [4] simulation data is performed.

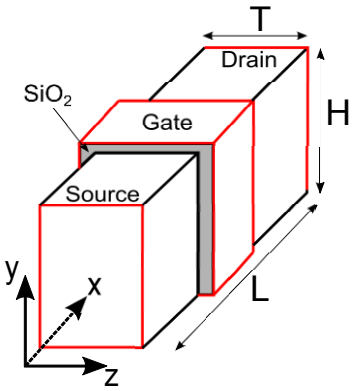

Fig.1. Sketch of the JL TG-NW MOSFET including its coordinate system. Red lines represents the source, drain and gate electrode, respectively.

2. 3-D Modeling Approach

In [5] a compact model for short-channel junctionless DG MOSFETs was presented. Based on this approach, a model extension to account for 3-D effects in triple-gate structures is developed. A similar procedure for lightly-doped junction-based devices was presented in [6]. Starting with 3-D Poisson's equation we have

$$\phi(x,y,z) = \frac{\partial \phi^2}{\partial x^2} + \frac{\partial \phi^2}{\partial y^2} + \frac{\partial \phi^2}{\partial z^2}.$$

To simplify matters and in order to find an analytical closed-form expression for the potential, the solution of Poisson's equation is split into three separate problems. These are called the source-related, the drain-related and the top-gate-related case, whereby detailed information about this decomposition can be found in [6]. Using this decomposition strategy, the result for the 3-D solution of the electrostatic potential is

$$\phi(x,y,z) = \phi_{2D}(x,z) + \varphi_{top}(y,z),$$

where ϕ_{2D} and φ_{top} represent the contributions of the decomposed potential problems related to source/drain and top-gate, respectively. The calculation of the 2-D potential is detailed in [5] and the calculation of the top-gate influence can be found in [6]. After that, we arrive at a modified current equation, which takes into account the specific behavior of JL MOSFETs, i.e. the

conduction mechanism in depletion and accumulation and the resulting effective gate capacitances.

$$I_{ds} = \frac{\mu\,(H_{ch} + T_{ch}/2)}{L_g}\left[V_{th}\,\tilde{\alpha}\,(Q_s - Q_d) + \frac{(Q_s^2 - Q_d^2)}{4\,\tilde{C}}\right]$$

Here, α and C are introduced to account for subthreshold slope degradation and the effect of volume inversion in the depletion region, respectively, whereby the transition to the accumulation region is smoothly modeled by using a tangent hyperbolic function, which ensures continuity even at derivatives of higher order.

3. Results and Discussions

Our model is compared versus measurement data, which were provided through "SQWIRE" project. Measuring was done by S. Barraud et. al., who is with the LETI in Grenoble, France. For details about the device fabrication, the reader is kindly asked to refer to [7]. The devices under investigation have various L_g. The fabricated gate stack gives an EOT = 1.2nm and the source/drain lengths are L_{sd} = 150nm. The measuring was done at T = 300K. In the model, the del Alamo model for the consideration of band gap narrowing effects is included [4]. In order to account for mobility degradation effects equations (37) and (38) from [6] are adapted. So far, the model does not include the effect of gate-induced drain leakage current.

Fig. 2 depicts the transfer characteristics of the JL NW MOSFET. On first sight, one can see that the model matches well the measurement data from depletion to accumulation region. Important electrical parameters such as the V_T, DIBL and S are well predicted. The DIBL is defined in terms of a threshold voltage shift.

$$\mathrm{DIBL} = V_T|_{V_d=0.05\,\mathrm{V}} - V_T|_{V_d=0.9\,\mathrm{V}}$$

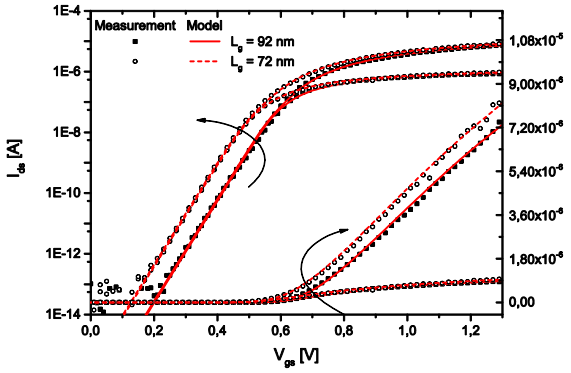

Fig.2. Transfer characteristics of the JL TG-NW MOSFET with: N_d=10^{19}cm^{-3}, V_d=0.05/0.9 [V], L_g=92/72 [nm], L_{sd}=150nm, T_{ch}=10nm, EOT=1.2nm, H_{ch}=9nm. Model versus measurement.

By decreasing L_g down to 42nm, V_T slightly rolls-off, as expected (Fig. 3). However, the DIBL is still very low (around 10mV) and S is insignificantly affected. Since the model matches well with the measurement data, we can estimate that the electrical model parameters are identical to the measured ones. Unlike in DG devices [9], the V_T roll-off, when downscaling L_g, is much lower in TG transistors, due to the increased control of the gate over the device's channel region (reduced SCEs).

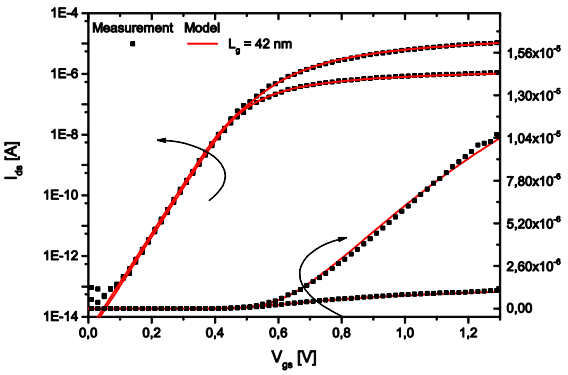

Fig.3. Transfer characteristics of the JL TG-NW MOSFET. Parameters as in Fig. 2 with: L_g=42nm.

Acknowledgments

This project was supported by the German Federal Ministry of Education and Research under contract No.1779X09, by German Research Foundation (DFG) under Grant KL 1042/3-1, by the European Commission under FP7 Projects ICTSTREP 257111 ("SQWIRE"), IAPP-218255 ("COMON"), by the Spanish Ministerio de Ciencia y Tecnolog´ıa under Projects TEC2011-28357-C02-01 and also by the ICREA Academia Prize. We also would like to thank people from CEA-LETI in Grenoble, France, for providing the measurement data.

References

[1] J.-P. Colinge, C.-W. Lee, A. Afzalian, N. D. Akhavan, R. Yan, I. Ferain, P. Razavi, B. O'Neill, A. Blake, M. White, A.-M. Kelleher, B. McCarthy, and R. Murphy, "Nanowire transistors without junctions," Nat Nano, vol. 5, pp. 225–229, Mar. 2010.

[2] J.-P. Colinge, A. Kranti, R. Yan, C. Lee, I. Ferain, R. Yu, N. D. Akhavan, and P. Razavi, "Junctionless Nanowire Transistor (JNT): Properties and design guidelines," Solid-State Electronics, vol. 65-66, pp. 33–37, 2011.

[3] J.-P. Colinge, I. Ferain, A. Kranti, C.-W. Lee, N. D. Akhavan, P. Razavi, R. Yan, and R. Yu, "Junctionless Nanowire Transistor: Complementary Metal-Oxide-Semiconductor Without Junctions," American Scientific Publishers, vol. 3, pp. 477–482, 2011.

[4] Synopsys, Inc., TCAD Sentaurus, C-2012.06 ed.

[5] T. Holtij, M. Graef, F. Hain, A. Kloes, and B. Iniguez, "Compact Model for Short-Channel Junctionless Accumulation Mode Double Gate MOSFETs," Electron Devices, IEEE Transactions on, vol. 61, no. 2, pp. 288–299, 2014.

[6] A. Kloes, M. Schwarz, and T. Holtij, "MOS3: A New Physics-Based Explicit Compact Model for Lightly-Doped Short-Channel Triple-Gate SOI MOSFETs," IEEE Trans. Electron Devices, vol. 59 (2) (2012), 2011.

[7] S. Barraud, M. Berthome, R. Coquand, M. Casse, T. Ernst, M. P. Samson, P. Perreau, K. Bourdelle, O. Faynot, and T. Poiroux, "Scaling of Trigate Junctionless Nanowire MOSFET With Gate Length Down to 13 nm," Electron Device Letters, IEEE, vol. 33, no. 9, pp. 1225–1227, 2012.

Fabrication of porous SU-8 surfaces using soft lithography

P. J. Eravuchira, A. Slota, M. Baranowska, J. Ferré-Borrull, E. Llobet, F. Diaz

Engineering of Materials and Micro/NanoSystems, University Rovira i Virgili,
Avinguda Paisos Catalans26, 43007, Tarragona, Spain
Tel. +34977256571, pinkie.jacob@urv.cat

Abstract

Structuring of SU-8 surfaces with pores of nanometric and micrometric dimensions using soft lithography is described here. Also we present the fabrication of SU-8 micropillars with nanopores and micropores obtained with the combination of photolithography and soft lithography.

1. Introduction

Soft lithography is a sheer simple, cost effective and rapid technique that uses elastomeric stamps to pattern soft materials such as polymers and photoresists [1]. Using this technique both two-dimensional and three-dimensional structures can be easily achieved, which might be harder and tedious to obtain using photolithography. Silicon, metals, or photoresists are generally used as the master templates in soft lithography, and one of the most commonly used elastomer molds is PDMS [2]. The application of soft lithography ranges from fabricating components in microelectronic, and optoelectronic to biotechnology [3]. SU-8, an epoxy-based negative photoresist has been extensively used in microfluidics, MEMS, and microelectronics for the past few decades [4]. Characterized by its biocompatibility, and non-toxicity, SU-8 has been considered as a valuable structural material in biological research. A biosensing technique based on the photoluminescence quenching of SU-8 with various surface functionalization (antibody-antigen interaction) has been already studied by us. We have observed that the quenching was higher for a sensing platform structured with SU-8 micropillar than that of a planar SU-8 surface. Therefore we assume that the further patterning of SU-8 micropillars with nanostructures might result in higher photoluminescence quenching due to the higher surface area available for functionalization. And thus the nanostructuring and microstructuring of SU-8 using an easy and low cost method is of great research interest for biosensing. In the present work, we illustrate the fabrication of porous SU-8 surfaces and SU-8 micropillar with pores using soft lithography.

2. Experiment

The patterning of porous SU-8 strutures involves mainly three steps; i) fabrication of a master template, ii) fabrication of PDMS stamp, and iii) replicating the pattern of master template onto the SU-8 using PDMS stamp.

We have used microporous silicon and nanoporous alumina as the master templates for the production of PDMS stamps with micropillar and nanopillar respectively. The microporous silicon was fabricated using electrochemical etching in (10:1 v/v) DMF: HF solution at a constant current of 5 mA for 10 minutes. The silicon wafer had a resistivity of 10-20 Ω cm, and the produced micropores had a diameter of 1 μm. The ordered nanoporous anodic alumina was fabricated using two-step anodization in 1% phosphoric acid. This was followed by pore widening of anodic alumina by wet chemical etching. This process resulted in an ordered arrangement of 200 nm diameter pores in alumina.

To obtain a soft PDMS mold, a 9:1(v/v) ratio of pre-polymer and curing agent (sylgard 184) was mixed, degassed, and finally poured over the master templates. The composite was then cured in the oven at 60^{o}C for 2h., and peeled off from the master templates once it was cooled down.

SU-8 nanoporous and microporous surfaces were produced by spin coating SU-8 onto cleaned glass substrates at a spinning speed of 800 rpm for 10sec., followed by spinning at an increased speed of 2500 rpm for another 30sec. The substrate was then soft baked at 65^{o}C for 5min. and then ramped to 95^{o}C and baked for another 8 min on a hot plate. During the soft bake, a high pressure was applied onto the PMDS by keeping a metal block of approximately 1Kg on the top of the stamp, which helps to press the PDMS stamp against the SU-8 surface well enough. After the soft bake, the PDMS stamp was peeled off from the SU-8 surface to release the porous SU-8.

The fabrication of SU-8 micropillars with nanopores or with micropores comprises of two steps; i) soft lithography to produce the porous pattern on a spin coated SU-8, and ii) photolithography of the SU-8 to obtain the porous micropillars. In order to fabricate the

micropillars the porous SU-8 surfaces were exposed under the UV light through a chromium mask for 9sec. The exposure was done using a mask aligner (MG 1410 from Karl Suss) equipped with an Hg lamp having wavelength ranging from 365-400nm, and a power of 350W. Consequently, to thermally cross-link the exposed part of the polymer, the glass slides were post baked at 65^{o}C for 3min. followed by 4 min. at 95^{o}C on a hot plate. Then the samples were allowed to cool down to room temperature. The post-baked samples were developed with PGMEA for 1min. and subsequently rinsed it with isopropanol for 10sec.

3. Results and discussion

Structural characterization of fabricated SU-8 structures was performed with environmental scanning electron microscope (ESEM). The ESEM images of SU-8 nanopores and SU-8 micropores are shown in fig. 1. The images verify the successful replication of nanometric and micrometric featured patterns of master template on SU-8 surface. In terms of geometry, the images show that the fabricated SU-8 surfaces retained the order, shape, and size of the PDMS stamps without any significant structural deformation.

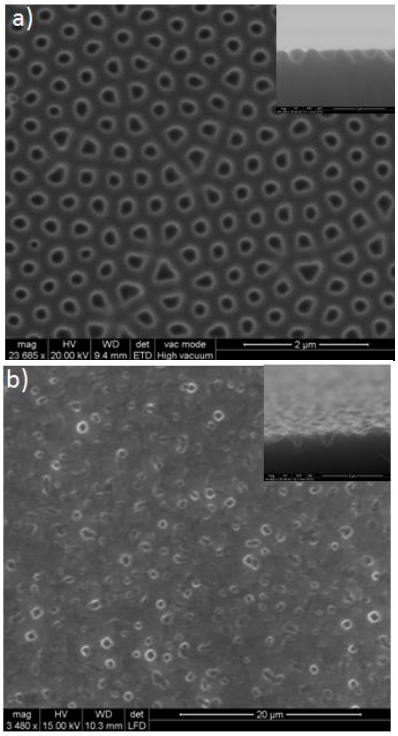

Figure 1: Top view SEM pictures (inset: cross sectional view) of SU-8 a) nanopores and b) micropores.

Figure 2 depicts the images of SU-8 micropillars with nanopores (a) and micropores (b). Similarly, SU-8 micropillars with porous structures also sustained the dimension and geometry without any deformation of pillars or pores. It is important to point out that the previous imprinting step on the SU-8 surface has no significant effect on the subsequent photolithographic conditions.

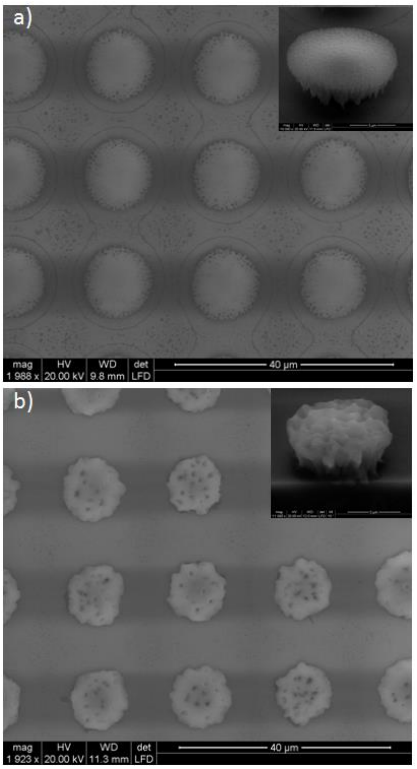

Figure 2: Top view (inset: cross sectional view) of SU-8 micropillars with a) nanopores and b) micropores.

4. Conclusions

Fabrication of nanometric and micrometric porous SU-8 strucutres using simple and cost effective soft lithographic technique is demostated. Besides, 3D SU-8 micropillars with nanopores and micropores on it were also achieved with a combination of photolithography with soft lithogrpahy. Furthur investigations will be carried out on these porous SU-8 structutes as a tool for biosensing.

5. Acknowledgment

This work was supported by the MINECO (TEC2012-34397) and by Catalan Government (AGAUR 2014 SGR 1344).

References

[1] Y. Xia, G. M. Whitesides, Soft lithography, Annu. Rev. Mater. Sci., 28, pp 153–184, 1998.

[2] D. J. Lipomi, R.V. Martinez, L. Cademartiri, G.M. Whitesides, Soft Lithographic Approaches to Nanofabrication, Polym. Sci., 7, pp 211-231, 2012.

[3]Wolfe D. B., Qin D., Whitesides G. M., Rapid prototyping of microstructures by soft lithography for biotechnology, Methods Mol. Biol., pp 81-107, 2010.

[4] S. Tuomikoski, S. Franssila, Free-standing SU-8 microfluidic chips by adhesive bonding and release etching, Sensors and Actuat. A, 120, pp 408–415 2005.

Modulated Transponder for Radar Applications

J. Lorenzo, A. Lazaro, R. Villarino and D. Girbau

Department of Electronics, Electric and Automatic control Engineering, universitat Rovira i Virgili
Av. Paisos Catalans, 26, 43007 Tarragona, Spain – Javier.lorenzo@urv.cat - +34 977 29 70 48

Abstract

This paper presents an active backscatter transponder at X-band suitable for FMCW radar applications. In order to maximize its read range the radar cross section (RCS) of the transponder is increased by means of a two-stage amplifier based on HEMT transistors, which is connected between two bowtie antennas. The transponder response is distinguished from the intertference of non-modulated clutter by modulating its RCS actuating on the bias of the transistors. The backscattered response of the transponder is collected using a FMCW radar. Theoretical operation and experimental results are presented, achieving measurements at 18 m.

1. Introduction

FMCW (Frequency Modulated Continuous Wave) radar is a short-range radar that transmits a signal that is usually swept linearly in frequency. Echoes from a target are mixed with the transmitted signal to produce a beat signal whose frequency is proportional to the distance between the radar and the target [1]. FMCW radars are commonly used in several applications such as: altimeters, tank levels where high-resolution non-contact measurements in harsh conditions are required [2], marine radars [3] or automotive collision avoidance radars [4]. In recent years, FMCW radar has also been used as reader for long-distance transponders integrating different types of sensors such as pressure or temperature sensors [5]. One of the problems to detect the target is the clutter contamination derived from multipath reflections [6]. This is of major concern when the target radar cross section (RCS) is smaller than that of other surrounding objects. In order to mitigate this problem, a modulated backscatter transponder has been proposed in [7]. In this case the spectrum at the output of the mixer is shifted by the modulated frequency of the tag, f_{tag}. The range measurement is performed by analyzing the spectrum of the beat signal around f_{tag} and by verifying the presence of a couple of peaks. The frequency difference between peaks is proportional to the distance between the radar and the tag. The use of retrodirective properties of Van Atta arrays in the design of transponders allows obtaining high RCS for wide observation angles. Modulated passive Van Atta array has been proposed in [8] using PIN diodes switches. Active Van Atta arrays are also investigated to reduce the effect of the losses of the transmission lines that connect the antennas [9-10]. Combined injection locking techniques and retrodirective active Van Atta arrays are proposed in [9]. Retrodirective techniques often use narrow band patch antennas as radiation elements [10]. In addition, the power consumption of an RF oscillator in secondary radars or the power consumption of active Van Atta arrays is high, and the design is complex and expensive. The high RCS can be achieved modulating high gain antennas but then the tag needs to be oriented to the reader. The aim of this work is to study the feasibility to use wide-band backscatter active transponders including a low-power consumption amplifier and low-gain decoupled antennas. This paper presents an active modulated transponder with low-power consumption that can be readed at 18 m. The paper is organized as follows. Section 2 deals about the basic theory of the backscattered transponder and describes a transponder designed as a proof of concept. Experimental results are described in Section 3. Section 4 draws the conclusions.

2. Modulated Transponder Operation and Design

A. Operation theory

Fig. 1 shows a block diagram of the proposed system composed by the FMCW radar and the transponder. The radar interrogates the transponder and it answers modulating its RCS. The transponder consists of two bowtie antennas interconnected by an amplifier controlled by an oscillator circuit. The backscattered field is modulated controlling the amplifier bias current. Assuming that the frequency of the transmitted signal is swept linearly, it can be written as:

$$x_T(t) = A\cos\left(2\pi\left(f_c t + \frac{1}{2}\mu t^2\right)\right) \quad (1)$$

where A is the amplitude, f_c is the carrier frequency, $\mu=B/T$, T and B are the sweep slope, duration and bandwidth respectively. The backscattered received signal is the transmitted signal delayed by the round-trip time of flight (τ), attenuated and modulated at frequency f_{tag}.

$$x_R(t) = A'\cos\left(2\pi\left(f_c(t-\tau)+\frac{1}{2}\mu(t-\tau)^2\right)\right)\cos\left(2\pi f_{tag}t\right) \quad (2)$$

where $\tau=2d/c$, d is the transmitter to transponder distance and c is the speed of light, A' is the received amplitude. The spectrum of the received signal is schematically shown in Fig.2. Two cases are considered. The first case addresses a non-modulated transponder. Here the distance is obtained using the FMCW radar equation and the transponder is difficult to be detected due to the phase noise and because it is interfered by the reflections at surrounding objects with higher RCS (e.g. metallic objects).

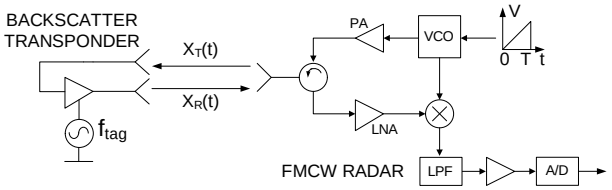

Fig.1. Schematic block diagram by the transponder and the FMCW radar reader.

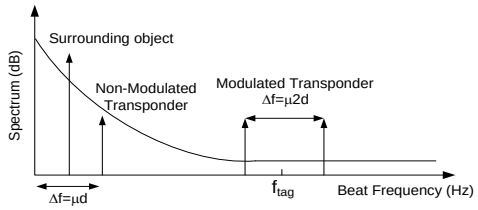

Fig.2. Spectrum of received signal using a non-modulated and modulated transponder and a parasitic reflector.

The second case addresses a modulated transponder. Now a couple it can be detected from a couple of peaks that appear around f_{tag}. Here the distance can be obtained from the frequency separation (Δf) between a couple of peaks that appear around f_{tag} the separation between the these peaks, Δf, which is proportional to the distance.

$$\Delta f = \mu\tau = \mu 2d/c \rightarrow d = c\Delta f/(2\mu) \qquad (3)$$

In the latter, the transponder can be detected more easily because the interference from clutter and noise floor is smaller and detection is limited by the receiver noise figure instead of the phase noise.

B. Transponder design

A proof-of-concept transponder is manufactured using Rogers 4003 substrate (relative permittivity εr=3.54, loss tangent tanδ=0.003, and height 32 mil). The transponder operates between 9.25 GHz and 10.75 GHz, because it is the frequency band of the FMCW radar used as reader (Siversima RS3400X). In order to achieve the bandwidth requirements, two wideband bowtie dipole antennas, designed with ADS/Momentum are integrated in the transponder. The length of the arms is 6.6 mm and the angle is 70 degrees. A balun is implemented by means of a 13.5 mm tapered microstrip line that converts the balanced feed line into a 50 Ω microstrip line. In order to increase the gain A metallic reflector is located at 7 mm to increase antenna gain. A two-stage amplifier based on CEL NE3503M04 HEMT transistors is placed between transmitter and receiver antennas (see Fig.3.a). The oscillator that modulates the transponder (Fig.3.b) is generated using a 555 timer oscillator (Fig.3.c shows the oscillator schematic block diagram) and it drives the drains of transistors (V_{D1}, V_{D2} at 2.5 V and I_{Ds} at 25 mA), whereas the gate voltages (V_{G1}, V_{G2}) are set to -0.3 V. A key point in this transponder is to minimize the coupling between antennas. Fig.4 shows the open-loop gain computed from the cascade simulation of the antennas coupling with and without amplifier. It can be seen that the coupling between antennas is enough small to avoid oscillation.

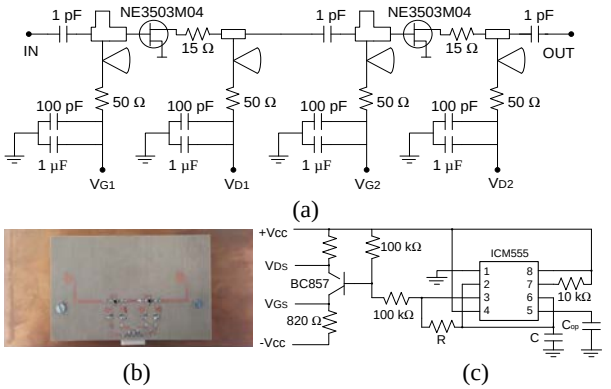

Fig.3. Amplifier schematic (a);photography of the transponder and the ground (b);oscillator schematic (c).

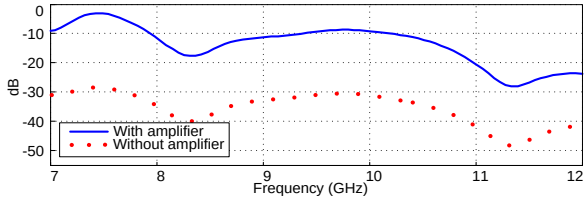

Fig.4. Open-loop gain without and with amplifier.

The amplitude of the modulated reflected signal is a function of the RCS of the active transponder that it is given by [11]:

$$\sigma = \frac{\lambda^2}{4\pi} G_{tag,r} G_a G_{tag,t} \qquad (4)$$

where λ is the wavelength, $G_{tag,r}$,$G_{tag,t}$ are the transponder receiver and transmitter antenna gains, respectively, and G_a is the amplifier gain. Fig. 5 shows the computed RCS using (4). A large enhancement due to amplifier gain can be observed.

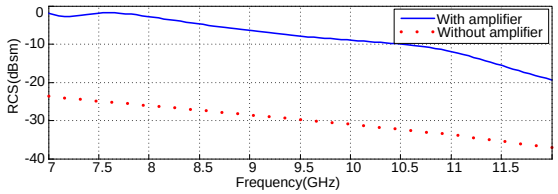

Fig.5. Simulated RCS as a function of frequency with (solid line) and without (dashed line) the amplifier.

3. Experimental Results

The experimental setup described in Fig.1 is used to measure the modulated transponder. A strong peak at the transmitted frequency due to the coupling between

transmitter and receiver antenna and the sideband peaks originated by the modulation of the transponder are also observed. Measurements in outdoor environment between 3 and 18 m are performed using commercial radar RS3400X from Siversima. It is a synthesized X-band FMCW radar front-end. The nominal transmitted power is 0dBm+/-5dB. The radar sweeps the 9.25-10.75 GHz frequency band with sweep time of 75 ms and it is connected to a 20 dB standard pyramidal horn. Fig.6.a shows the measurement of the transponder at 8 m without modulation and Fig.6.b shows the measurement of the transponder modulated at 7 kHz. Here a background subtraction technique is applied, subtracting the measurement of Fig.6.a. The peaks are clearly detected (black circles). The maximum non ambiguous distance is limited by the sampling frequency of the A/D converter used [20] (20 KHz for the Siversima controller card used in our case). Fig. 7 shows the sideband peaks obtained from the measurement of the modulated transponder at different distances (from 3.2 m to 13.5 m).

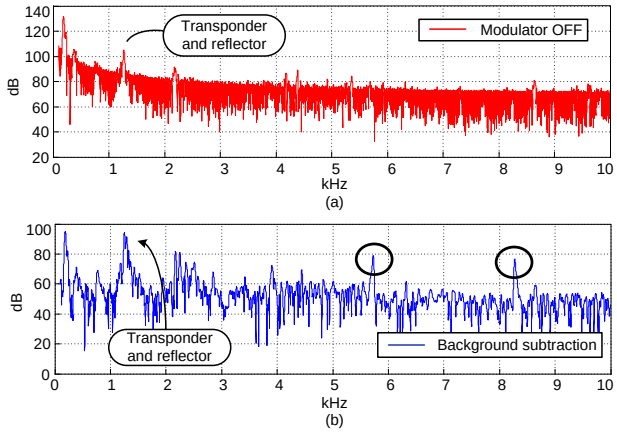

Fig.6. Measurement comparison of the transponder and reflector at 8 m in case of no modulation (a) or with f_{tag}=7 kHz modulation (b).

The distances are derived from the spacing between the peaks and match with the measured distances between the radar and the transponder. Now a 90º rectangular dihedral reflector (20 cm by 29 cm) is located in the vicinity of the transponder. This reflector presents a high RCS (19.7 dB oriented to the radar) Fig. 8 shows the estimated distance obtained from the measurement of the transponder and from the reflector. The offset between the measured and actual distance between the radar and the transponder is due to the delay introduced by the cables that connect the radar and the antenna. This systematic offset has been subtracted in all measurements.

4. Conclusions

This work has studied the feasibility of using an active backscattered modulated transponder based on a two-stage amplifier and a couple of bowtie antennas for FMCW radar applications. The basic operation theory of the system is explained. Since the RCS is modulated, interferences which come from non-modulated clutter can be removed using a simple background subtracting technique, which consists on subtracting the modulated and no modulated transponder measurements. Experimental results are obtained using commercial low-power FMCW radar working as a reader. The use of an amplifier allows to detect the transponder at distances up to 18 m near the non ambiguous distance.

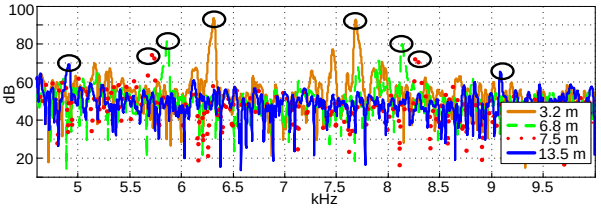

Fig.7. Measurement comparison of the transponder with ftag=7 kHz modulation with background subtraction.

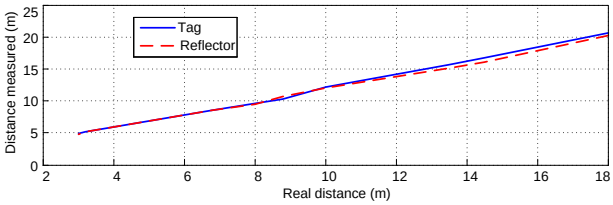

Fig.8. Distance obtained from the reflector (dashed line) and derived from the spacing between the peaks (solid line).

References

[1]M.I. Skolnik, “Introduction to Radar Systems ,” in McGraw-Hill, 2nd ed. Singapure, 1981.

[2]D. Brumbi, “Low power FMCW radar system for level gauging,” in IEEE MTT-S Intr. Microwave Symp. Digest, Boston, MA (USA), 2000, vol. 3, pp. 1559-1562.

[3]Y. Huang, P.V. Brennan, D. Patrick, I.Weller, P. Robertis, K.Hughes, “FMCW based mimo imaging radar for maritime navigation,” in Prog. In Electromgetics Rsch, vol. 115, pp. 327-342, 2011.

[4]S.-H.Jeong, H.-Y. Yu, J.-E. Lee, J.-N. Oh, K.-H. Lee, “A Multi.Beam and Multi-Range Radar with Fmcw and Digital Beam Forming for Automotive Applications,” in Prog. In Electromagnetics Rsch., vol. 124, pp. 285-299, 2012.

[5]P.Pons, H.Aubert, P.Menini, M.Tentzeris, “Wireless Passive autonomous Sensors with Electromagnetic Transduction,” in Int. Conf. on Micrw and High Freq. Heating, Toulouse (France), 2011.

[6]J.Thornton, D.J.Edwards, “Range measurement using modulated retro-reflectors in FM radar system,” in IEEE Microwave Guided Wave Lett., vol. 10,pp. 380-382, 2000.

[7]M.Kossel, H.R.Benedickter, R.Peter, W.Bächtold, “Microwave backscatter modulation systems,” in IEEE Int. Microwave Symp. Dig., Boston, MA (USA), 2000, pp. 1427-1430.

[8]J.A.Vitaz, A.M. Buerkle, K.Sarabandi, “Tracking of metallic objects using a retro-reflective array at 26 GHz,” IEEE Trans. on Antennas and Propagation, Vol. 58, No.11, pp.3539-3544, 2010.

[9]C.Luxey, J.-M., Laheurte, "A retrodirective transponder with polarization duplexing for dedicated short-range communications," IEEE Trans. on Micrw. Thry. and Techniques, vol.47, no.9, pp.1910-1915, Sep 1999

[10]T.-J. Hong; S.-J. Chung, "24 GHz active retrodirective antenna array," Elec. Ltt,vol.35, no.21, pp.1785-1786, 1999.

[11]D. R. Brunfeldt and F. T. Ulaby, “Active Reflector for Radar Calibration,” IEEE Trans. On Geoscience and Remote Sensing, Vol.GE-22, No.2, pp.165-169, March 1984.

Digital Control of a Unidirectional Battery Charger for Electric Vehicles

A. Marcos-Pastor, E. Vidal-Idiarte, A. Cid-Pastor and L. Martínez-Salamero
Electronics, Electrical and Automation Engineering Department (DEEEA)
Universitat Rovira i Virgili. Tarragona, Spain,
E-mails: {adria.marcos, enric.vidal, angel.cid, luis.martinez}@urv.cat

***Abstract* — The digital control of a unidirectional battery charger of 3 kW for electric vehicles is presented. The selected electrical architecture consists of a two-stage topology composed of a rectifier for power factor correction followed by a converter that manages the charge of the battery. Both stages are based on three 1 kW interleaved converters. In particular, first stage cells are boost converters while the second stage cells are buck converters. The control of inductor currents has been obtained by applying discrete-time sliding mode control theory at constant switching frequency. An outer control loop is meant to regulate the DC-link capacitor voltage between both stages and another loop regulates the charge of the battery.**

I. INTRODUCTION

Electric vehicles (EVs) and Plug-in Electric Vehicles (PHEV) stand for the best alternative to reduce the emission of greenhouse gasses due to their low consumption of fossil fuels. Battery chargers play an important role within the paradigm of EVs. Different classifications of battery chargers can be found in the literature [1].

Unidirectional battery chargers are frequently implemented due to their low cost, volume and reduced number of components as well as their simplicity of the required control strategy that manages the system. In turn, bidirectional battery chargers allow both the absorption and the injection of energy to the grid [2]. However, this capability implies a major cost and complexity of hardware and control.

In general, two-stage battery chargers are composed of an input filter for interferences (EMI), an AC/DC rectifier for Power Factor Correction (PFC) and a DC/DC converter to manage the energy delivered to the battery. In this paper, a digital control for a 3 kW unidirectional non-isolated EV battery charger is presented. The proposed electrical architecture is composed of an input diode bridge followed by three interleaved boost cells for the PFC stage, a DC link and three interleaved buck cells connected to the battery for the DC/DC stage.

In this work, the application of discrete-time sliding mode control (SMC) technique [3] to operate at a constant switching frequency is proposed. A detailed description of the system is given in section II. Section III presents the design of the digital control while section IV presents the simulated results of the whole system. Conclusions are outlined in section V.

II. SYSTEM DESCRIPTION AND OPERATION

The first stage of the proposed battery charger has an input diode bridge followed by three interleaved boost cells whereas the second stage is composed by three interleaved buck cells connected between the DC-link and the battery (Fig. 1). The digital controller is going to sense the rectified input voltage $v_{in}(t)$, the DC-link voltage $v_C(t)$, the battery voltage $v_{bat}(t)$ and currents $i_{Lj}(t)$ and $i_{Lk}(t)$ at $t = nT_{sw}$ that is beginning of the n^{th} switching period T_{sw} of each cell. To simplify the figures and the mathematic analysis that follows, j and k subscripts have been introduced for boost and buck cells respectively whose values can be 1, 2 or 3 for j and 4, 5 and 6 for k.

Fig. 2 illustrates a block diagram of the proposed digital controller. It is composed by analog-to-digital converters, the control algorithm and the digital PWM modules that generate $u_j(t)$ and $u_k(t)$ control signals for MOSFETs M_j and M_k respectively. The fast control loops for inductor currents calculate d_j^n and d_k^n duty cycles control laws obtained by the application of the discrete-time SMC theory [3]. Control law d_j^n is meant to impose a Loss-Free Resistor (LFR) behavior to guarantee a correct PFC [4] meanwhile control law d_k^n is going to control the current of the battery. Moreover, the duty cycle calculation depends on current references $i_{Lj,ref}^n$ and $i_{Lk,ref}^n$. Duty cycles d_j^n and d_k^n can be defined as discrete-time variables given by the following expression:

$$d_q^{\,n} = d_q(t)\big|_{t=nT_{sw}} = \frac{\tau_q^{\,n}}{T_{sw}} \tag{1}$$

where q can be j or k and τ_q^n is the duration of the conduction state of the MOSFET for the n^{th} switching. Duty cycle d_q^n must be restricted within the interval (0, 1) to maintain constant the switching frequency.

DC-link voltage will be regulated by a slower second control loop that is going to calculate the conductance g^n for the pre-regulator PFC stage and generate the current reference $i_{Lj,ref.}^n$. Conductance g^n will be determined by the sum of two terms, one related to the power balance characteristic (AB/C^2) and the output of a PI compensator ($G_1(z)$) to ensure the regulation of DC-link voltage at the desired value.

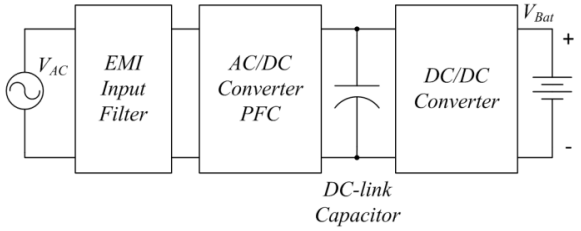

Fig. 1. General block diagram of a battery charger for EVs.

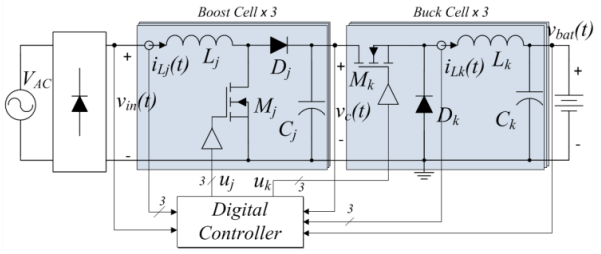

Fig. 2. Scheme of the unidirectional battery charger with digital control.

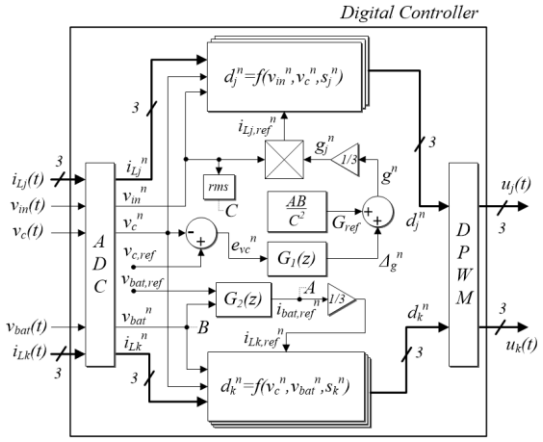

Fig. 3. Block diagram of the digital controller.

III. Digital Control Design

The digital control design is structured in two parts: the design control of inductor currents and the design of the outer loop for the DC-link voltage regulation. The algorithm to control inductor currents are the following:

$$\tau_{eq,j}^{\ n} = \frac{L_j\left(i_{Lj,ref}^{\ n} - i_{Lj}^{\ n}\right) + T_{sw}\left(v_c^{\ n} - v_{in}^{\ n}\right)}{v_c^{\ n}} \quad (Boost)$$

$$\tau_{eq,k}^{\ n} = \frac{L_k\left(i_{Lk,ref}^{\ n} - i_{Lk}^{\ n}\right) + T_{sw} v_{bat}^{\ n}}{v_c^{\ n}} \quad (Buck) \qquad (2)$$

The transfer function that relates the conductance with the DC-link capacitor voltage is the following:

$$\frac{V_c(z)}{G(z)} = -\left(\frac{V_{c,e} L_{eq}}{R_o C_o}\right) \frac{z - \left(1 + \frac{V_{in}^{\ 2} T_{sw} R_o}{V_{c,e}^{\ 2} L_{eq}}\right)}{z\left(z + \left(\frac{2T_{sw}}{R_o C_o} - 1\right)\right)} \qquad (3)$$

To regulate the DC-link capacitor voltage, parameter g^n will be calculated as the sum of both a Proportional-Integral controller $G_1(z)$ and the G_{ref} value of Fig. 3.

IV. Simulation Results

Different simulations have been realized using PSIM to validate the performance of the proposed digitally controlled two-stage 3 kW EV battery charger. The system parameters and components are presented in TABLE I.

TABLE I. Battery Charger Characteristics

Parameter	Value
V_{AC}	230 V_{rms}
$v_{c,ref}$	420 V
$v_{bat,max}$	380 V
$i_{bat,ref\ max}$	7.9 A
$P_{bat,max}$	3 kW

Component	Value
L_j	620 µH
L_k	620 µH
C_j	300 µF
T_{sw}	60 kHz

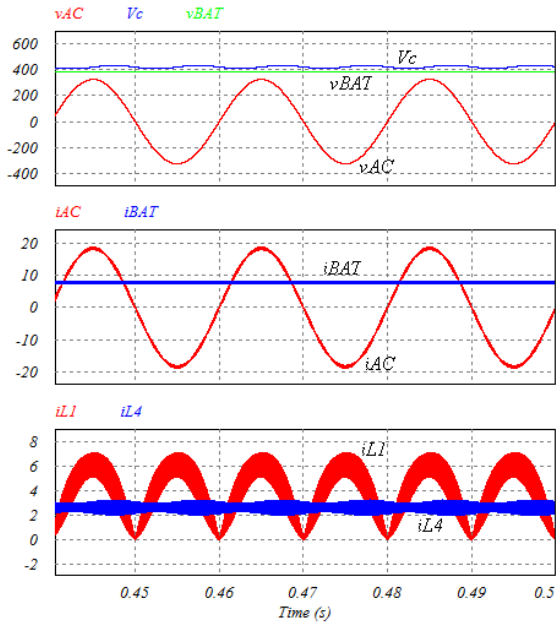

Fig. 4. Battery charger variables at maximum output power. a) v_{AC}, v_c and v_{bat}. b) i_{AC} and i_{bat}. c) i_{L1} and i_{L4}

V. Conclusions

In this work a digital control of a 3 kW unidirectional two-stage battery charger for EVs has been proposed. The AC-DC and DC-DC stages are based on three interleaved boost and buck cells, each of them of 1 kW respectively. The control of inductor currents has been obtained by means of the application of discrete-time SMC theory that allows the operation at a constant switching frequency. We are currently working towards experimental results from a real implementation.

References

[1] M. Yilmaz and P. T. Krein, "Review of Battery Charger Topologies, Charging Power Levels, and Infrastructure for Plug-In Electric and Hybrid Vehicles," *Power Electronics, IEEE Transactions on*, vol. 28, pp. 2151-2169, 2013.

[2] Z. Xiaohu, S. Lukic, S. Bhattacharya, and A. Huang, "Design and control of grid-connected converter in bi-directional battery charger for Plug-in hybrid electric vehicle application," in *Vehicle Power and Propulsion Conference, 2009. VPPC '09. IEEE*, 2009, pp. 1716-1721.

[3] V. Utkin, *Sliding modes and their application in variable structure systems*: Mir Publishers, 1978.

[4] A. Marcos-Pastor, E. Vidal-Idiarte, A. Cid-Pastor, and L. Martinez-Salamero, "Digital Loss-Free Resistor for power factor correction applications," in *Industrial Electronics Society, IECON 2013 - 39th Annual Conference of the IEEE*, 2013, pp. 3468-3473.

Layer by layer polyelectrolytes deposition on Nanoporous Alumina for retained drug release

Maria Porta-Batalla, María Alba, Gerard Macias, Pilar Formentín, Elisabet Xifré, Lluís F. Marsal*

Departemant d'Enginyeria Electrònica, Elèctrica i Automática, ETSE, Universitat Rovira i Virgili, Avda. Països Catalans 26, 43007 Tarragona, Spain

*Corresponding author. Tel: 977 559 625 E-mail: lluis.marsal@urv.cat

Abstract

Stimuli-responsive materials that could change their properties and structures in response to external stimuli have recently received much attention owing to their many potential applications in drug delivery systems. Among various preparation methods to realize these goals, layer-by-layer (LBL) assembly, based on polyelectrolytes leading to swellable multilayers, is a powerful processing method because it can be applied to substrates of any shape and size and, at the same time, the multilayer films assembled under specific conditions show a strong swelling behavior that can be modulated in response to post-treatment conditions. The aim of this study is to use polyelectrolytes multilayers onto de nanoporous anodic alumina (NAA) in order to have the maximum surface to load the drugs and have a retained drug release compared to those samples without polyelectrolytes.

1. Introduction

Since the human body exhibits variations in pH along the gastrointestinal tract from the stomach (pH 1.0 - 3.0), to the small intestine (pH 6.5-7.0), to the colon (pH 7.0-8.0) and also in some specific areas like tumoral tissues (pH 6.5-7.2) and subcellular compartments, such as endosomes/lysosomes (pH 5.0-5.5), one very important drug delivery system is those sensitive to the pH. [1]. With this state of the art, pH-sensitive polyelectrolytes are good candidates for drug delivery uses.

2. Experimental Section

Nanoporous alumina anodization

Ordered nanoporous anodic alumina (NAA) was prepared by the two-step anodization method.

NAA membranes were prepared by the two-step anodization method. High purity (99.999%) aluminum plates were purchased from Goodfellow (Huntingdon, UK). Perchloric acid and phosphoric acid which were used as electrolytes, for anodization (phosphoric acid) and electropolishing (perchloric acid), were purchased from Sigma-Aldrich Corporation (St Louis, USA).

Aluminum plates were degreased in acetone and ethanol to eliminate organic impurities. They were then subsequently electropolished in a mixed solvent of perchloric acid and ethanol (1 : 3) at a constant applied voltage of 20 V for 4 min at a reaction temperature of 4ºC.

To suppress breakdown effects and to enable uniform oxide film growth at high voltage (194V in phosphoric acid) a protective layer at lower voltage (174V in phosphoric acid) was performed for 180 min. After this pre-anodization a ramp of 0,05V/s was used to reach the hard voltage (194V) during 24h. Then, after this first step, the porous alumina grown on the aluminum surface was removed by a wet chemical etching in a mixture of phosphoric acid (0,4M) and chromic acid (0,2M) (1:1 volume ratio) at 70ºC. [2] The second anodization step was performed under the same experimental conditions (194V) as they were used in the first step in order to obtain ordered nanoporous alumina. The anodization area were 36 circles of a diameter around 6mm. During the anodization the temperature and velocity of stirring of the electrolyte were kept constant.

Polyelectrolytes assembly

Three groups of NAA substrates were done: control samples (without polyelectrolyte treatment), polyelectrolyte samples (with 20 bilayers of polyelectrolyte deposition) and APTES-treated with polyelectrolyte deposition samples (with APTES-treatment and 20 bilayers of polyelectrolyte deposition). For LBL deposition, the NAA substrates were immersed consecutively into solutions of poly(styrenesulfonate) (PSS, 1mg/ml in 20mM $CaCl_2$ in deionized water), deionized water, and poly(allyl amine) (PAH, 1mg/ml in 20mM $CaCl_2$ in deionized water). Dipping times in polyelectrolyte solutions were 30 min, the washing step in deionized water lasted for 10 min, and all the steps were repeated for 20 times. [3]

The morphologies of the NAA substrates and the polyelectrolytes layers were characterized by Environmental Scanning Electron Microscopy (ESEM). (Fig. 2) The initial porous measurements were 135 nm in diameter and 4µm in depth.

Drug loading and release studies

Positively charged doxorubicin hydrochloride (DOX) was selected as a model drug. 5 ml of DOX solution (1.0 mg/ml) at room temperature was adjusted to pH 2.0 with 0.1 M HCl. The suspension was stirred for 10 h in the dark with the samples immersed, followed by adjustment to pH 8.0 with 0.1 M NaOH and further stirring for 2 h. [1]

Drug release was measured by drug photoluminescence. The photoluminescence measurements were taken on a fluorescence spectrophotometer from Photon Technology International Inc. (Birmingham, NJ, USA) with a Xe lamp used as the excitation light source at room temperature and an excitation wavelength (λex) of 480 nm.

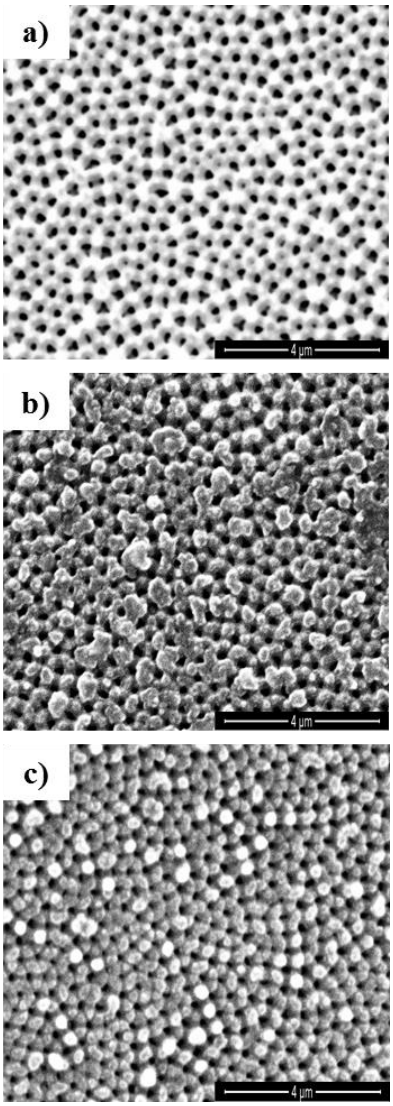

Fig. 1. ESEM images of NAA substrates with (a)control surface without polyelectrolytes (mean diameter value 280.9 nm), (b)surface with polyelectrolytes (mean diameter value 214.8 nm), (c)APTES-treated surface with polyelectrolytes (mean diameter value 186.8 nm)

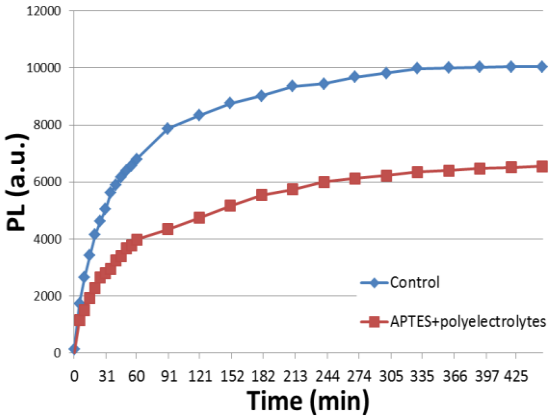

Fig. 2. Photoluminescence release of DOX with PBS at pH 7.

3. Conclusions

Good polyelectrolyte deposition in both surfaces: APTES-treated NAA and the non-treated NAA have been found. It can be assumed that pores of 135 nm of diameter are not completely covered by 20 layers of polyelectrolytes using 20 mM salt concentration. More homogenous polyelectrolyte deposition in APTES-treated samples has been obtained than the non-treated ones. Higher drug volumes have been loaded in control samples due to the drug storage in larger porous. However, retained drug releases have been observed in polyelectrolytes assembled samples. Further release studies with different pH values will be needed to ensure pH-dependent differences in release.

Acknowledgements

This work was supported by the Spanish Ministry of Economy and competitiveness (MINECO) under grant number,TEC2012-34397 and by Catalan authority under project AGAUR 2014 SGR 1344.

References

[1] Yang, Y. J., Tao, X., Hou, Q., Ma, Y., Chen, X. L., & Chen, J. F. (2010). Mesoporous silica nanotubes coated with multilayered polyelectrolytes for pH-controlled drug release. Acta biomaterialia, 6(8), 3092-3100.

[2] G. C. Schwartz, V. Platter, Journal of the Electrochemical Society 123, 34 (1976)

[3] a ou i, , Tranc ida, D , Sc n err, Pushing the Size Limits in the Replication of Nanopores in Anodized Aluminum Oxide via the Layer-by-Layer Deposition of Polyelectrolytes. Langmuir, 28(26), 10091-10096.

Gas sensing properties of ZnO nanowires grown via vapor-liquid-solid method over sapphire substrates

S.Roso[1,3], F.Güell[2], E.Llobet[1]

[1]*Minos-Emas. University Rovira i Virgili. Avda. PaïsosCatalans 26, 43007 Tarragona, Spain*

[2]*Departament d'Electrònica, Universitat de Barcelona. C/ Martí Franquès 1, 08028 Barcelona, Spain*

[3]*Institute of Chemical Research of Catalonia (ICIQ), Avda. Països Catalans 16, 43007 Tarragona, Spain*

Abstract

In the present work we have synthesized ZnO Nanowires NWs via the vapor-liquid-solid method (VLS) over different kind of sapphire substrates; c-plane, r-plane and a-plane. We obtained ZnO NWs oriented in different directions depending on the crystallographic direction of the substrates. We applied this sensors to some reducing and oxidizing gases that are harmful to human helath such as EtOH, NO2 and C6H6.

1. Introduction

Zinc oxide (ZnO) has been considered as one of the best materials for its economic and large scale optoelectronic applications. ZnO is a wide direct band-gap semiconductor, 3.37 eV at room temperature, and has an extremely large binding energy, 60 meV, much higher than other materials such as GaN (25 meV). The reduced size of nanostructures such as (1D) nanowires (NWs), gives us new mechanical, chemical, electrical and optical properties due to its large surface to volume ratio [2]. The key goal of nanostructure research is to control structure, which opens the door to new structure-function relationships. The fundamental advantage of nanostructures is that they offer something different to the bulk materials in terms of size, structure and functionality. For these properties 1D ZnO NWs have great potential for many applications such as solar cells, waveguides, lasers, LEDs and gas sensors.

2. Experimental Tecnhique

ZnO NWs were synthesized through the VLS method using a chemical vapour deposition (CVD) furnace. VLS growth mechanism was firstly introduced by Wagner and Ellis in the early 1960s for Au-catalysed Si whiskers in the range of micrometers [8]. Mainly, the VLS growth process can be divided in three principal steps: 1)Creation of a liquid alloy of the Au catalyst and the material to deposit, 2) nucleation of the material in the solid-liquid interface and 3)growth of the NWs. The nucleation and growth of the solid ZnO NWs occur due to supersaturation of the liquid droplet [9]. Incremental growth of the NW taking place at the droplet interface constantly pushes the catalyst upwards. First of all, Au thin layers from 3 to 30nm, that will act as a catalyst, have been deposited by sputtering. The mixture used as powder is ZnO and graphite (125 mg) and Ar as the carrier gas. To synthesize ZnO via VLS is essential to decompose the powder into Zn2+ and O-2, which occurs at high temperature. In order to reduce this temperature, the ZnO powder is usually mixed with graphite, so the decomposition takes place at 850ºC. we grew the ZnO NWs over Al2O3 substrates with three different crystallographic directions, the c-plane (0001), the a-plane (11-20), and the r-plane (1-102).

3. Results and discussion

The ZnO nanowires grew differently depending on the crystallographic direction of the substrate, because it is well known that NWs grow following the crystalline structure of the substrate. For the c-plane the nanowires grew at 51º and 129º, for the r-plane, the NWs grew with a nanorod shape and for the a-plane the NWs grew vertically aligned.

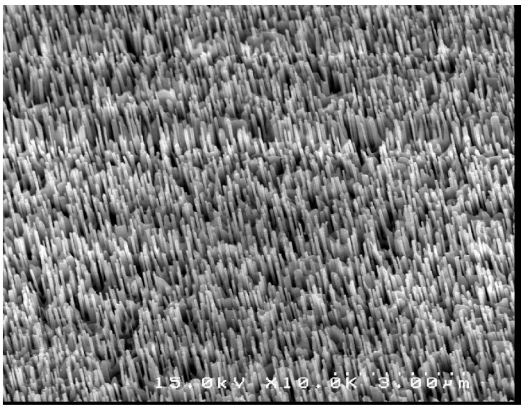

Fig.1. SEM image of the nanowires vertically aligned for the a-plane.

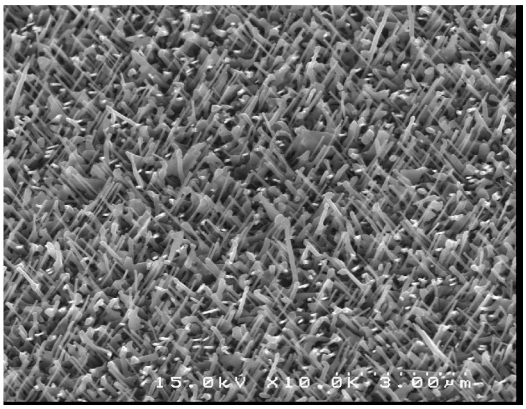

Fig 2. SEM image of the nanowires at 51º and 129º for the c-plane.

For each one of these substrates we have tested different oxidizing and reducing gases such as ethanol, NO_2 and C_6H_6. We have compared the responses and we have analysed which one of the substrates is the best for each of the target gases. We have also found out the optimal working conditions of our materials as a function of the orientation of the NWs on the substrates. First of all we have tested the response of our sensors to EtOH. As we can see from the images we have tried three different concentrations (500, 200 and 100ppm) of the target gas at three different temperatures. Fig. 3 show the response of theone of the sensors to repetitive cycles of 200 ppm of EtOH.

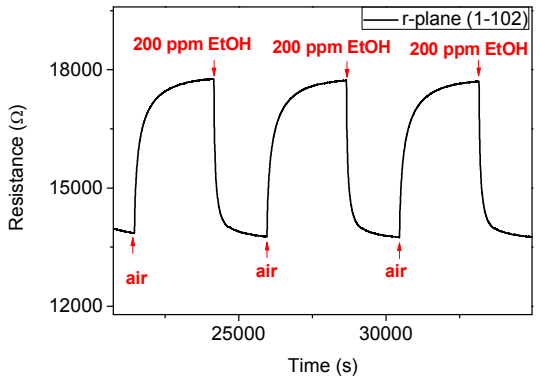

Fig 3. Response to EtOH of the r-plane sensor

After that, we tested our sensors to an oxidizing gas like NO_2, and C6H6. This time, we have tried again three different concentrations (100, 50 and 10 ppm) and the same temperatures as for EtOH (150, 200 and 250ºC). We can see from the fist image that our repeatability and stability are remarkable

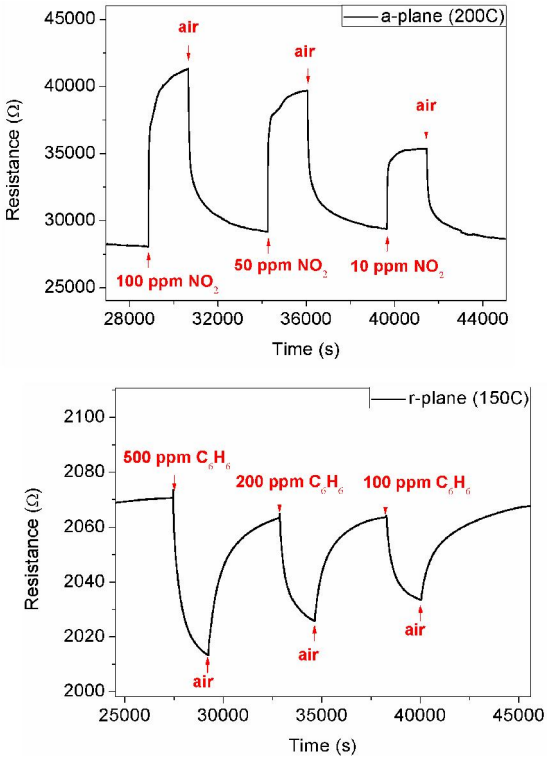

Fig 4. Response to NO2 (up) and C6H6 (down) of the a-plane and r-plane sensor

3. Conclusions

We have obtained ZnO NWs via the VLS method, grown over three different substrates with diverse crystallographic directions, resulting in the NWs oriented in three different ways. We have tested these three sensors to different oxidizing and reducing target gases such as EtOH, NO_2 and C_6H_6, and we have determined the optimum working conditions.

Influence of $PC_{70}BM$ and ICBA on the Efficiency in BHJ Organic Solar Cells with P3HT

J.G. Sánchez[a], V.S. Balderrama[a], J. Pallarés[a], J. Ferré-Borrull[a], M. Estrada[b] and L.F. Marsal[a]*

[a]Departament d'Enginyeria Electrònica, Elèctrica i Automàtica, Universitat Rovira i Virgili, Avda. Països Catalans 26, 43007 Tarragona, Spain.
[b]Sección de Electrónica del Estado Sólido, Depto. Ingeniería Eléctrica, CINVESTAV-IPN, Av. IPN No 2508, C.P. 07360, D.F., México

*Corresponding author: e-mail: lluis.marsal@urv.cat, Phone. +34 977 559 625, Fax: +34 977 559 605.

Abstract

Several bulk-heterojunction (BHJ) organic solar cells were fabricated with different blends for the active layer. The Poly(3-hexylthiophene) (P3HT) as electron donor material was the same in all cases. We focus in the electron acceptor material, using two similar fullerenes to study their effects on the power conversion efficiency (*PCE*) of the solar cells. Fullerenes used were [6, 6]-Phenyl C_{71} butyric acid methyl ester ($PC_{70}BM$) and 1',1'',4',4''-tetrahydro-di [1,4] methanonaphthaleno [5,6]fullerene-C_{60} (ICBA). The structures were ITO (120 nm) / PEDOT:PSS (40 nm) / P3HT:Fullerene (~200 nm) / Ca (25 nm) / Ag (100 nm) for all the samples. Furthermore, we fabricated several structures replacing the Ca layer for a poly [(9,9-bis(3'-(N,N-dimethylamino)propyl)-2,7-fluorene) -alt-2,7-(9,9–dioctylfluorene)] (PFN) film as surface modifier [1] between the blend and metallic cathode, with a thickness of 10 nm. The *PCE* in samples fabricated with $PC_{70}BM$ were higher than those for samples fabricated with ICBA. In the other hand, *PCE* and fill factor (*FF*) in samples fabricated with PFN were lower than those for samples fabricated without.

1. Introduction

Nowadays, the BHJ solar cells are too much interesting due to their low cost fabrication as well as their easy fabrication, simple device structure, promising applications, large-area devices and their possibility to flex, compared with traditional silicon solar cells. The improvement of the electrical and optical properties of the electron donor material, by modifying its chemical structure, has been the main approach to increase the *PCE* in BHJ solar cells. Many electron donor materials has been reported to enhance the *PCE* in BHJ solar cells, i.e., P3HT (3%) [2], PTB1 (5.2%) [3] and PTB7 (7.4 %) [4], to mention some of them. At present, research has been focused also to the study of new fullerene-type materials similar to $PC_{70}BM$, with different properties to improve the *PCE* of BHJ solar cells. One of these materials was the ICBA where *PCE* has been reported of 4-6 % [5-6].

2. Experimental and Discussion

Fig. 1 shows the BHJ organic solar cell structure that was made in this work. ITO were cleaned and exposed to UV during 15 minutes to eliminate organic material in their surface, afterwards, PEDOT:PSS was deposited on top of the ITO by spin-coating at 4500 rpm and was applied the annealing of 120°C during 20 min. Afterwards, a layer of blend (P3HT:Fullerene) was deposited on top. Two blends were fabricated in N_2 atmosphere, mixing in a bottle P3HT with two different fullerenes. In both cases the ratio was 1:1 (w/w), dissolving the blend in ortho-dichlorobenzene to obtain a final concentration of 20 mg ml^{-1} for the blend P3HT:$PC_{70}BM$ and 34 mg ml^{-1} for the blend P3HT:ICBA. Blends solutions were left stirring by 18 h and deposited by spin-coating at 600 rpm by 30 s for the blend P3HT:$PC_{70}BM$ and 800 rpm by 45 s for the blend P3HT:ICBA. Afterwards, the samples were left during 1 h under N_2 environment. Finally, the samples were transferred to a vacuum chamber, where 25 nm of Ca and 100 nm of Ag were thermally evaporated on the photoactive layer at $6x10^{-7}$ mbar. The active area in the devices was 9 mm^2. Other structures were made replacing the Ca by PFN. PFN was prepared dissolving 2 mg/ml in methanol and acetic acid with a ratio 1000:1 (v/v), respectively and left stirring during 18 h. PFN was deposited by spin-coating on top of the active layer before the Ag deposition at 3500 rpm by 1 min to get ~10 nm of thickness. The *J–V* curves of all fabricated structures under illumination at 1 sun (AM 1.5G spectrum) are shown in Fig. 2. Fig. 3 shows *J–V* curves of all structures under darkness. Table 1 shows the name of the samples and their structures. Samples A and B were fabricated with the same structure only the fullerene used was different, while the sample C was fabricated as sample A replacing the Ca layer by the PFN layer. The same case occurs with the sample D and B. Table 2 shows all the performance parameters for all

the structures A, B, C and D and their *PCE* were 3.19%, 2.94%, 1.75% and 1.39%, respectively. The performance parameters in the sample A were higher than that sample C. In sample B was the same case with sample D.

3. Conclusions

BHJ solar cells fabricated with P3HT:$PC_{70}BM$ had higher *PCE* compared with the samples fabricated with the P3HT:ICBA active layer. The devices fabricated with a PFN layer (C and D) had lower *PCE* than that samples without PFN (A and B). However, this is due to that the PFN layer is too thicker.

4. Future works

The use of PFN layer in BHJ solar cells as electron acceptor, the fullerene ratio in P3HT:ICBA blend solution and the Ca thickness must be optimized in order to improve the performance parameters on the photovoltaic devices.

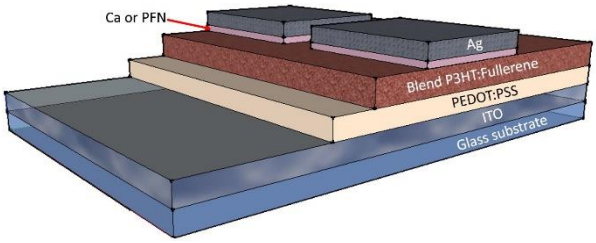

Fig. 1. Structure of BHJ solar cell with all layers ITO / PEDOT:PSS / P3HT:Fullerene/ Ca or PFN/ Ag.

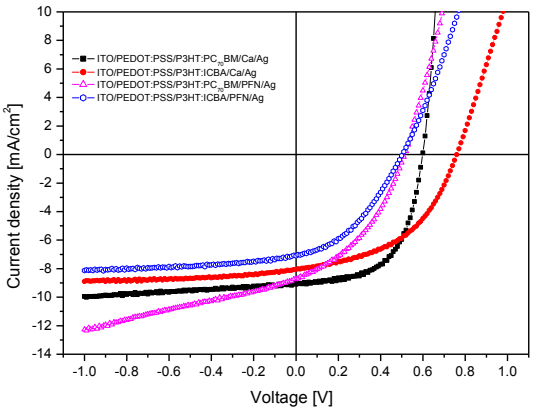

Fig. 2. *J–V* electrical characteristics of all structures under illumination at 1 sun (AM 1.5G spectrum).

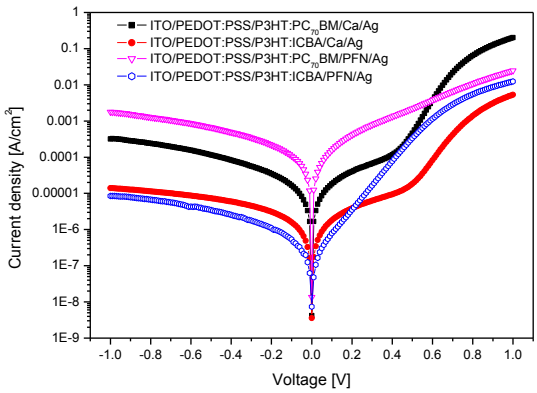

Fig. 3. *J–V* electrical characteristics under darkness of all structures manufactured.

Sample	Structure
A	ITO/PEDOT:PSS/P3HT:$PC_{70}BM$/Ca/Ag
B	ITO/PEDOT:PSS/P3HT:ICBA/Ca/Ag
C	ITO/PEDOT:PSS/P3HT:$PC_{70}BM$/PFN/Ag
D	ITO/PEDOT:PSS/P3HT:ICBA/PFN/Ag

Table 1. Structure of the samples.

Sample	V_{OC} [mV]	J_{SC} [mA/cm^2]	*FF* [%]	*PCE* [%]
A	600	9.10	58	3.19
B	760	8.05	48	2.94
C	510	8.73	40	1.75
D	450	7.10	39	1.39

Table 2. Performance parameters of the samples.

Acknowledgements

This work was supported by the Spanish Ministry of Economy and competitiveness (MINECO) under grant number, TEC2012-34397 and by Catalan authority under project AGAUR 2014 SGR 1344 and CONACYT Project 127978 in Mexico.

References

[1] F. Huang, "Novel electroluminescent conjugated poly-electrolytes based on polyfluorene", *Chem. Mater. 16*, pp. 708, 2004.

[2] V.S. Balderrama, "Correlation between P3HT inter-chain structure and Jsc of P3HT:$PC_{[70]}BM$ blends for solar cells", *Microelectronics Reliability 53*, pp. 560, 2013.

[3] V.S. Balderrama, "Degradation of electrical properties of PTB1:PCBM solar cells under different environments". *Solar Energy Materials and Solar Cells, 125*, pp. 155, 2014.

[4] Y. Liang, "For the Bright Future—Bulk Hetero-junction Polymer Solar Cells with Power Conversion Efficiency of 7.4%", *Adv. Mater., 22,* pp. E135, 2010.

[5] Z. Tan, "Solution-processed nickel acetate as hole collection layer for polymer solar cells", *Phys. Chem. Chem. Phys., 14*, pp. 14217, 2012.

[6] S. Singh, "Ultrafast transient spectroscopy of nano-domains of polymer/fullerene blend for organic photovoltaic applications", *Journal of Applied Physics 112*, pp. 123505, 2012.

Polydimethylsiloxane micropatterned substrates for bio-applications

A. Slota, M. Baranowska, P. Jacob, P. Formentín, L.F. Marsal

Departament d'Enginyeria Electrònica, Elèctrica i Automàtica, Universitat Rovira i Virgili
Avda. Països Catalans 26, 43007 Tarragona, Spain
lluis.marsal@urv.cat

Abstract

In this study we present the fabrication process for a biocompatible double-layer polydimethylsiloxane stamps with various surface morphologies. These materials are intended to be used as cell culture substrates in order to investigate the influence of surface topography on cell adhesion, growth and proliferation.

1. Introduction

As it has been already proven in many studies, an understanding and control over interactions between biomolecules and surfaces is the key to many biomedical applications: from cell-based sensors and chip devices to tissue-engineered artificial organs [1, 2]. In their natural tissue environment cells are constantly subjected to a multitude of chemical and physical signals coming from the contact with other cells and with the extra-cellular matrix components. These signals determine cells behavior influencing their adhesion, growth and differentiation. Studying biointerfacial interactions in vitro has become possible by using micro- and nanofabrication techniques to construct materials of various topographical and chemical cues mimicking native cell microenvironment [3]. Despite the large number of papers published in this area, general tendencies in cell-material interactions are yet difficult to establish due to the differences in cell types, material chemistry and the geometrical characteristics of the surface features.

Polydimethylsiloxane (PDMS) is a silicon-based polymer, generally considered as inert and non-toxic and widely used in pharmaceutical and cosmetics industries. Apart from biocompatibility, other properties of PDMS, like high solvent and temperature resistance, high gas permeability, adjustable elasticity and the ability to be formed into complicated shapes on micro- and nanoscale, make it a favorable biomaterial for tissue engineering application [4].

In the present study we describe the preparation of PDMS patterned substrates with different topographies by replication from porous alumina and silicon templates.

2. Experimental

The alumina templates with ordered pores structure were obtained by two-step anodization process in 1 wt% phosphoric acid solution followed by pore-widening treatment. Macroporous silicon samples were prepared by anodizing Si substrates in hydrofluoric acid-dimethylformamide electrolyte (1:10 v/v) at 5 $mA \cdot cm^{-2}$. Photolithography and chemical etching in 8% solution of tetramethylammonium hydroxide were used to produce silicon templates with inverted pyramid pattern.

Polydimethylsiloxane replicas were fabricated as two-layer stamps: a thin layer of high elastic modulus PDMS ("hard PDMS") for the improved pattern transfer of nanoscale features and a thicker layer of low elastic modulus PDMS to provide a flexible support [5]. To obtain h-PDMS layer, 3.4 g of vinyl PDMS prepolymer (VDT-731, Gelest Corp.) was mixed with 18 µl of platinum catalyst, 12 mg of modulator and 1 g of PDMS hydrosilane prepolymer (HMS-301, Gelest Corp.) and subsequently degassed under vacuum. The mixture was spin-coated onto Si or alumina template and thermally cured in an oven at 60 ºC for 20 minutes. The second PDMS layer was prepared by mixing "Sylgard 184" (Dow Corning) prepolymer and curing agent in 10:1 ratio, degassing and pouring on the template with h-PDMS layer. The composite was then placed in an oven and cured at 60 ºC for 2 hours. After cooling down, the PDMS stamp was carefully peeled off from the template.

To compare the structures of alumina and silicon templates with the resulting PDMS replicas, the samples were characterized by environmental scanning electron microscope (ESEM).

3. Results and discussion

The total thickness of fabricated PDMS stamps was about 3 mm with the h-PDMS layer of 65 µm. The ESEM images (Fig. 1) reveal a successful replication of the master structures on the polymeric substrate. The overall geometry of the hard templates - in terms of ordering and shape - is well preserved with no significant pattern deformations (collapse, buckling, edge rounding) typical for low elastic modulus PDMS [6]. However, some differences in structural dimensions between

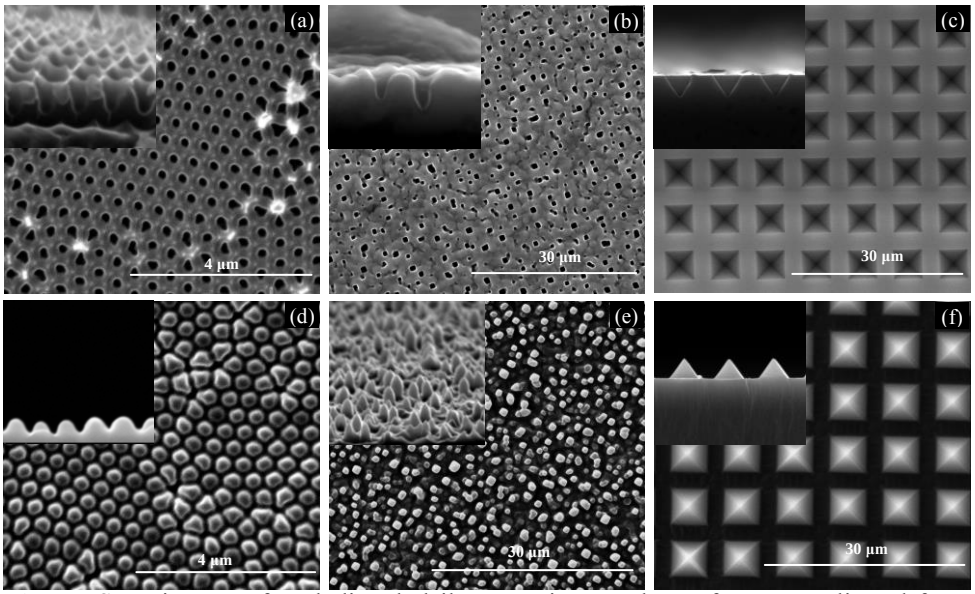

Fig. 1 ESEM images of polydimethylsiloxane micro- and nanofeatures replicated from alumina and silicon templates.

templates and polymer replicas can be found. The pore diameter of the nanoporous anodic alumina is in the 160-180 nm range whereas the diameter of PDMS nanopillars is almost two times larger (310-340 nm) although with the same interpore distance of ca. 450 nm. Moreover, the nanopillars are about 100 nm shorter than the corresponding length of alumina pores (370 nm) which suggests that the pore filling by PDMS liquid pre-polymer could be incomplete [7]. In the case of macroporous silicon template and the resulting PDMS replica the general tendency to increase the diameter and decrease the length of the pillars can also be observed, however the changes seem to be less significant than for the nanoscale features. For the silicon pores of 0.6-1 µm diameter and 1-2 µm length the corresponding PDMS pillars are about 1-1.5 µm wide and 1.5-1.8 µm tall. The exact differences are yet difficult to define because of the pattern non-uniformity and random ordering. The smallest size variations were found in the case of PDMS pyramids replicated from lithography patterned silicon. The lateral pyramid size is about 5 µm, the height is 3.8 µm and the inter-pyramid distance is 8 µm which is in good agreement with the dimensions of the silicon master geometry.

4. Conclusions

A double-layer polydimethylsiloxane stamps with different topographies were fabricated via replica molding from porous alumina and silicon templates. Combing high and low elastic modulus PDMS allowed to obtain stable materials with no significant pattern deformation. The most accurate transfer of template geometry was achieved in the case of macroscale features (pyramids). The replicated nano-features exhibit some size variations (increased diameter and decreased length) but the overall geometry is well preserved. The effect of fabricated micro- and nano-structured surfaces on cell behaviour will be investigated in the future.

5. Acknowledgements

This work was supported by the Spanish Ministry of Economy and Competitiveness (MINECO) under grant number TEC2012-34397 and by Catalan Government under project AGAUR 2014-SGR-1344.

References

[1] P. Koegler, A. Clayton, H. Thissen, G.N.C. Santos, P. Kingshott, The influence of nanostructured materials on biointerfacial interactions, Adv. Drug Deliv. Rev. 64 (2012), 1820–1839.

[2] M. Nikkhah, F. Edalat, S. Manoucheri, A. Khademhosseini, Engineering microscale topographies to control the cell-substrate interface, Biomaterials 33 (2012), 5230-5246.

[3] T. Betancourt, L. Brannon-Peppas, Micro- and nanofabrication methods in nanotechnological medical and pharmaceutical devices, Int. J. Nanomedicine, 1 (2006), 483-495.

[4] B. Ratner, A. Hoffman, F. Schoen, J. Lemons, Biomaterials Science (Third Edition): An Introduction to Materials in Medicine, Academic Press, 2012.

[5] T.W. Odom, J.C. Love, D.B. Wolfe, K.E. Paul, G.M. Whitesides, Improved pattern transfer in soft lithography using composite stamps, Langmuir 18 (2002), 5314-5320.

[6] C. Y. Hui, A. Jagota, Y. Y. Lin, E. J. Kramer, Constraints on microcontact printing imposed by stamp deformation, Langmuir 18 (2002), 1394-1407.

[7] C. Con, B. Cui, Effect of mold treatment by solvent on PDMS molding into nanoholes, Nanoscale Res. Lett. 8 (2013), 394.

Study of P3HT:PCBM blend nanopillars prepared from nanoporous alumina for solar cells applications

C. Stenta, P.L. Han, J. Ferré-Borrull, J. Pallarès, L.F. Marsal

Departament d'Enginyeria Electrònica, Elèctrica i Automàtica, Universitat Rovira i Virgili
Avda Països Catalans 26, 43007 Tarragona (Spain); E-mail: lluis.marsal@urv.cat; Tel: (34) 977 55 96 25

Abstract

The active layer of an organic solar cell is molded into an ordered nanopillar array to improve exciton dissociation and charge collection, thus improving the cell efficiency. To achieve a nanopillar morphology, poly(3-hexylthiophene) (P3HT) and fullerene derivative Phenyl-C_{60}-butyric acid methyl ester (PCBM) blends are molded by means of nanoimprinting lithography with a nanoporous aluminium oxide template.

1. Introduction

Recent progress in Organic Solar Cells (OSC) has proven this technology a valid competitor to the more stablished inorganic wafer based technology.

One of the key issues in improving the efficiency of OSC has been the morphology control of the donor-acceptor junction. An ideal structure should both ensure diminish recombination effects and provide an efficient charge transport between layers. Therefore, large dissociative interface between the donor and acceptor materials, as well as between the active layer and the electrode, is crucial to an improved performance of the OSC.

Here we study the influence of the nanostructures of P3HT and PCBM blends in the cell photoelectric conversion efficiency. Different morpholgies are studied by nanostructuring the active layer with .different types of aluminium oxide templates..

2. Experimental

Aluminium plates were first electrochemically polished using an electrolyte solution of ethanol (EtOH) and perchloric acid ($HClO_4$) (4:1) in order to obtain low surface roughness (~3nm) [1] of the plates. When a voltage is applied during the polishing, the aluminium is oxidized but no oxide is formed due to the chemical conditions of the electrolyte used. The electropolishing is carried out by applying 20 V for 2 min under a constant stirring rate.

To produce the nanoporous anodized alumina templates (NAATs) the two-step anodization technique is used, which is described elsewhere [2]. Figure 1 summarize the two-step anodization technique.

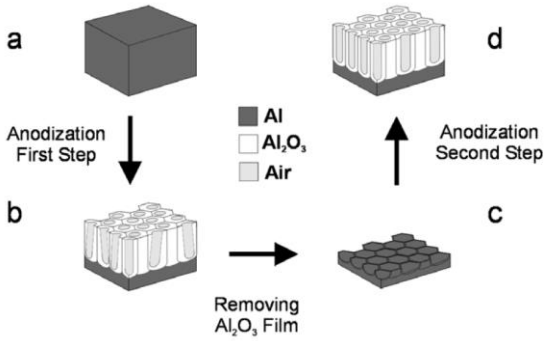

Fig.1. Schematic overview of the two-step anodization process. A) Electropolished aluminium foils; b) Anodic Alumina Templated with disordered pores on top and ordered pores at the bottom; c) Ordered patterned Al substrate and d) Nanoporous Anodic Alumina Templates with hexagonally ordered pores. [2]

Alumina templates with different pore lengths have been produced in order to study the characteristics and the structure of the blend nanopillars that can be obtained through the nanoimprint process.

To obtain different pore lengths the charge applied during the anodization has been varied.

Before nanoimprinting, the alumina templates were first modified by Poly(dimethylsiloxane) (PDMS) to reduce the surface energy of the templates. PDMS has been used because of its properties of special interest like the thermal stability (melting point T_m, 217.8-236K) and excellent release properties [3].

Thermal nanoimprinting with the alumina mold was developed to fabricate nanopillars in the P3HT:PCBM blend layer.

The blend layer of P3HT:PCBM was spin coated on a substrate of PEDOT:PSS.

Nanoporous anodic alumina template are sandwiched between the polymer substrate and the metal layer used for transferring the pressure on the desired area as shown in Figure 3.

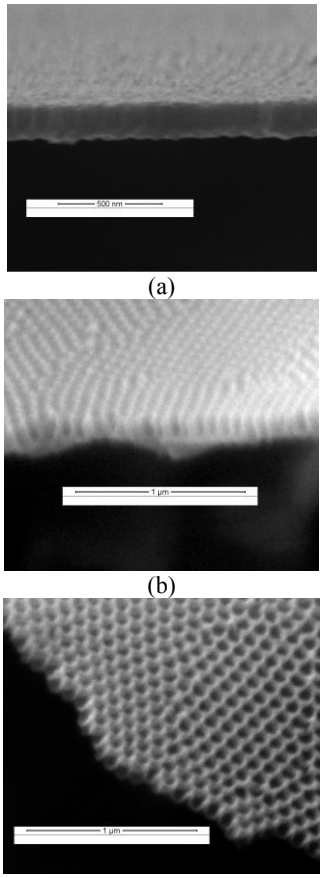

Fig.2 Cross section SEM images of AAO templates produced through the two-step anodization process with (a) and (b) Q=2,53 C and (c) 1,75 C.

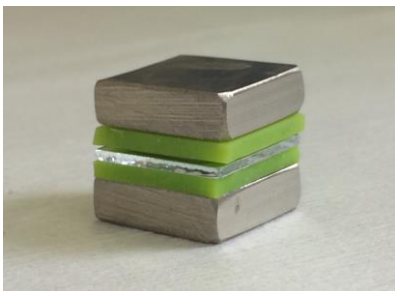

Fig.3 Nanoimprinting architecture used to produce the polymer nanopillars from alumina molds.

Then, the nanoimprinted P3HT:PCBM nanopillars were used to make bulk heterojunction solar cells by depositing calcium and silver on top of the pillars through Physical Vapour Deposition (PVD).

3. Results

NAAT's of high density nanopores with different pore lengths have been successfully fabricated by the two-step anodization process.

By means of nanoimprinting, polymer nanopillars have been fabricated showing how this technique provided a way to control the interdigitized heterojunction morphology.

Nanopillars of P3HT:PCBM blend layer have been observed.

The PVD of Ca and Ag on the nanopillars leads to promising functioning solar devices that open the way to further studies and investigation on the technology

4. Conclusions

We have presented a cost-effective method that combines electrochemical process and thermal nanoimprinting to produce nanopillars structures for solar cells applications.

Keys parameters to better understanding these innovative structures are the morphology control of blend nanopillars and the deposition control of the metal layer. Thus, in order to optimize the nanopillars fabrication process and to complete understand the operation of these structured solar cells, further characterization, both structural and electronic, is required. Future research work will also include thermal annealing studies on the nanostructured solar devices as the annealing could improve the performance of the organic solar cells [4].

Acknowledgements

This work was supported by the Spanish Ministry of Economy and Competitiveness (MINECO) under grant no. TEC2012-34397 and by the Generalitat of Catalunya under grant no. 2014-SGR-1344.

References

[1] Aryal, Mukti, et al. "Imprinted large-scale high density polymer nanopillars for organic solar cells." *Journal of Vacuum Science & Technology B* 26.6 (2008): 2562-2566.

[2] Alejandro, Abel Santos. Structural Engineering of Nanoporous Anodic Alumina and Applications: Doctoral Thesis. Universitat Rovira I Virgili, 2011.

[3] Kuo, ALEX CM. "Poly (dimethylsiloxane)." *Polymer data handbook* (1999): 411.

[4] Yang, Xiaohan, and Ashraf Uddin. "Effect of thermal annealing on P3HT: PCBM bulk-heterojunction organic solar cells: A critical review." *Renewable and Sustainable Energy Reviews* 30 (2014): 324-336.

Gas sensing properties of nanostructured mixed oxide film prepared by anodizing Zr-W alloy through the alumina nanopores

R.M. Vázquez[1*], R. Calavia[1], F. Gispert-Guirado[1], E. Llobet[1], J. Hubalek[2], A. Mozalev[2]

[1]MINOS-EMaS Universitat Rovira I Virgili, Tarragona, SPAIN
[2]Department of Microelectronics, Brno University of Technology, Brno, CZECH REPUBLIC
rosamaria.vazquez@urv.cat

Abstract

Nanostructured Zr-W mixed oxide film was prepared via anodizing a sputter-deposited Zr-W alloy layer through nanopores in an anodic alumina layer superimposed on the alloy. The morphology, structure and chemical composition of the film were examined by SEM and XRD. Test sensor employing the ZrO_2-WO_3 mixed oxide film as active layer was fabricated and utilized for detecting H_2 at different concentrations (100-1000 ppm) at temperatures up to 300°C. The sensor was fast and highly responsive to hydrogen. The findings are of importance for improving chemical and structural stability of the nanostructured tungsten-oxide-based films and selectivity of gas sensors employing the films.

1. Introduction

Crystalline nanostructured oxides on refractory metals are of growing interest as active layers for chemical sensors. In this niche, tungsten trioxide has proved to be effective in detecting a wide range of atmospheric pollutants. Among the preparation techniques, anodizing of sputter-deposited tungsten layers has the advantage of tailored morphology and full compatibility with Si microtechnology. The major problem with the anodically synthesized WO_3 films is their chemical instability, which may cause distraction of the nanosized character already during film growth. As recently reported [1], field-assisted mixing of a metal oxide with dissimilar oxide at the nanoscale may restrain and stabilize the growth of the first oxide phase and improve substantially the post-formed properties of the mixed oxide film.

In the present work, we describe the process for forming self-organized nanostructured tungsten oxide regularly mixed with zirconium oxide resulting from porous-alumina-assisted anodizing of a layer of Zr-W alloy sputter-deposited onto oxide-coated silicon wafer and explore gas sensing properties of this mixed oxide film.

2. Experimental

The initial sample was prepared by sequential magnetron sputter-deposition onto a 100-mm Si wafer of a layer of Zr-50at.%W alloy followed by a layer of Al 99.99%. The sample pieces were anodized in an aqueous acid electrolyte and then reanodized to a more anodic voltage, as described conceptually in our previous work on individual W metal [2]. This resulted in the initial growth of a porous anodic alumina film, followed by pore-assisted formation of anodic oxide on the Zr-W underlayer, as shown schematically in Fig. 1. Post anodizing treatment included annealing at 600-800°C to examine crystallization and phase transition effects in the mixed oxides and open-circuit dissolution of the alumina overlayer. The morphology and crystalline structure of the film formed was examined by X-ray diffraction (XRD) and scanning electron microscopy (SEM).

A fully automated experimental set-up was employed for performing gas sensing tests. The desired concentration of test gas was obtained from the calibrated gas cylinders by means of mass flow controllers commanded from the LabView environment. The sample with a pair of Pt interdigitated microelectrodes on top was bonded to a ceramic hotplate allowing the operating temperatures up to 300°C (Fig. 1f). The in-plain resistance of the film annealed at 700°C was monitored in the presence of either synthetic air or hydrogen gas at various temperatures and concentrations.

3. Results and discussion

Fig. 2 shows typical SEM views of the anodic film formed as outlined in Fig. 1. The film consists of two parts: a lower, relatively compact layer and an upper layer which is an array of upright-standing nanosized columns anchored to the lower layer. From the XRD analysis, the film is composed of monoclinic WO_3 and orthorhombic ZrO_2. As the film composition is well stabilized, the morphology remains unaffected in the solutions selectively dissolving alumina.

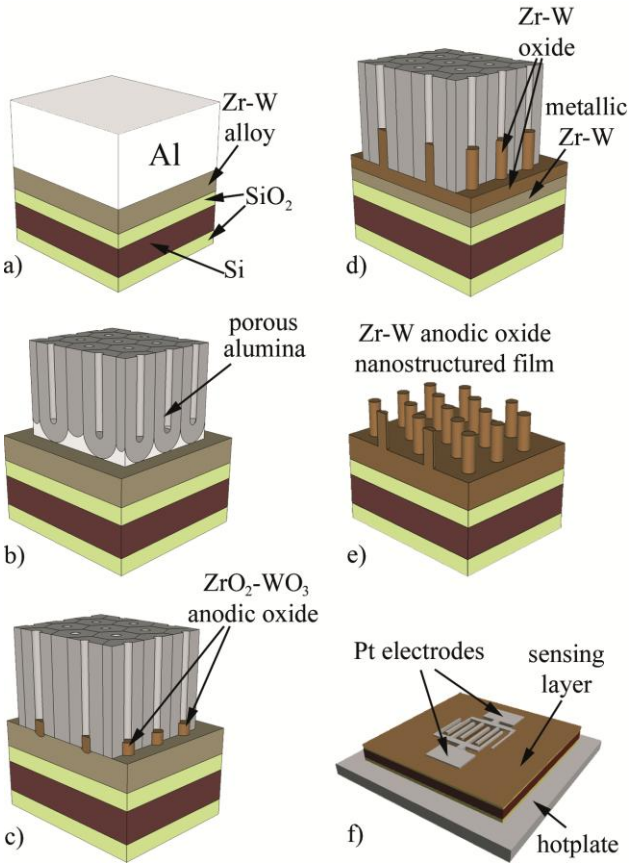

Figure 1. Schematic diagram showing the process for growing Zr-W mixed oxide nanostructured film on an SiO_2/Si substrate: a) sputter deposition of Al/Zr-W layer, b) formation of porous anodic alumina, c) anodizing the Zr-W alloy layer, d) reanodizing the Zr-W alloy layer through the alumina nanopores, e) dissolution of the porous alumina overlayer and annealing the film at 700ºC, f) preparation of test sensor employing the Zr-W mixed oxide active film.

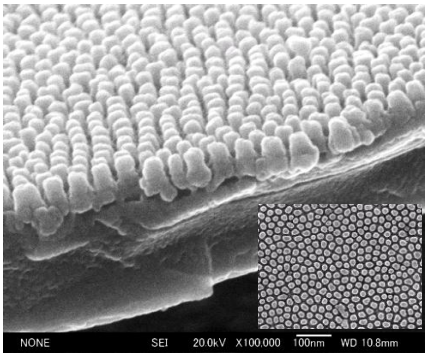

Figure 2. SEM views of the anodized/reanodized Zr-50at.%W layers onto an oxide-coated Si wafer. The insert shows an SEM surface view of the film.

As an example, Fig. 3 and 4 show the behavior of the sensor resistance, temperature-dependent sensor response, response time and recovery time in the presence of 1000 ppm H_2. The film is highly responsive to hydrogen with response and recovery times as short as 9 seconds in the range of 200-300ºC, with the fully reversible film resistance, which characterizes the Zr-W mixed oxide nanostructured film as one of the fastest-responding among the metal-oxide sensors. The achievement is due to the construction of a three-dimensional architecture of the nanocrystalline zirconium-tungsten oxide film, with the substantially increased surface-to-volume ratio, which effectively speeds up both the adsorption and diffusion processes at the film surface and in the oxide volume.

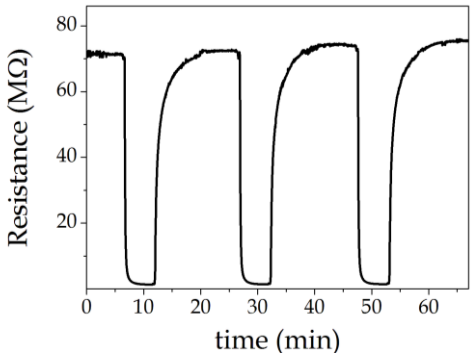

Figure 3. Resistance response to 1000 ppm H_2 of the Zr-W mixed oxide film at 225ºC.

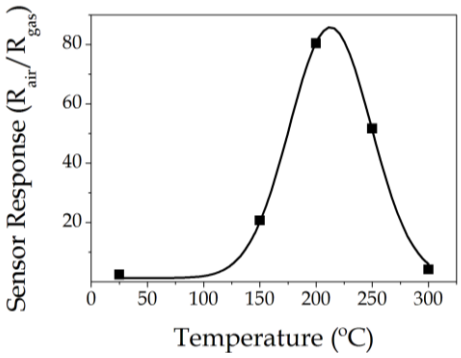

Figure 4. Sensor-response value of the nanostructured Zr-W mixed oxide film in the presence of 1000 ppm of hydrogen at various operating temperatures.

References

[1] R. M. Vázquez, R. Calavia, E. Llobet, F. Guirado, J. Hubálek, A. Mozalev, "The Growth and Gas Sensing Properties of Mixed Oxide Nanocomposite Thin Film Derived from Anodically Oxidized Al/Ti Metal Layers", in *Procedia Engineering Eurosensor 2012 Conference*, Kraków, September 9-12, 2012, pp. 833-836.

[2] A. Mozalev, V. Khatko, C. Bittencourt, A. W. Hassel, G, Gorokh, E. Llobet, X. Correig, "Nanostructured Columnlike Tungsten Oxide Film by Anodizing Al/W/Ti Layers on Si", *Chem. Mater.*, vol. 20, pp. 6482-6493, 2008.

Fabrication and characterization of Different solid state substrates based on Tungsten Trioxide for Laser Desorption Ionization Mass Spectrometry applications

Vilalta[1,2], D.; Calavia[1,2], R; Yanes[1,2,3], O; Canela[3], N, Correig[1,2], X.

[1]Dept. Enginyeria Electrònica, Universitat Rovira i Virgili, Tarragona, Spain

[2]Metabolomics Platform, CIBERDEM (CIBER de Diabetes y Enfermedades Metabólicas Asociadas), Spain

[3]Centre for Omic sciences, URV, Reus, Spain

Abstract

The analysis of metabolites with MALDI-MS is not straightforward because the organic matrix used masks the ions peaks of metabolites. To overcome this limitation, solid-state substrates based on nanoporous silicon (i.e DIOS and NIMS), carbon derivatives or metal nanoparticles, has been used for Laser Desorbtion Ionization (LDI) applications. In this study, three different solid-state substrates are fabricated and characterized. The first one is the NIMS standard substrate, the second is the NIMS with added WO_3 nanoparticles and the third one is a WO_3 substrate obtained by an anodic process employing tartaric acid. To measure the sensibility and selectivity of these substrates, five different mixtures of standard compounds and human urine samples had ben spotted onto the surfaces. Two of these mixtures are based in lipids standard compounds, and the other three are mixtures based in aqueous standard compounds.

1. Introduction

The Matrix Assisted Laser Desorption Ionization (MALDI) is an analytic technique developed in the 80's [1]. Since then, it has been used for the detection of macromolecules (peptides, proteins, lipids, etc). The organic matrix for the ionization of the sample generates many ion peaks at low mass spectra (< 1000 Da) that makes impossible to use in metabolomics. For this reason, different solid-state substrates, with little interference in the low weight mass region, have appeared during the last years.

The new created substrates need to fulfill some specific properties to be used in the LDI techniques [2]. These new substrates must be chemically stable and their surfaces can be easily functionalized. They must have a high melting point, in order to minimize interference of the surface, a low thermal capacity combined with high thermal and electrical conductivity, a high absorption coefficient at the laser wavelength (355 μm) and a high ratio between active area and volume to obtain high sensitivity.

One of these new substrates is the Desorption Ionization On porous Silicon (DIOS) [3], created by Dr. G. Siuzdak et al. in 1999; the fabrication process consist in silicon anodizing with hydrofluoric acid (HF) in a galvanostatic mode. During the anodizing process the surface is irradiated with a white light. Using DIOS substrate in LDI applications is possible to detect compounds in the femto Mol range [4]. The DIOS substrates, due to their stability problems evolved to Nanostructure Initiator Mass Spectrometry (NIMS) [5], created by Dr. G. Siuzdak et al. in 2007. This substrate is fabricated anodizing silicon (also with HF acid). A perfluorinated compound layer (Heptadecafluoro-1,1,2,2-tetrahydrodecyl) dimethylchlorosilane , called *initiator compound* was applied on the top of the nanostructured material, and gives hydrophobic properties to the surface. This compound facilitates the sample protonation due to the Fluor protons given to the surface. With NIMS substrates is possible to detect compounds in femto and atto Mol range [6].

Another type of solid-state substrate used in LDI applications is based in carbon derivatives, i.e. Carbon Nanotubes (CNT). Using CNT is possible to detect compounds in nano Mol range [7]. Another material based with carbon is the graphite [8]. It is deposited on the commercial MALDI plates or on the silicon wafer before the sample deposition. But carbon based materials produce an important background noise, which makes the identifications of low-intensity peaks extremely difficult.

Other solid-state substrates, based on nanoparticles of different metals (Au, Ag, etc.) or metal-oxides (WO3, ZnO, etc.) deposited on silicon, have been employed during last years in LDI experiments. This kind of surfaces are called Surface Assisted Laser Desorption Ionization (SALDI) [9].

The sensitivities that we can achieve with SALDI

substrates depend on the nanostructuring degree of them. It has been reported [10] that we can detect compounds in concentrations as low as femto Mol range with gold nanoparticles [11].
WO_3 and the TiO_2 are two metal-oxides that exhibit excellent properties that makes them ideal for LDI applications [2]. With the WO_3 and TiO_2, is possible detect compounds in the pico Mol range [12]. In order to obtain the WO_3, in the literature, there has been reported several processes.
In this study we have fabricated and characterized two different WO_3 substrates for Laser Desorption Ionization Mass Spectrometry. The first WO3 substrate was fabricated anodizing a W/Ti metal bilayer, deposited previously by sputtering, followed by a galvanostatic etching process [13]. The second is the NIMS standard substrate adding WO_3 nanoparticles (NIMS+NP-WO_3). The standard NIMS has been used as a reference substrate for comparing.
All of these surfaces are tested with different standards mixtures and human urine samples.

2. Methodology

2.1. Nanostructured substrates fabrication

2.1.1. NIMS

The NIMS substrates were fabricated according with the process reported by H. Woo et al. [14]. The p-type silicon wafers were cut into 35 x 35 mm squares and after, the chips were cleaned through submersion in Piranha solution (2:1 H2SO4:H2O2) for 30 min. Then the chips were cleaned with deionized water and ethanol, and were dried with high-purity nitrogen gas. The etching process has been performed in a Teflon chamber in two steps. In the first step, 25 % of hydrofluoric acid in ethanol was dumped and we waited 10 min before to apply the current. In the second step, we applied the current of 0.3 A for 30 min. The etching chips were cleaned with ethanol and dried at 100 ºC for 10 min. Then, the chips were coated with ~ 75 μL of the *initiator* compound using an airbrushing deposition system, during 0,78 seconds with 2 bar of nitrogen pressure.

2.1.2. NIMS + NP-WO_3 nanoparticles

The NIMS fabrication process was reported in the section 2.1.1. NIMS. After the porosification process of the silicon, the WO3 nanoparticles were deposited on the chips by a reactive sputtering-deposition RF Magnetron with 100 W of power for 15 seconds, using a 99.995% tungsten purity target. Then, the chips were coated with ~ 75 μL of *initiator* compound using an airbrushing deposition system, during 0,78 seconds with 2 bar of nitrogen pressure.

2.1.3. Anodized WO3 layer on silicon

The procedure to create this substrate was divided in two steps. In the first step a layer of 50 nm of Ti was deposited with a RF power of 200 W. After that, a W layer of 200 nm was deposited with an RF power of 200 W. The second step is the etching process. This process took place in a Teflon camber with 0.4 M Tartaric acid aqueous solution under 4.5 mA/cm^2 for 18 min [13].

2.2. Characterization of the created substrates

The Environmental Scanning Electron Microscope (ESEM) FEI Quanta 600 was used to characterize all of the fabricated substrates
To characterize the surface reaction when the laser beam impacts on it, we used the X-Ray Diffraction (RDX) equipment model Siemens EM-10110BU D5000.

2.3. Sample preparation and deposition

2.3.1. Sample preparation

For testing the different solid-state substrates created, we prepared five different standard mixtures. The two first mixtures used are phospholipids mixtures, and the other three mixtures are aqueous standard compounds (see **Table 1**).
The standard compounds were diluted with deionized H_2O and methanol (v:v) at the concentration of 1 mg/ml. After the individual compound dilutions, we mixed it in five different mixtures. Doing this process we dilute a 10 factor these compounds. The urine samples were diluted in deionized H2O at a factor of 1:10.

2.3.2. Sample deposition

0,5-1 μl of every sample was deposited manually over every surface. For avoiding the sample crystallization on the surface, after 1-2 seconds of the deposition process, the sample was absorbed another time.

2.4. Sample analysis

The equipment used for the analysis was the Bruker Ultraflex extreme MALDI-TOF spectrometer. As a substrate support we used a commercial MALDI plate previously modified with a 50 μm recesses.
The spectrometer configuration used was a reflection mode oriented to detect in the low mass range (100 - 1500 Da) in positive and negative ionization mode.
The obtained spectra are externally calibrated with one mixture of standard compounds.

3. Results and Discussion

3.1. Standard Response

The five different standard compound mixtures described before (see **Table 1)** were tested to characterize the new surfaces.
In order to estimate the substrate homogeneity and the deposition process repetitively, every sample has been deposited in three spots and the averaged signal to noise ratio (SN) of every sample as well as the standard deviation (SD) has been calculated for every sample.
Figure 1 shows the SN and SD for every compound and surface. The phospholipids detection is better with the NIMS surface (or in the NIMS with WO_3 nanoparticles) than in the WO_3 based ones. In the surface NIMS + NP-

WO_3 we can detect the lipids compounds with a few rises in their SN in front of NIMS substrate.
The best surface for aqueous standards detection is the WO_3 etched by Tartaric acid, because in general the SN is higher than with NIMS based surfaces and using this surface we can detect some standard compounds that are impossible to detect with the NIMS based surfaces.

3.2. Urine Response

Measuring the urine samples we observed that the three different surfaces are able to detect different ions, so being complementary between them. In **Figure 2** we can see the urine spectra measured for every substrate. In the NIMS substrate we can detect 123 sample peaks, in the NIMS+NP-WO_3 195 sample peaks, with WO_3 Tartaric acid etching 142 sample peaks, and in the three surfaces in total 244 different sample peaks. In order to identify the metabolites detected we used their exact mass to interrogate the METLIN DATABASE.

3.3. Background Noise

To analyze the background noise, we employed the same laser parameters used in the sample; we shot in a region without sample and we obtained a surface reference spectrum. The peaks of this spectrum will be subtracted from the sample spectra. In the **Figure 3** we can observe the substrate spectra obtained with the three different surfaces analyzed.
Between the NIMS and NIMS with Nanoparticles, the background noise is similar, but a few more peaks can be observed in the latter surface. The surface of WO_3 etched by Tartaric acid reduces drastically this background noise in one order of magnitude. This example is reported in the **Figure 3**. In the surface etched by Tartaric acid have some peaks in the mass range from 80 to 1400 Da from the Tungsten, and these peaks difficult the correct compounds detection in this mass range, but in the NIMS case the more concentration of the surface peaks are in the mass range from 400 to 600 Da, and it makes difficult the correct compound detection in this mass range.

4. Conclusions

WO_3 surfaces exhibits a much more elevated sensitivity towards the aqueous metabolites that the NIMS based surfaces. However, the WO_3 based surfaces are not capable to detect lipids. Interestingly, NIMS+NP-WO3 improves the sensitivity of aqueous compounds compared NIMS, keeping the good sensitivity of lipid compounds.

The background noise of WO3 surfaces in the low mass region is excellent, although in the mid range appears some intense ions related with tungsten alloys.

References

1. Karas, M. and F. Hillenkamp, *LASER DESORPTION IONIZATION OF PROTEINS WITH MOLECULAR MASSES EXCEEDING 10000 DALTONS.* Analytical Chemistry, 1988. **60**(20): p. 2299-2301.
2. Okuno, S., et al., *Requirements for laser-induced desorption/ionization on submicrometer structures.* Analytical Chemistry, 2005. **77**(16): p. 5364-5369.
3. Wei, J., J.M. Buriak, and G. Siuzdak, *Desorption-ionization mass spectrometry on porous silicon.* Nature, 1999. **399**(6733): p. 243-246.
4. Laiko, V.V., et al., *Atmospheric pressure laser desorption/ionization on porous silicon.* Rapid Communications in Mass Spectrometry, 2002. **16**(18): p. 1737-1742.
5. Northen, T.R., et al., *Clathrate nanostructures for mass spectrometry.* Nature, 2007. **449**(7165): p. 1033-U3.
6. Patti, G.J., et al., *Detection of Carbohydrates and Steroids by Cation-Enhanced Nanostructure-Initiator Mass Spectrometry (NIMS) for Biofluid Analysis and Tissue Imaging.* Analytical Chemistry, 2010. **82**(1): p. 121-128.
7. Ren, S.F. and Y.L. Guo, *Oxidized carbon nanotubes as matrix for matrix-assisted laser desorption/ionization time-of-flight mass spectrometric analysis of biomolecules.* Rapid Communications in Mass Spectrometry, 2005. **19**(2): p. 255-260.
8. Sunner, J., E. Dratz, and Y.C. Chen, *GRAPHITE SURFACE ASSISTED LASER DESORPTION/IONIZATION TIME-OF-FLIGHT MASS-SPECTROMETRY OF PEPTIDES AND PROTEINS FROM LIQUID SOLUTIONS.* Analytical Chemistry, 1995. **67**(23): p. 4335-4342.
9. Shrivas, K. and H.-F. Wu, *Applications of silver nanoparticles capped with different functional groups as the matrix and affinity probes in surface-assisted laser desorption/ionization time-of-flight and atmospheric pressure matrix-assisted laser desorption/ionization ion trap mass spectrometry for rapid analysis of sulfur drugs and biothiols in human urine.* Rapid Communications in Mass Spectrometry, 2008. **22**(18): p. 2863-2872.
10. Kawasaki, H., et al., *Layer-by-layer self-assembled mutilayer films of gold nanoparticles for surface-assisted laser desorption/ionization mass spectrometry.* Analytical Chemistry, 2008. **80**(19): p. 7524-7533.
11. Su, C.-L. and W.-L. Tseng, *Gold nanoparticles as assisted matrix for determining neutral small carbohydrates through laser desorption/ionization time-of-flight mass spectrometry.* Analytical Chemistry, 2007. **79**(4): p. 1626-1633.
12. Yuan, M.J., et al., *Preparation of highly ordered mesoporous WO(3)-TiO(2) as matrix in matrix-assisted laser desorption/ionization mass spectrometry.* Microporous and Mesoporous Materials, 2005. **78**(1): p. 37-41.
13. Zeng, J., et al., *NO2-sensing properties of porous WO3 gas sensor based on anodized sputtered tungsten thin film.* Sensors and Actuators B-Chemical, 2012. **161**(1): p. 447-452.
14. Woo, H., et al., *Nanostructure-initiator mass spectrometry: a protocol for preparing and applying NIMS surfaces for high-sensitivity mass analysis.* Nature Protocols, 2008. **3**(8): p. 1341-1349.

Tables

Mixture for calibrating	Lipid 1	Lipid 2	Aqueous 1	Aqueous 2	Aqueous 3
1,2-dioleoyl-sn-glycero-3-phosphocholine (18:1 (Δ9-Cis))	1,2-dioleoyl-sn-glycero-3-phosphocholine (18:1 (Δ9-Cis))	1,2-dipalmitoyl-sn-glycero-3-phospho-(1'-rac-glycerol) (sodium salt)	Adenosine	L-Glutathione reduced	Cholesterol
18:1 Lyso PC (1-oleoyl-2-hydroxy-sn-glycero-3-phosphocholine)	1-palmitoyl-2-hydroxy-*sn*-glycero-3-phosphocholine (Lyso PC)	16:0-18:1 PG (1-palmitoyl-2-oleoyl-sn-glycero-3-phospho-(1'-rac-glycerol) (sodium salt))	L-Canavanine	Oxalic acid	D-(+) Glucose
Betaine	Sphingomyelin (Egg)		Betaine	γ-Aminobutyric acid (GABA)	L-Tyrosine
	L-a-phosphatidylethanolamine (Liver, Bovine)		Taurocholic acid sodium salt hydrate	Hydroquinone	Palmitic acid
	18:1 Lyso PC (1-oleoyl-2-hydroxy-sn-glycero-3-phosphocholine)		Sarcosine	Nicotinic acid	Glyceryl tripalmitate
			L-Arginine	Folic acid	
			L-Tryptophan		
			Nicotinamide		

Table 1. Different standard compound mixtures for test the different solid-state substrates, and the mixture to calibrate the spectra.

Figures

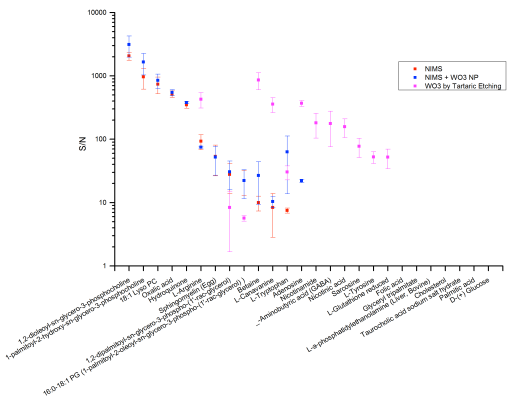

Figure 1. Mean and standard deviation of the Signal to Noise between the different spot of the same standard mix in the different tested substrates, in red NIMS, blue NIMS with WO3 Nanoparticles and pink WO3 by Tartaric etching.

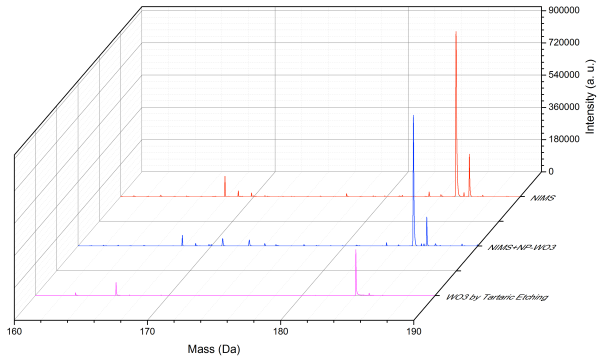

Figure 2. Comparison of the same region of the urine sample noise in red NIMS, in blue NIMS with WO3 Nanoparticles and pink WO3 by Tartaric etching

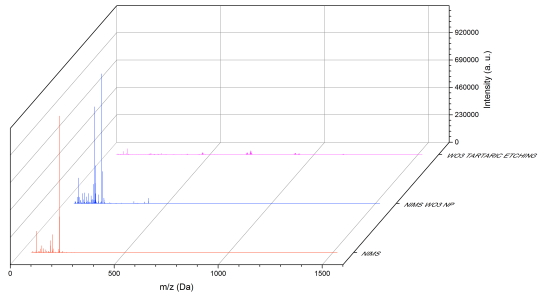

Figure 3. Background noise in red NIMS, in blue NIMS with WO3 Nanoparticles and pink WO3 by Tartaric etching.

Rapid Detection of Proteins Using Potentiometric Biosensors Based on Carbon Nanotubes and Aptamers: Towards Optimum Performance

Tesfalem Geremariam Welearegay[1,2,3], Pascal Blondeau[2], Jordi Riu[2]

e-mail: gem.tesfa@gmail.com,

[1]*Department of Electronics, Electrical and Automatic Engineering, Universitat Rovira i Virgili*

Campus Sescelades, Av. Països Catalans 26, 43007 Tarragona, Spain

[2]*Department of Analytical and Organic Chemistry, Universitat Rovira i Virgili*

Campus Sescelades, c/Marcel-lí Domingo s/n, 43007 Tarragona, Spain

[3]*Department of Chemistry, Mekelle University, P.O. Box 231, Mekelle, Ethiopia*

The rapid progress of nanotechnology and advanced nanomaterials production offer significant opportunities for designing powerful analytical devices with enhanced performance. Carbon nanotubes along with aptamers for biosensing represent an interesting hybrid material for potentiometric biosensors (the so called aptasensor), for the development of robust and rapid methods for protein detection. However, to guarantee an efficient performance of aptasensors for a range of proteins, some challenges concerning fundamental aspects such as pH, size of protein, ionic strength, transducer, and substrate material still remain to be faced. In this work, a potentiometric aptasensor based on single walled carbon nanotubes (SWCNTs) and aptamer for lysozyme detection as a model protein has been developed. The performance properties of the aptasensor at three pH values and substrate material were assessed, while keeping the other media conditions constant. The aptasensors displayed varying potential response against lysozyme addition at different pHs, pH=4.8, 7.5 and pH=9.0 which is consistent with charge to pH profile of the protein. As a result, a best sensitivity of 4.37 ± 0.32 mV/decades of lysozyme concentration at pH=4.8 was recorded for the corresponding linear range 200 M – 10 µM with a good reproducibility of 7.3% for SWCNT/GC based aptasensors. The performance of the aptasensors was also assessed to determine whether they possess the same performance before and after regeneration for further use. The issue of non-specific binding of protein on the surface of SWCNTs remained the challenge while trying to optimize performance of aptasensors.

Keywords: *Carbon nanotubes, aptamer, protein detection, aptasensors, non-specific binding*

Modeling Current Collapse in AlGaN/GaN HEMTs Using a New Equivalent Circuit Based on the Virtual-gate Approach

Fetene M. Yigletu and Benjamin Iñiguez, *Senior Member*, *IEEE*

***Abstract*—In This work a new DC equivalent circuit incorporating a virtual gate as an additional external fourth port in the gate-drain region is described. The maximum voltage value and the duration of a stress applied to a device have been shown to be the main factors that determine the severity of the current collapse. Mechanisms to capture these various levels of current compression have been devised mainly using the voltage and length of a virtual gate placed in the gate drain region. The model is based on a physics-based core drain current model. The virtual gate is incorporated as a separate fourth port that can be biased separately. This allows implementing the model in circuit simulators easily. The model is used to reproduce different current compression levels due to various stress levels applied to a device where it showed a good agreement with measurement data.**

***Index Terms*— HEMTs, Compact model, Current collapse**

I. Introduction

Despite the astonishing performance of AlGaN/GaN HEMTs in high power applications [1]–[3], the current and output power reductions due to current collapse that show up during high voltage applications have been shown to be the major pitfall of these devices [4]–[6]. In relation to this, there are not many compact models suggested for the current collapse effects to be used in circuit simulations, not even hand full of them. In fact, this could be related to the fact that the root causes of the effect are not still well known and a general agreement is not yet reached on the mechanisms that cause the effect.

Meanwhile, it has been widely reported that an additional negative charge, created due to entrapment of electrons by acceptor-type surface states at the heterojunction interface in the gate-drain region, will deplete the 2DEG under it and causes reduction of the drain current, the virtual gate concept [6]. As mentioned above, even if there are different suggestions on the formation of this additional charge in the gate-drain region, models can be built by considering the additional charge as a secondary gate voltage applied in the gate-drain access region. that depletes the underlying 2DEG channel and results in a lower drain current. Using this approach, [7] [8], and our previous compact GaN HEMT model [9], we propose in this work an alternative continuous compact physical model for the current collapse, caused by permanent or semi-permanent damage of the gate-drain region, suited for circuit simulation applications.

This work is supported by the European Commission under FP7 project IAPP-218255 ("COMON"), by the Spanish Ministerio de Ciencia y Technologia under Projects TEC2011-28357-C02-01, and also by the ICREA Acadamia Prize.

Fetene M. Yigletu, and Benjamin Iñiguez, are with the Department of Electrical Electronics and Automation Engineeting, Universitat Rovira i Virgili, Tarragona, Spain (email: fetenemulugeta.yigletu@urv.cat or benjamin.iniguez@urv.cat).

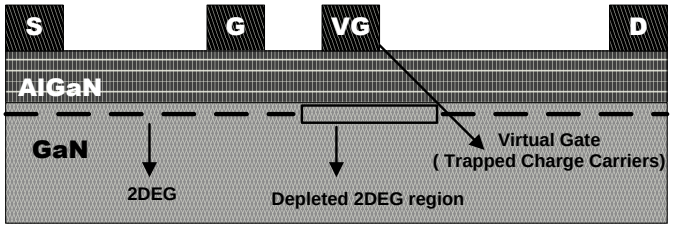

Fig. 1. Device structure showing the effect of the charge carriers accumulated in the gate-drain region that tends to deplete the 2DEG under it.

II. Current Collapse Modeling

Fig. 1 shows a layout of a device which had accumulated unwanted charge carriers in its gate-drain region. As the virtual gate concept states it, the effect of this additional charge is similar to applying a negative voltage through a secondary gate attached to the gate-drain region right next to the main gate which tends to deplete the 2DEG under it [6]. Regardless of the origin of these charge carriers, we can model the current collapse by considering a secondary gate voltage at the gate-drain region. To simulate the DC characteristics of a device in the existence of current collapse we propose the circuit configuration depicted in Fig. 2. As shown in Fig. 2, a secondary, virtual, gate has been placed in the gate-drain region as a representative of the additional charge carriers trapped in the region. It is important to be aware that this configuration is used only before the commencement of saturation in the device. The reason for this will be explained shortly after in this section.

In comparison with the basic DC equivalent circuit, the new equivalent circuit in Fig. 2 has two additional points to consider, the virtual gate port and the new internal node which is the connection point between the drain of the main transistor and the source of the virtual transistor. The virtual gate value is set in proportion with the amount of charge accumulated and usually in such cases it is used as a fitting parameter and is adjusted to best fit measurement data. The current and voltage values at the new internal node in the gate-

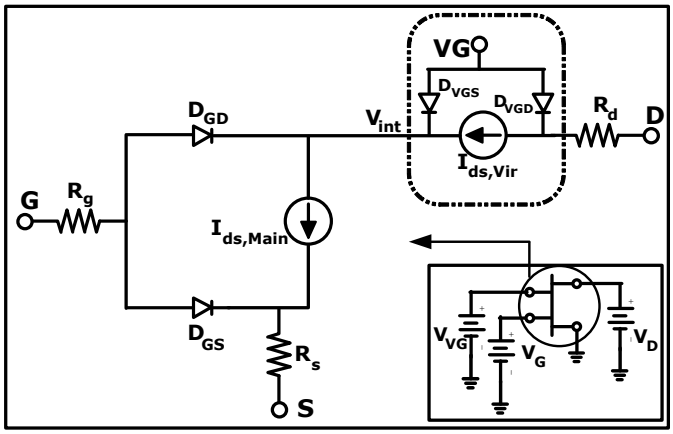

Fig. 2. DC equivalent circuit of a HEMT device including a virtual transistor. Inset: Model implementation setup used in ADS. The four ports of the transistor symbol correspond to the four terminals of the equivalent circuit.

drain region have to be solved systematically. In the analysis of a normal DC topology, without the virtual transistor, this node is just an internal drain node after a voltage drop over the drain access region resistance, R_d. However, under the schematic shown in Fig. 2 the voltage and the current values at the internal node have to be calculated in such a way that considers the effect of virtual gate in the region. To start with, we adopted the approach used in [8] where the current throughout the channel is assumed to be continuous and the saturation starts from the drain edge of the virtual gate. We have found this approach to be more effective than the one used in [7] where the charge trapped region is incorporated as a fully saturated gateless transistor in series with the main transistor.

The current under the main gate and the virtual gate are calculated using a continuous compact physical drain current model given in [9]. Assuming current continuity under each gate, we have

$$I_{ds_{Main}}(V_S, V_G, V_{\text{int}}) = I_{ds_{Vir}}(V_{\text{int}}, V_{VG}, V_D) \qquad (1)$$

where V_G and $I_{ds_{Main}}$, and V_{VG} and $I_{ds_{Vir}}$ are the gate voltage and drain currents of the main and the virtual transistors respectively and V_{int} is the voltage at the drain of the main gate which is also the voltage at the source of the virtual gate.

In circuit simulators such as ADS, (1) should be executed automatically as long as the equivalent circuit shown in Fig. 2 is deployed properly. The inset inside Fig. 2 shows the actual basic setup of the model that can be used in ADS. While using numerical solvers like MATLAB, (1) can be used to solve for the unknown, V_{int}, so that the two equal currents can be calculated using the model given in [9]. The drain current should be calculated in such a manner until the saturation of the virtual gate is reached. This operating regime can be characterized by simply calculating the saturation voltage of the device for the specific gate voltage applied to the device given in [9].

After the start of saturation at the region under the virtual gate, the length of the virtual gate length will not remain intact

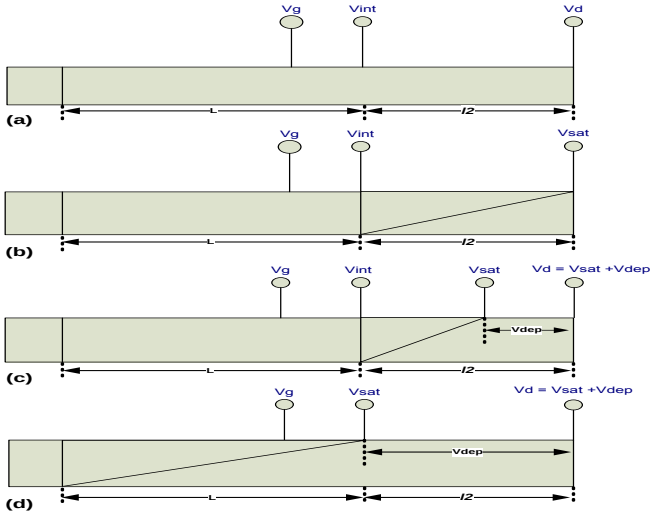

Fig. 3. Gradual saturation point movement from the virtual gate to the main gate, (a) before saturation, (b) saturation start at the virtual gate, (c) saturation moving towards main gate, (d) saturation start at the main gate.

anymore since the saturation point continues to move towards the source of the virtual gate (or towards the drain of the main gate). Therefore, for (1) still to hold the appropriate modification of the length of the virtual gate region used in the right hand side of the equation should be made. The modified length of the channel under the virtual gate is calculated as

$$l_{2,\text{mod}} = l_2 - \Delta l_2 \qquad (2)$$

where l_2 is the length of the virtual gate and Δl_2 is the length of the depleted region under the virtual gate and can be calculated as shown later in (5). The current across both transistors can be calculated in such a way as long as the depletion region under the virtual gate does not exceed the length of the virtual gate. When the drain voltage is increased continuously, finally the whole length of the virtual gate will be depleted and the saturation point reaches the drain end of the main gate. The virtual gate will not be treated in the same manner anymore as shown in Fig. 2, rather, the part of Fig. 2 in the dashed rectangle will then become just a simple resistor in the gate-drain region in series with R_d. This indicates the commencement of saturation under the main gate. The voltage at which this occurs is taken as the new saturation voltage of the main gate. It can easily be calculated as

$$V_{Sat} = V_{Sat,Vir} + V_{dep} \qquad (3)$$

where V_{dep} is the voltage drop across the full length of the virtual gate. V_{dep} can be calculated using the expression derived for calculating a voltage drop at a point in a depleted region [7]. Thus, after the complete depletion of the region under the virtual gate, we have

$$V_{dep} = \lambda E_S \sinh\left(l_2 / \lambda\right) \qquad (4)$$

where E_s is the saturation field and λ is the characteristics length of the depletion region. Note that (3) and (4) show that the creation of the virtual gate at the gate-drain region has

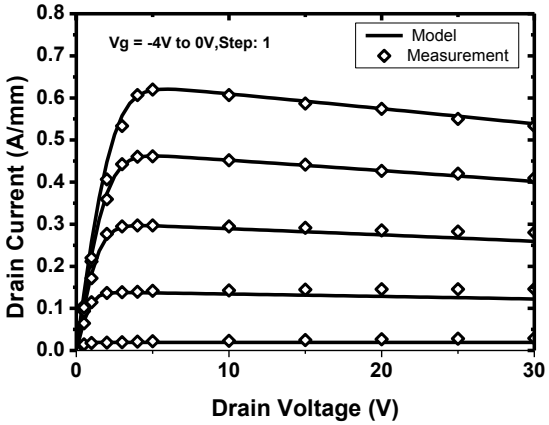

Fig. 4. Output characteristics of a 1μm gate length device, measured (diamonds) and modeled (solid lines), before stress shown for Vg -4V to 0 with 1V step from top to bottom, data from [10].

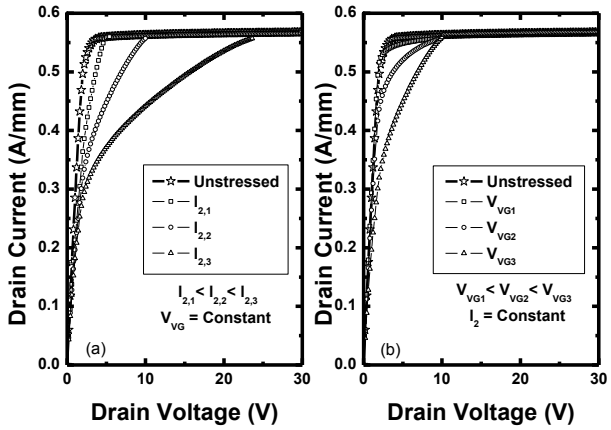

Fig. 5. The effects of Virtual gate voltage and length parameters on the performance of the model when one is varied while the other is fixed.

introduced a shift in the saturation of the main gate in comparison with the saturation point before collapse. This gradual saturation of the virtual and main gates is shown in Fig. 3(a)-(d).

After the saturation of the region under the main gate is reached a further increase in voltage will once again move the depletion region into the main gate region towards the source. This depletion region extension will reduce the length of the channel under the main gate. The modified channel length is simply $L-\Delta L$, where ΔL is the length of the depleted region under the main gate. From the expression of voltage drop in a depleted region, (4), one can solve for the length of the depleted region as

$$\Delta L = a\sinh\left(V_{\text{int}} - V_{sat} \Big/ \lambda E_S\right)\lambda . \qquad (5)$$

Note that (5) is also used to calculate Δl_2 using the appropriate drain and saturation voltages.

III. Results and Discussion

The DC equivalent circuit shown in Fig. 2 has been implemented in the circuit simulator ADS from Agilent to simulate the output characteristics of devices after stress. The setup used is shown in the inset of Fig. 2. A device with a gate length of 1μm and a width of 150μm from [10] has been used. To demonstrate the performance of the core current model and for the purpose of comparing it with that of after stress, the output characteristics of the device before stress have been simulated using the current model given in [9]. Fig. 4 shows the simulated and measured output characteristics of the device before stress. It is shown that the continuous physical core current model is able to reproduce the output characteristics very well.

Once the reliability of the core current model is shown, the virtual gate model described in the previous section based on this core current model is applied. The virtual gate has been modeled as the fourth port of the normally three terminal

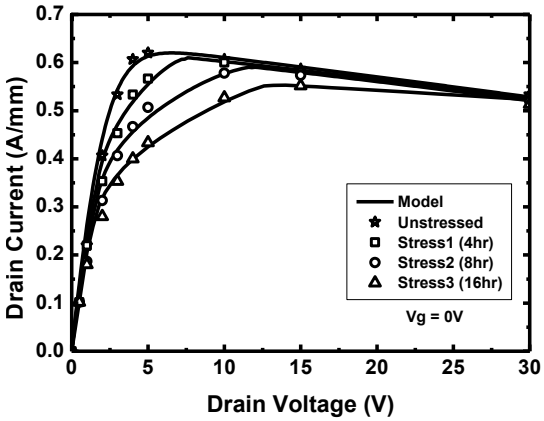

Fig. 6. Measured (symbols) and modeled (solid lines) output characteristics of a 1μm gate length device. The various levels of current collapse correspond to the various hours of stress, data from [10].

device, similarly to a double gate transistor, using Verilog-A, the standard compact modeling language. This by far simplifies the use of the model in the circuit simulator since it is now possible to apply a direct bias at the virtual gate as any other port. The four port layout will be very useful for future developments of the model where the virtual gate voltage is not anymore a single fitting value but is dynamic and calculated in terms of all the physical factors that should be considered such as the trapped charge carrier distribution and the value and duration of the maximum drain voltage applied.

To look into the mechanics of the present model, different levels of permanent or semi-permanent current collapse shown by a device are considered, [10]. The work by Mittereder et al, [10], shows the dependence of the extent of current collapse, gate-drain region damage, on the intensity of the stress under which the device has been placed. It has been shown that both the value of the maximum drain voltage applied and the duration of the stress have direct influences on the level of the current collapse. In this regard, the maximum drain voltage and hours of stress determine the intensity of the current collapse.

Table I
List of Model parameters

Parameter	Description	Value
V_{off} (V)	Cut-off Voltage	-4.2
μ_0 (cm^2/Vs)	Low field mobility	900
μ (cm^2/Vs)	saturation mobility	790
λ (nm)	Characteristics length of saturation region	43
l_2 (nm)	Virtual gate length	41(Stress1) 45(Stress2) 47(Stress3)
V_{VG} (V)	Virtual gate voltage	-4.2(Stress1) -4.3(Stress2) -4.5(Stress3)

Likewise, the significances of the main virtual gate model parameters, the length and voltage of the virtual gate, on the overall output of the model have been analyzed. The length of the virtual gate determines the shift in the saturation point of the main gate. This is exclusively indicated during the calculation of the new saturation voltage, (3), based on the voltage drop across the depleted region which is dependent on the length of the virtual gate, (4). Fig. 5(a) shows the role of the virtual gate length parameter. The longer virtual gate lengths resulted in longer shifts of the saturation point of the main gate while the virtual gate voltage is kept constant. Similarly, the effect of the virtual gate voltage parameter is shown in Fig. 5(b). Unlike the virtual gate length parameter, the virtual gate voltage does not shift the saturation point of the main gate channel region. Rather, it determines the severity of the current collapse in the affected region. It represents the concentration of the charge carriers trapped in the gate-drain region that determines the strength of the repelling field that the charge carriers in the underlying channel experience. Fig. 5(a) and Fig. 5(b) depict the two important boundaries of the current collapse region that are determined by the length and voltage of the virtual gate. A systematic optimization of these parameters is therefore necessary to reproduce the current collapse exhibited by a device under a specific level of stress. The fact that one has to use pre-assumed values for the voltage and length of the virtual gate is probably the main drawback of such virtual gate models. Devising analytical ways of calculating the values of these parameters, after considering all the factors involved, is expected to make the virtual gate modeling even more powerful.

Fig. 6 shows a comparison between the present model and a measurement data taken after a device has been put into different levels of stress. The consecutive levels of stress were imposed on the device by varying the hours of stress [10]. The model has reproduced all levels of stress very well. This shows the capability of the model to trace a wide range of current collapse levels. Table I shows the list of parameters used to model the device considered here, after stress.

IV. Conclusion

A compact physical drain current model and a virtual gate approach have been combined to produce a robust model for the current collapse effect in AlGaN/GaN HEMT devices. The direct calculation of the current using a continuous drain current model and the implementation of a new equivalent circuit containing the virtual transistor in a circuit simulator is found to be simpler to use and yet powerful. This provides an insight into a universally applicable integration of a controlled virtual transistor with various drain current models in circuit simulators. This approach presents a practical rather than theoretical consideration of virtual gate modeling for circuit simulation. The same model can also be used to simulate the I-V characteristics before current collapse by simply 'turning off' the virtual gate. The model has been implemented in a circuit simulator where it is used to simulate the I-V characteristics of a device after current collapse. The good agreements shown between measurement data and the model witnesses the validity of the approach proposed in this work.

References

[1] D. Kapolnek, J. P. Ibbetson, P. Parikh, B. P. Keller, and U. K. Mishra, "Very-high power density AlGaN/GaN HEMTs," IEEE Trans. Electron Devices, vol. 48, no. 3, pp. 586–590, Mar. 2001.

[2] U. K. Mishra, L. Shen, T. E. Kazior, and Y. Wu, "GaN-Based RF Power Devices and Amplifiers," in Proc. IEEE, vol. 96, no. 2, pp. 287–305, Feb. 2008.

[3] Y. Wu, A. Saxler, M. Moore, R. P. Smith, S. Sheppard, P. M. Chavarkar, T. Wisleder, U. K. Mishra, and P. Parikh, "30-W / mm GaN HEMTs by Field Plate Optimization," IEEE Electron Device Lett., vol. 25, no. 3, pp. 2003–2005, 2004.

[4] S. C. Binari, K. Ikossi, J. A. Roussos, W. Kruppa, D. Park, H. B. Dietrich, D. D. Koleske, A. E. Wickenden, and R. L. Henry, "Trapping Effects and Microwave Power Performance in AlGaN/GaN HEMTs," IEEE Electron Device Lett., vol. 48, no. 3, pp. 465–471, 2001.

[5] G. Verzellesi, R. Pierobon, F. Rampazzo, G. Meneghesso, A. Chini, U. K. Mishra, C. Canali, and E. Zanono, "Experimental/Numerical Investigation on Current Collapse in AlGaN/GaN HEMT's," in Proc. Electron Devices Meeting, 2002, no. I, pp. 689–692.

[6] R. Vetury, N. Q. Zhang, S. Keller, and U. K. Mishra, "The Impact of Surface States on the DC and RF Characteristics of AlGaN/GaN HFETs," IEEE Trans. Electron Devices, vol. 48, no. 3, pp. 560–566, Mar. 2001.

[7] A. Koudymov, M. S. Shur, G. Simin, K. Chu, P. C. Chao, C. Lee, J. Jimenez, and A. Balistreri, "Analytical HFET I – V Model in Presence of Current Collapse," IEEE Trans. Electron Devices, vol. 55, no. 3, pp. 712–720, 2008.

[8] M. Morardi and P. Valizadeh, "Analytical Modeling of Current Collapse in AlGaN / GaN HFETs According to the Virtual Gate Concept," IEEE Trans. Device Mater. Reliab., vol. 10, no. 2, pp. 287–294, 2010.

[9] F. M. Yigletu, S. Khandelwal, T. A. Fjeldly, B. Iñiguez, "Compact Charge-Based Physical Models for Current and Capacitances in AlGaN / GaN HEMTs," IEEE Trans. Electron Devices, vol. 60, no. 11, pp. 3746–3752, 2013.

[10] J. A. Mittereder, S. C. Binari, P. B. Klein, J. A. Roussos, D. S. katzer, D. F. Storm, D. D. Koleske, A. E. Wickenden, R. L. Henry, "Current Collapse Induced in AlGaN/GaN HEMTs by Short-Term DC Bias Stress," in IEEE 41st Annual International Reliability Physics Symposium, 2003, pp. 320–323.

INFORMATION CONTACT

Administrative contact:

Dr. Josep Ferré Borrull:
Email: josep.ferre@urv.cat
Phone: 34+ 977 559 632 , **Fax:** 34+ 977 559 605

Programme chairman:

Dr. Roberto Giral Castillón
Email: roberto.giral@urv.cat
Phone: 34+ 977 559 620 , **Fax:** 34+ 977 559 605

Informatic support:

Jordi Maré Viles
Email: jordi.mare@urv.cat
Phone: 34+977 559 712 , **Fax:** 34+977 558 501

Administrative support:

Angels Hernando Casado
Email: angels.hernando@urv.cat
Phone: 34+ 977 559 610 , **Fax:** 34+ 977 559 605

Dolores Córdoba Sánchez
Email: dolores.cordoba@urv.cat
Phone: 34+ 977 559 728 , **Fax**: 34+ 977 559 605

Franzina Borràs Martorell
Email: francina.borras@urv.cat
Phone: 34+ 977 559 726 , **Fax**: 34+ 977 559 605

DIPUTACIÓ DE TARRAGONA

IEEE

FUNDACIÓ URV